QUATERNARY STRUCTURE ANALYSIS OF CALCIUM/CALMODULIN-DEPENDENT PROTEIN KINASE II ALPHA BY CRYO-ELECTRON MICROSCOPY

by

Scott Charles Bolton

A Dissertation

Submitted to the Faculty of Purdue University

In Partial Fulfillment of the Requirements for the degree of

Doctor of Philosophy

Department of Chemistry

West Lafayette, Indiana

December 2019

THE PURDUE UNIVERSITY GRADUATE SCHOOL
STATEMENT OF COMMITTEE APPROVAL

Dr. David H. Thomspon, Co-Chair
Department of Chemistry

Dr. Tamara L. Kinzer-Ursem, Co-Chair
Weldon School of Biomedical Engineering

Dr. Cynthia V. Stauffacher
Department of Biological Sciences

Dr. Chittaranjan Das
Department of Chemistry

Approved by:
Dr. Christine Hrycyna

I dedicate this work to my wife Michelle, whose only wish for me was to find happiness. Because of you, I got that wish.

ACKNOWLEDGMENTS

First, I would like to acknowledge Prof. David Thompson. Thank you so much for giving me the fundamental skills to be successful in my journey, and for patiently and persistently encouraging me to embrace cryo-EM during the years when I was convinced I would never touch signal processing again. Thank you for allowing me the freedom to find my passion in science, and for giving me the time to learn how to solve challenging problems. Prof. Cynthia Stauffacher and Prof. Chittaranjan Das, your kind words of encouragement over the years motivated me to keep going. I also would like to acknowledge Prof. Thomas Walz at Rockefeller University, whose input and critique profoundly shaped my viewpoint, and the outcome, of this work. Prof. Andy Hudmon, thank you for sharing your time, expertise and allowing me to move into your lab for a year. This project would not have progressed without your help. To Prof. Angeline Lyon and Elisabeth Garland-Kuntz, thank you for making room for me in your lab, as well. I especially would like to acknowledge Dr. Thomas Klose and Valorie Bowman at the Purdue Cryo-EM Facility. Both of you have made me feel welcome since day one. I have watched you sacrifice many of your evenings and days off to keep the microscopes online and everyone's experiments moving forward. It does not go unnoticed, and I sincerely appreciate your help over the years. I would also like to acknowledge Dr. Uma Aryal and Vicki Hendrick at the Purdue Proteomics Facility and Dr. Chris Gilpin at the Purdue Life Science Microscopy Facility. Dr. Keith Vicarro, thank you for sharing your expertise in kinase activity measurement. Thanks also to Dr. Kyle Wright and Dr. Christopher Benjamin for your help with monolayer preparation. To my fellow lab members Dr. Kaisa Ejendal, Dr. Matt Pharris, Aya Saleh, and Julia Fraseur: you have always made the lab a positive place to work. Thanks also to Purdue University and the PULSe Program for accepting and supporting me throughout my studies, and I gratefully acknowledge the support of this work from Purdue University Center for Cancer Research NIH Grant P30 CA023168 and NIH Grant R21 NS095218. Finally, I would like to acknowledge Prof. Tamara Kinzer-Ursem. You are an outstanding mentor, and it is a joy to see you connect with students and colleagues alike that share the same passion for science that you do. It is my goal to encourage and mentor others as much as you did for me. Thank you for opening up the world of neuroscience to me, and for your guidance in this journey: past, present, and future.

TABLE OF CONTENTS

LIST OF TABLES

LIST OF FIGURES

LIST OF ABBREVIATIONS

AD	Alzheimer's disease
AFM	Atomic force microscopy
AMPAR	α-amino-3-hydroxy-5-methyl-4-isoxazolepropionic acid receptor
ATP	Adenosine triphosphate
BEVS	Baculovirus-insect expression vector system
BSA	Bovine serum albumin
CaM	Calmodulin
CaMKII	Calcium/calmodulin-dependent protein kinase II
CMC	Critical micelle concentration
CMOS	Complementary metal–oxide–semiconductor
Cryo-EM	Cryogenic electron microscopy
Cryo-ET	Cryogenic electron tomography
CTF	Contrast transfer function
CV	Column volume
DCM	Dichloromethane
DDD	Direct detection device
DMF	N,N-Dimethylmethanamide
EFTEM	Energy-filtered transmission electron microscopy
EPSP	Excitatory Postsynaptic Potential
FBS	Fetal bovine serum
FPLC	Fast protein liquid chromatography
GO	Graphene oxide
HEPES	4-(2-hydroxyethyl)-1-piperazineethanesulfonic acid
IMAC	Immobilized metal affinity chromatography
IPA	Isopropanol
IPTG	Isopropyl-β-D-thiogalactoside
MeOH	Methanol
MOI	Multiplicity of infection
NMDAR	N-methyl-D-aspartate receptor
NTA	Nitriltrioacetic acid
OD	Optical density
PABA	Para-aminobenzoic acid
PAGE	Polyacrylamide gel electrophoresis
PMSF	Phenylmethylsulfonyl fluoride
PSD	Postsynaptic density
RCT	Random conical tilt
SAXS	Small-angle X-ray scattering
SDS	Sodium dodecyl sulfate
SEC	Size exclusion chromatography
SEM	Scanning electron microscopy
SOC	Super optimal broth
TEM	Transmission electron microscopy
THF	Tetrahydrofuran
TIRF	Total internal reflection fluorescence
TKG	Tetracycline kanamycin gentamycin

ABSTRACT

Calcium-dependent protein kinase II alpha (CaMKIIα) is a highly abundant protein within the hippocampus, the region of the brain responsible for memory and learning. CaMKII has both structural and signaling roles in the regulation of the connective strength of synapses in excitatory neurons. It has a unique structure comprised of twelve subunits that form a dynamic assembly and is highly flexible. Its structural behavior has been shown to affect its activity, and a comprehensive mechanism of structure and function is still not fully understood. The determination of the quaternary structure of the CaMKII holoenzyme has been attempted for nearly 20 years by a variety of methods, with no one method giving a definitive structure. Problems in obtaining a structure originated with observation methods that estimated quaternary shape from low-resolution ensemble averages or required significant alteration of the protein to enforce a particular conformation. In this work, experiments were conducted to remove these limitations and provide a path towards the quaternary structure of CaMKIIα. Different expression and purification methods were evaluated to produce an optimal protocol for the generation of samples of concentrated, monodisperse, autoinhibited full-length wild-type CaMKIIα for study with cryo-electron microscopy. Strategies for microscopy sample preparation were investigated, including affinity girds, graphene-coated grids, and holey carbon grids. Lastly, experiments using negative stain electron microscopy, cryo-electron microscopy with single particle analysis, and cryo-electron tomography with subtomogram averaging were conducted to reveal the conditions required to produce an unambiguous three-dimensional structure. It was found that the assembly of the hexameric hub rings appeared to have flexible orientation, and superposition problems inherent in two-dimensional projection averaging requires the use of cryo-electron tomography to unravel the ambiguity in both hub orientation and catalytic module placement within the reconstructed volume. A subtomogram average of a limited number of particles revealed a hub domain that matched the morphology of prior reports, but the determination of catalytic module placement was not resolved. The cumulative result of this work establishes a strategy for the large-scale data collection needed to fully elucidate the structure of this challenging and fascinating protein.

CHAPTER 1. INTRODUCTION TO CALCIUM CALMODULIN-DEPENDENT PROTEIN KINASE II ALPHA

1.1 The Hippocampus and Neuronal Synaptic Plasticity

The hippocampus, a small region of the human forebrain located near the cortex, plays a major role in our ability to learn and form memories. The dynamic strengthening and weakening that occurs during learning and memory formation, termed plasticity, presents exciting challenges in research as there is much we do not yet understand about its mechanism of operation. Beyond basic research, decoding the mechanism of plasticity is an urgent healthcare concern. The degeneration of synaptic plasticity is one of the hallmarks of Alzheimer's disease[1] [2] [3]. As of 2016, Alzheimer's disease and related dementia affects 5.4 million people in U.S.[4], and the cost of treating Alzheimer's Disease patients alone totaled $600B[5]. Neurological disorders, including schizophrenia, epilepsy, and long-term depression, also are correlated with the loss of plasticity and atrophy of the hippocampus[6]. While neuroimaging hippocampal volume can reveal degeneration of the hippocampal volume and cognitive testing can detect memory impairment, differentiating between normal age-related functional decline and Alzheimer's disease is not entirely clear. A greater understanding of bimolecular synaptic function is needed to find disease-specific biomarkers[7] [8]. At a minimum, early-detection biomarkers could ameliorate the increased burden of care by implementing an early treatment plan before chronic symptoms occur.

In the hippocampus, plasticity is mediated by the mechanisms of long-term potentiation or long-term depression. The post-synaptic neuron is sensitive to both frequency and amplitude of an action potential[9]. The threshold to create an excitatory postsynaptic potential (EPSP) is

strength dependent and can be fed by multiple action potentials from different neurons firing together, or from the same source repeatedly firing over time. This change in strength, either increasing or decreasing, is the biochemical process of memory being formed.

Stronger synaptic connections incur larger depolarization and are more likely to create an action potential in the postsynaptic neuron. But how does this work? Nerve impulses at the soma end of the axon travel down as an action potential where it depolarizes the terminal membrane, causing the presynaptic membrane to fuse with the plasma membrane and release neurotransmitters that bind receptors on the postsynaptic membrane. On the postsynaptic neuron, α-amino-3-hydroxy-5-methyl-4-isoxazolepropionic acid receptors (AMPARs) and N-methyl-D-aspartate receptors (NMDARs) also exchange sodium and potassium ions to create a local depolarization at the membrane. AMPARs respond quickly and depolarize the local membrane area in short periods, and are thought to be a gating mechanism to depolarize adjacent NMDARs, which exchange calcium ions as well. These channels open more slowly and remain open for a longer period due to the presence of a magnesium ion that blocks the channel. If glutamate binds the NMDAR and the membrane is depolarized from an action potential, channel-blocking magnesium ions are pushed away and the channel opens to exchange ions including calcium [10].

The calcium influx is not delivered in a single continuous burst, but instead sputters in millisecond bursts. In long-term potentiation, short and rapid bursts of signals from a presynaptic axon will cause a long-lasting increase in the EPSP. If the incoming sputtering frequency is 10–100 Hz, the accumulating calcium will trigger activation of downstream proteins and cause an action potential as well as increased sensitivity to further stimulation. This is called long-term potentiation and strengthens the synaptic connection. In long-term depression, longer and slower bursts occur, and do not change the amplitude of the EPSP. When the burst frequency is 1–5 Hz, the activation of downstream proteins is not rapid enough to cross a minimal threshold to induce an action potential through the postsynaptic neuron. If a slow frequency burst of calcium occurs for several minutes, it can induce de-sensitivity to the neuron and make it more difficult to induce an action potential in the future. This process, named long-term depression, results in synaptic weakening.

The postsynaptic density (PSD) is comprised of a gel-like mixture of proteins 30–40 nm thick that forms dynamic assemblies of proteins during stimulation (Figure 1.1) and the predominant enzyme found in the PSD is calcium/calmodulin-dependent protein kinase II

(CaMKII). A mass spectrometry proteomic analysis of rat forebrain revealed that the expression of CaMKII is at least 10 times higher than other signaling kinases [11]. The enzyme is truly unique – it modulates the functioning of the PSD by binding actin to create are scaffolding structure, is central to the mechanism of long-term potentiation, and contributes to the regulation of growth factors.

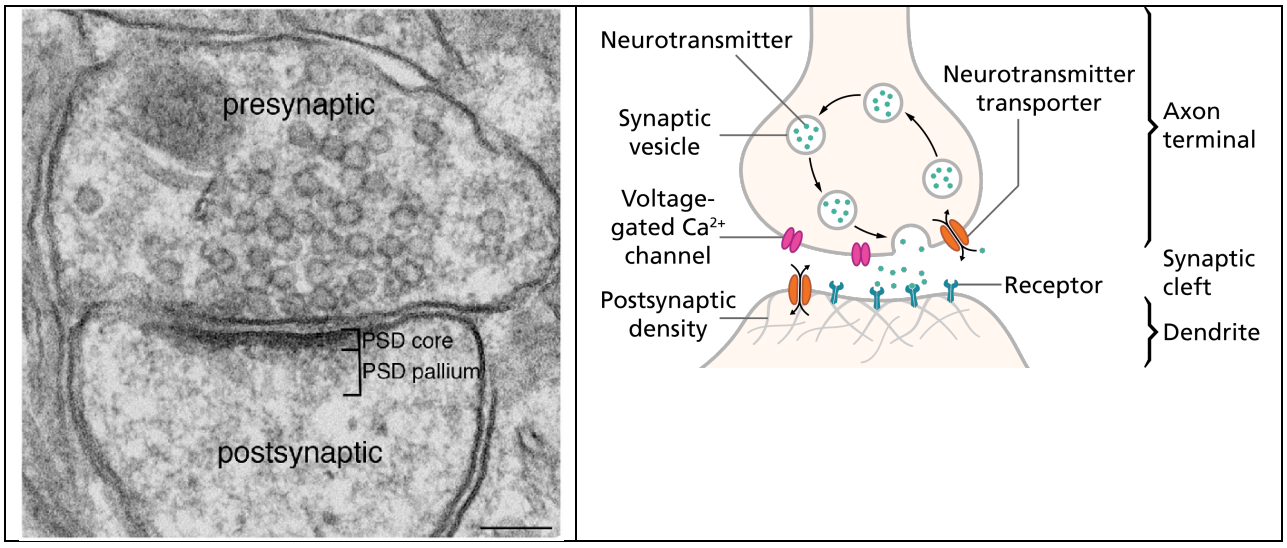

Figure 1.1. Excitatory Synapse. (Left) TEM image of the synapse and post-synaptic density[12]. Scale bar 100 nm. (Right) Schematic of neurotransmitter communication across the synaptic junction. Image courtesy of Thomas Splettstoesser. Both images (CC BY).

1.2 Calcium/Calmodulin-Dependent Protein Kinase II

CaMKII is highly abundant in the hippocampus, the region of the brain responsible for memory and learning [13]. CaMKII is implicated as an intersection of pathways for signal transduction [14]. Given its abundance in neurons, it is not surprising that dysfunction of this enzyme has implications in AD pathology [15] [16]. For example, there is mounting evidence to support that hyperactive CaMKII, in part, promotes hyperphosphorylation of Tau proteins, which then leads to aggregation of Tau-bound microtubules into neurofibrillary tangles[17]. Further, studies on memory formation using transgenic mice where CaMKII is either knocked-down or mutated phosphorylation sites exhibited substantial cognitive impairment [13, 18-21] [22]. A collaborative gene sequencing study identified 24 unrelated people with intellectual disability, all of which had rare mutations to CaMKII that modulated auto-phosphorylation and neuronal

migration [23]. Many excellent reviews on CaMKII function have been written: some are listed here[24-30].

1.3 CaMKII Isoform Family

The CaMKII family is comprised of four isoforms: α, β, γ, and δ. Each contains a catalytic module, a linker region of varying length, and an association (or hub) domain. A comparison of the four isoforms found the sequence similarity to be approximately 89-93%[31]. While γ and δ are expressed ubiquitously, the α and β isoforms are highly overexpressed in forebrain neurons. γ and δ are expressed at only 0.02% of the levels of α and β found in the brain [32 31].

The linker region is where the majority of differences occur between these isoforms. Different combinations of exons generate alternative splice variants that create nearly 38 distinct isozymes[33 34].

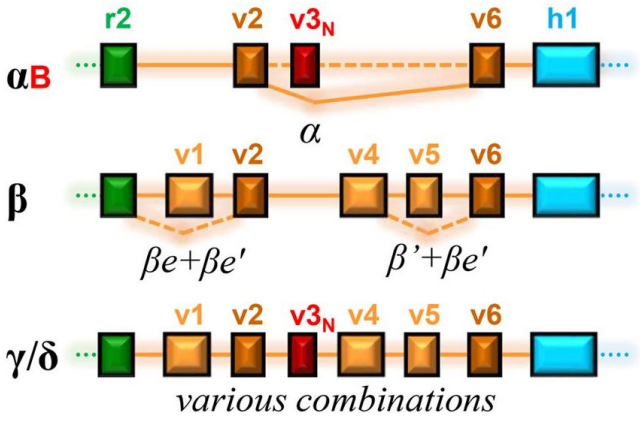

Figure 1.2. Exons comprising the various CaMKII isoforms [35]. (CC BY)

The α isoform has only two variants within the linker. The first, and most common, variant contains exons v2 and v6. The second variant, αB, contains exons v2 and v6 but also includes exon v3, a nuclear localizing sequence [36]. β is different from α in that it also binds actin, though variants βe and βe’ both lack v1 which abolishes actin binding[37]. Though many heterogeneous oligomers readily assemble from different isoform and isozyme combinations [35], heteromers of alpha and beta with a stoichiometric ratio is 3:1 α:β are the most common [38 39]. Heteromers enable a unique function to the holoenzyme where the majority of subunits provide

enzymatic signaling, and the few β subunits anchor the catalytic action on actin within the PSD. Still, homomers have been found in rat forebrain as well [40]. Most studies focus solely on the α homomer because activity measurements can be resolved to the behavior of one subunit type, and structural models can take advantage of the symmetry present in the oligomeric assembly.

1.4 CaMKIIα Sequence and Structure

1.4.1 Catalytic Module

Structure

The catalytic module is comprised of a 278-residue kinase domain followed by a 40-residue regulatory segment that controls the activity of the kinase. The kinase domain is highly conserved across the CaMK family and has a bi-lobed structure[33]. The smaller lobe, at the N-terminal end, contains an ATP-binding motif (residues 19-46) and binds ATP with an approximate K_D of 8 uM[41]. In Figure 1.3 the crystal structure shows an inhibitor residing in the ATP binding pocket. The larger lobe, at the C-terminal end, contains the substrate-binding site (S-site) shown in orange and the target-binding site (T-site) in yellow. [42]

The regulatory (autoinhibtory) segment is found at residues 274–314 and is divided into three segments R1, R2, and R3. In the autoinhibited state, the R1 and R2 segments form an alpha-helix that is conserved across CaM substrates[43]. This inhibitory helix acts as a pseudo-substrate to block the S-site until activation. It has been previously suggested that the regulatory segment also blocks ATP access [27], and a crystal structure of a dimeric catalytic module suggests that this occurs by rearrangement of the binding site [42]. Interestingly, a later monomeric crystal structure showed that it does not have close interaction with the site)[44]. This difference could be attributed to the difference in homology between *C. elegans* and human CaMKIIδ, which share 77% sequence identity.

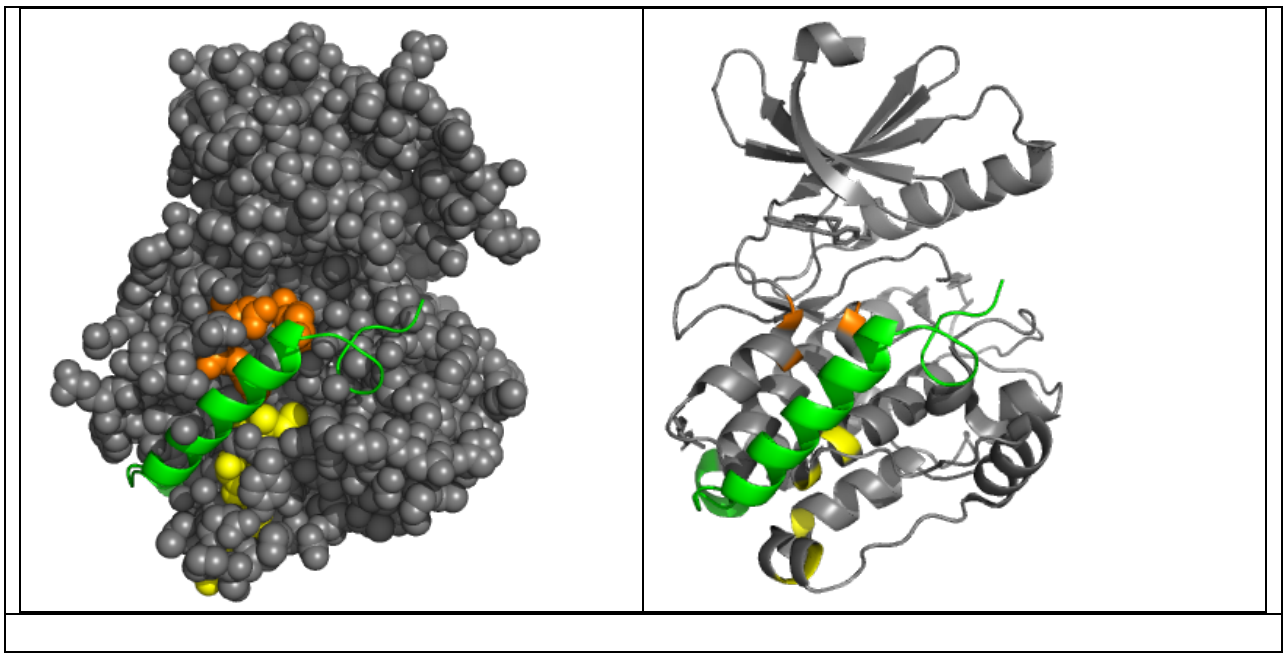

Figure 1.3. Crystal structure of the CaMKIIδ catalytic module (PDBID 2VN9)[44]. Top left: volume drawing with the regulatory segment as ribbon. Top right: ribbon drawing.

The calmodulin-binding motif is located in the R3 segment and partially overlaps the R2 pseudo-substrate segment. In the autoinhibited state, the R3 segment is largely unstructured, but a crystal structure revealed that it folds into an alpha helix when calmodulin binds the segment [44]. This structure also confirmed that CaM-bound R3 resulted in the unfolding of the inhibitory helix into a substrate and oriented Thr 286 in a position favorable for phosphorylation. This is shown in Figure 1.4. Therefore, R1 segment unfolding may result from freedom of movement when not resting the in the S-site hydrophobic groove, and the twist in the peptide that occurs when R3 is induced into helical conformation upon CaM binding.

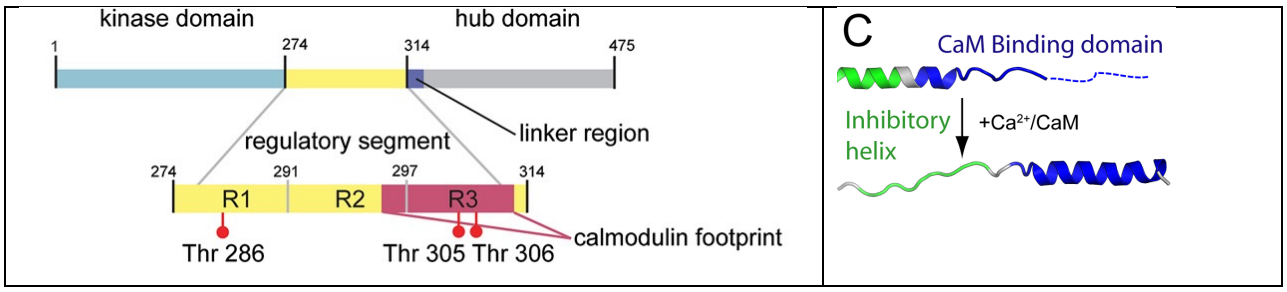

Figure 1.4. Left: schematic of regulatory segment [45]. Conformational changes in Regulatory Segment[44]. (CC BY)

There are three phosphorylation sites that control regulation. Phosphorylation of Thr 286 in the inhibitory helix enables the autonomous activity of the subunit. Phosphorylation of Thr 305 and Thr 306, which are located in the middle of the CaM-binding site, results in the attenuation of activity and an eventual return to the inhibited state.

The α isoform regulatory segment is followed by an unstructured 30-residue linker that serves to tether the catalytic module to the hub domain. The length of this linker affects its catalytic activity and sensitivity to frequencies of calcium bursts.

Autoregulation of the Kinase Domain

Calmodulin is roughly one-half the size of the kinase domain, totaling 148 residues, and has the structure of two domains connected by a flexible linker. Each domain is comprised of two EF-hand motifs, each of which binds one positively-charged calcium ion. When bound by four calcium ions, CaM is able to clamp around the R2/R3 regulatory segment, which then causes the inhibitory helix to unbind from the kinase domain at its T-site and expose the active S-site. This state, Ca2+/CaM–dependently active, has approximately 80% of maximal activity and is not considered a fully active state [46]. The relatively poor micromolar binding affinity of Ca2+/CaM to inhibited CaMKII suggests that there are significant periods where the S site is blocked. With Ca2+/CaM bound, the R1 segment rearranges to become positioned for Thr 286 phosphorylation and enables two functional changes. First, the inhibitory segment becomes charged and thus unable to bind the T site nor block the S-site, which keeps the kinase activated [47-48]. It has also been suggested that when R1 swings open, helix αD also moves in tandem to block R1 from covering the S-site[44]. Second, Ca2+/CaM affinity increases by ~10,000-fold in an effect known as "CaM trapping"[49]. It is not conclusively known if the phosphorylation charge

favors a tighter binding conformation for the CaM binding site or because the separation of the CaM motif from the kinase domain allows full binding. The combination of Thr 286 phosphorylation and bound Ca2+/CaM results in maximal CaMKII activity [46] [50] [51] [52]. This is shown as the middle state in Figure 1.5.

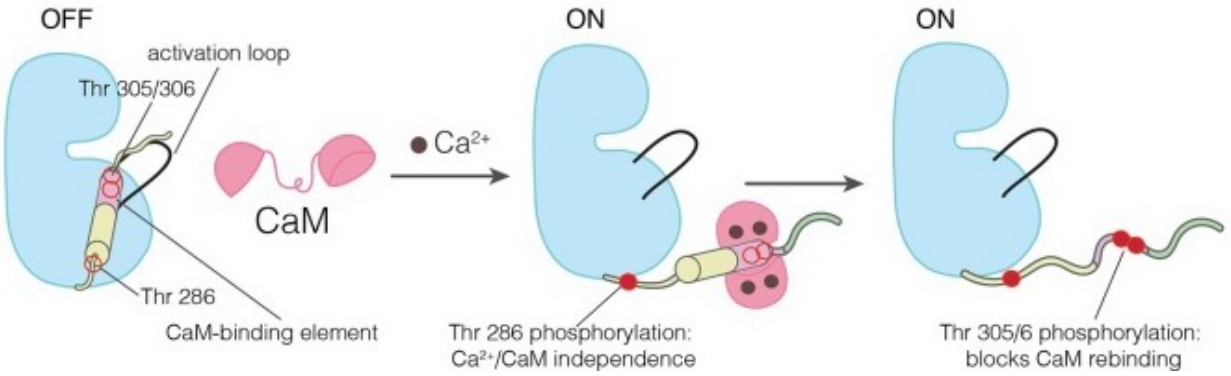

Figure 1.5. Autophosphorylation of a subunit [53] (CC BY)

After a pulse of calcium ions dissipates, CaM loses its bound calcium resulting in a conformational change that causes unbinding from the R2/R3. If Thr 286 was phosphorylated, however, the autoinhibition mechanism will still be blocked, making kinase activity autonomous. The subunit eventually reverts to the inhibited state by phosphatases.

Over the minute timescale, autonomous CaMKII can be phosphorylated again at Thr 305 and Thr 306, key residues at the middle of the Ca2+/CaM binding footprint. This change, known as "CaM capping", prevents Ca2+/CaM from further binding events, and limits the activity to 15% – 40% of maximal activity [51] [50] [25]. This state requires the full de-phosphorylation of regulatory residues and a return to the inhibited state before reactivation [51]. There is controversy regarding this mechanism, as it also has been shown that CaM-capping is purely time-dependent and not a result of CaM-dissociation [54].

A second pathway for activation of an alpha subunit occurs when its T-site binds the GluN2B subunit of the NMDAR. When this occurs, the regulatory region is blocked from returning to an inhibitory state, rendering the kinase fully activated in a persistently bound, activated complex [55]. Because the activity is retained regardless of calmodulin interaction or Thr286 phosphorylation, it is suggested that receptor interaction affects LTP maintenance and holoenzyme activity affects LTP induction.

In summary, autoregulation of the catalytic domain described above reflects a simple coincidence detection model, where increasing Ca2+/CaM results in increasing CaMKII activity. This simplicity, however, does not reflect the cooperative response seen when the subunits assemble into holoenzymes. We must look at the dynamics of subunit interaction in an oligomeric context.

1.4.2 Association Domain

Hub Oligomerization

The association domain is responsible for the oligomerization of the enzyme into a dodecameric form [56 57 58 42 45 59 53 60]. The assembly of the dodecamer can be thought of as two stacked hexameric rings formed by the hub domains, and catalytic modules arranged around the perimeter forming a larger ring. The variable linker regions tether the catalytic modules in a hub and spoke arrangement.

Yet it is more beneficial to think of the assembly as 6 vertical hub domain dimers arranged in a symmetric ring because the top and bottom hub domains bind more strongly than longitudinal ones. It has been shown that CaMKII can exchange subunits by the dissociation of a vertical hub dimer from the complex, and in complement, a vertical hub dimer can wedge into a dodecamer to form a transient tetradecamer [59 53]. This may exist in equilibrium and is shown in Figure 1.6. It is believed that this exchange mechanism is gated by autophosphorylation, whereby inhibited holoenzymes do not exchange subunits. A possible explanation for this behavior is that the autoinhibited kinase domains arrange close to the hub and block access for additional dimer insertion.

Additionally, when hub domains are truncated by proteolytic cleavage or by isolated domain expression, it was found that CaMKII naturally forms a tetradecamer [61 62]. Activated subunits position the kinase domain extended from the hub, and therefore relax the strain on the ring and allow for exchange.

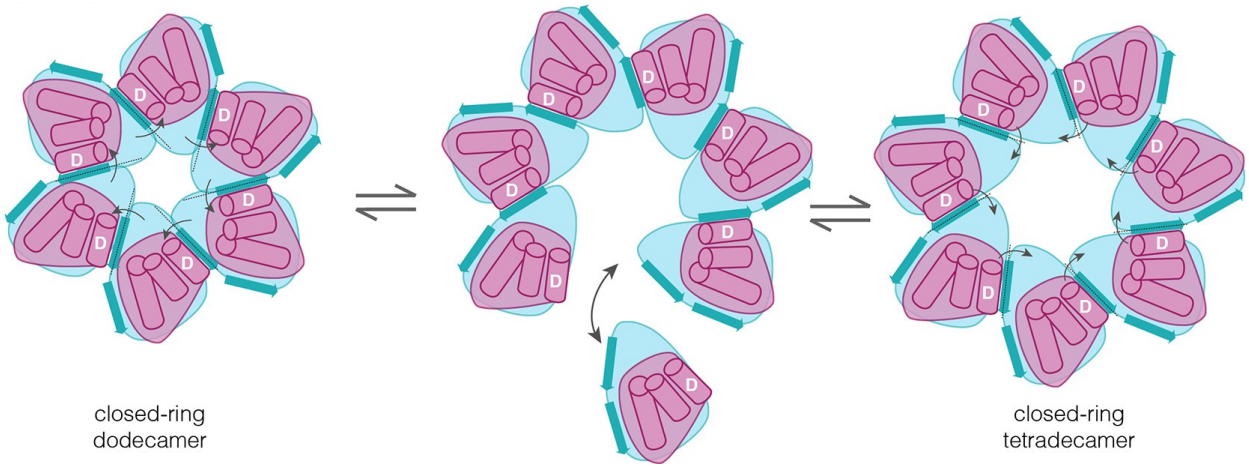

Figure 1.6. Oligomerization of CaMKII hub domains: the transition between dodecamer and tetradecamer. [53] (CC BY)

Architecture of the Holoenzyme

CaMKII has a unique morphology where 12 kinase domains are attached by unstructured linkers to the core hub assembly. Early TEM images of CaMKII showed a "hub and spoke" arrangement: the subunits were held together by the formation of a central hub of association domains, and the kinase domains were decorated around the hub and described as petals [63] [64]. Afterward, two additional TEM experiments revealed surprisingly different CaMKII structures. While the hub domain showed a well-defined structure comprised of 6 lobes arranged in a symmetric gear shape with a height of 10 nm and a diameter between 12 – 14 nm, class averages of CaMKII particles revealed different locations of the kinase domains[57] [58].

Kolodziej *et al.* described the appearance of kinase domains above and below the stacked hub rings increasing the holoenzyme height to 20 nm and diameter to 22 nm[57]. These extensions had a foot-like shape positioned at a 30-degree angle away from the hub, which similarly describes the bi-lobed shape of the kinase domain (Figure 1.7, panel A). This morphology was subsequently confirmed for the other isoforms beta, gamma, and delta [65]. In contrast, Morris and Török described the kinase domains in a coplanar arrangement around the hub in a 30 nm diameter ring (Figure 1.7, panel B).

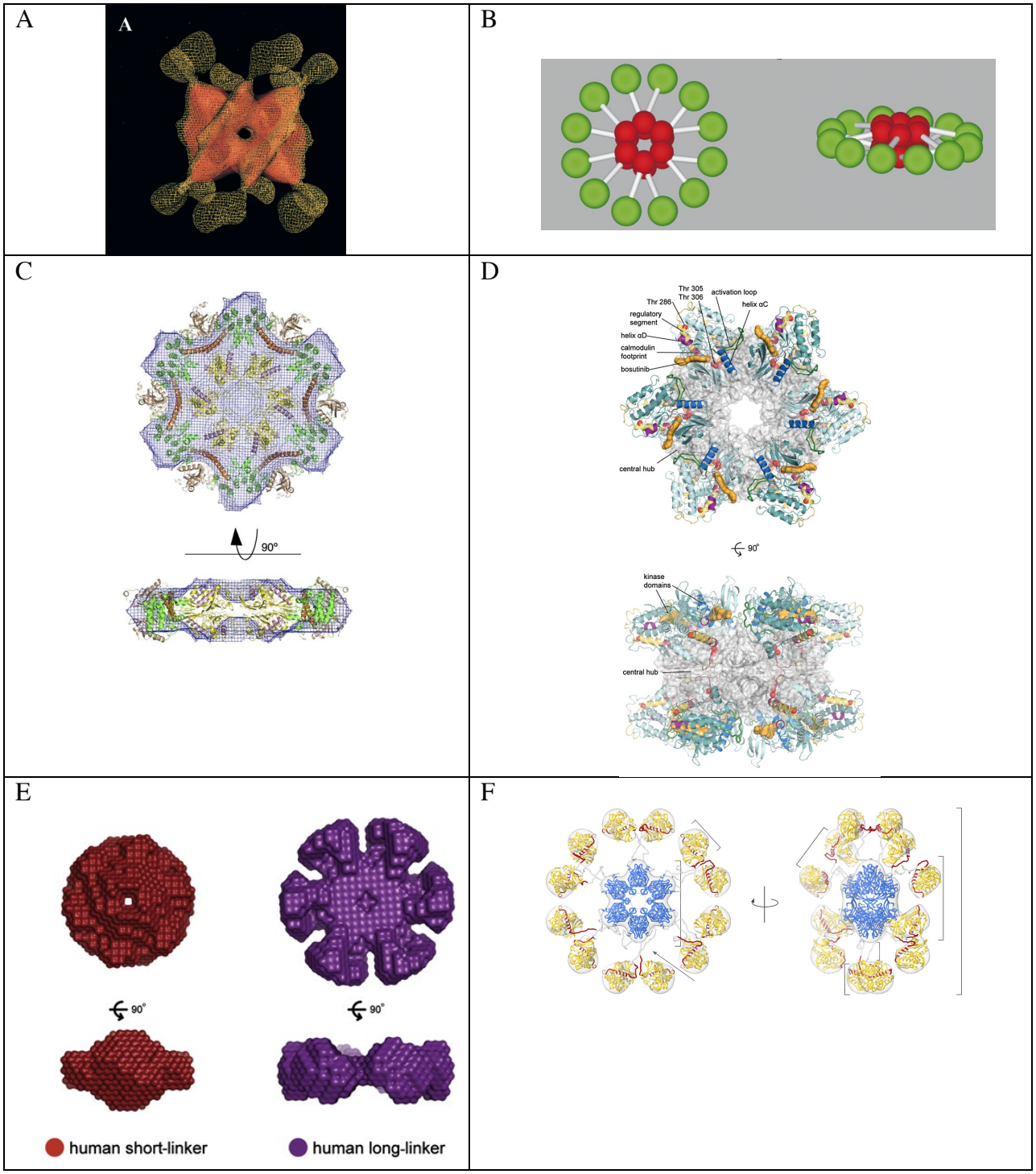

Figure 1.7. Differences in CaMKII Structural Models. A) Random Conical Tilt reconstruction from cryo-EM data [57]. B) Interpretation of shape from negative stain data [58]. C) SAXS shape reconstruction fit to rigid body model [42]. D) Holoenzyme reconstruction from the crystal structure of linker-less subunit [45]. E) SAXS ab-initio shape reconstructions for linker-less (human short-linker) and 30 residue linker (human long-linker) [45]. F) Pseudo-atomic model derived by mapping crystal structures into the negative stain density and modeling the disordered linkers[60].

It is surprising that the kinase domains were clearly identified from class averages of particles because the non-uniform placement of those domains causes the densities to average into a weak density [63] [62].

The disparity of these two structures and the relationship between structure and linker length prompted further experiments. Rosenberg *et al.* fit small-angle x-ray scattering (SAXS) data of CaMKII in solution to a series of rigid body model projections [42] (Figure 1.7, panel C). SAXS produced an experimental value of 72 Å for the radius of gyration, then a series of models were generated where each of the kinase domains were placed along an arc of travel that spanned between the coplanar location observed by Morris and Török (0 °) and the 10 nm displacement above and below the hub observed by Kolodziej (90 °). The best fit was where kinase domains were paired into dimers and extended in a coplanar ring around the hub. This data confirms the observations of Morris and Török, though it is still likely that both EM structures represent different configurations of the same assembly [59]. When the same SAXS data was used to reconstruct an *ab-initio* shape, the result was a flattened disc where the paired kinase dimers are docked to the perimeter, resulting in a larger 20 nm diameter but only 6 nm thick (Figure 1.7, panel E). This too may be yet another configuration of the holoenzyme.

Rosenberg and colleagues engineered the CaMKII linker to make short and long linker variants that would adopt a compact and extended catalytic arrangement, respectively. Chao *et al.* also employed a short (β7) linker to crystallize the structure of a subunit where the catalytic module and hub domain form an interface (Figure 1.7, panel D). The holoenzyme was rendered by extrapolation with 622 symmetry to match the symmetry used by Kolodziej *et al.* [45]. Interestingly, the kinase domains cannot form a dimer in this conformation, and the authors also suggested that the previous SAXS experiments also did not prove dimerization directly. It was proposed that this conformation represents a fully compact and docked conformation, while prior published data produced extended conformations. The flexible linker would allow equilibrium between the two conformational states. Importantly, the length of the linker was proposed to regulate the amount of strength towards a docked conformation. The authors proposed this given the observation that longer linker isoforms gain activity and have a higher affinity for Ca2+/CaM binding than isoforms with shorter linkers [66]. If the exposure of the regulatory segment is dependent upon access when extended from the hub, then a slower period of oscillation between extended and docked states would give more opportunity for binding and activation. The crystal

structure produced an interesting interaction between the regulatory segment and the hub domain. Part of the R3 segment inserted into a cavity in the hub domain to extend its beta sheet, suggesting that the Ca2+/CaM binding segment is sequestered in the hub domain and hinders activation.

Recently, single-particle electron tomography of negative-stained full-length CaMKII was performed to deduce catalytic module positions surrounding the hub domain [60]. A set of tilted images were captured at a coarse tilt step: 10° increments from 0° to 50°, which is adequate for low-resolution negative stained images. The tilt images were used to attempt to uncover additional 3-D positioning from the preferred face-up orientation of the particles. The authors used non-tilted images to determine class averages by removing the peripheral kinases with a 75 Å outer mask to maximize hub coherence, similarly to previous single particle reconstruction experiments [57, 62]. In this experiment, the non-tilted data also went through a second round of classification where the unmasked particles were filtered by a 50 Å inner mask designed to remove the hub from the class average alignments. Distance measurements between kinase and hub were calculated using the hub radius known from the first round of classification and samples of the kinase locations from the second classification. The results showed that nearly all holoenzymes were found to have an extended conformation. Extending the outer mask to 110 Å to include any kinase density from docked catalytic modules showed no density in the class averages. Additional individual distance measurements found that <3% of the particles were close enough to touch the hub domain. Therefore, the authors argued that the compact conformation occurred for only a minor number of individual catalytic modules and did not form a completely compact holoenzyme. The average distance of the catalytic modules extended from the hub domain was ~27 Å and followed a Gaussian distribution. The majority of these catalytic modules (80%) were separated from each other by an average of ~58 Å in a Gaussian distribution. Catalytic module dimers were found in approximately 20% of the samples, and there was no correlation between dimerization and distance from the central hub. This finding loosely corroborates the previous lower-resolution long-linker SAXS structure [45].

Holoenzyme Dynamics and Cooperativity

One of the most interesting features of the CaMKII holoenzyme is that it exhibits layers of cooperativity. Phosphorylation activity is markedly different between subunit monomers and

the holoenzyme. Truncated catalytic modules do not show cooperativity, and have a Hill coefficient of 0.9 [67]. Cooperativity of at least two subunits activated had a Hill coefficient of approximately 5, compared to individual subunit measurements of Ca2+ binding cooperativity to CaM (Hill slope 3) and Ca2+/CaM binding cooperativity to CaMKII (no cooperation) [67]. It was also shown that adding phosphatase activity to CaMKII activity increases the cooperativity (Hill slope >8) to result in a sharpened switch-like ultra-sensitivity to minute changes in Ca2+ concentration [68]. Various dynamic mechanisms have been proposed to add layers of cooperativity, described below.

Frequency detection

Once activated, a kinase domain in one subunit can phosphorylate neighboring subunits also bound by Ca2+/CaM within the same holoenzyme [69]. This action has been given several names: inter-subunit phosphorylation, intra-holoenzyme phosphorylation, and autophosphorylation in trans. This additional complexity imparts a second layer of autoregulation.

The mechanism for inter-subunit phosphorylation determines frequency selectivity for bursts of calcium occurring during a synaptic event. This is shown graphically in Figure 1.8. When calcium bursts occur at a slow frequency, some CaMKII subunits are activated, but the long "off period" between bursts allows CaM to unbind dependent subunits. Phosphatases also may inactivate active subunits before the next calcium burst. The result is that the holoenzyme may gain active subunits but lose them over the long period between calcium bursts, rendering the oligomer fully autoinhibited. Thus, there are not enough subunits to propel autophosphorylation of the holoenzyme. At higher burst frequencies, the shorter "off period" will still incur CaM unbinding from active subunits, but will rapidly rebind these (and adjacent) subunits before de-phosphorylation. Above the frequency threshold, adjacent subunits become active, dependently or autonomous, such that a chain reaction of inter-subunit phosphorylation activates the entire holoenzyme.

Further, the length of the linker between the catalytic module and the hub domain determines the frequency response to calcium. A long linker enables access to Ca2+/CaM more readily, but at the expense of a larger range of movement away from a neighboring kinase

substrate and slows down the rate of holoenzyme activation. Thus, longer linkers are tuned to lower frequency bursts, and shorter linkers are responsive to higher frequency bursts.

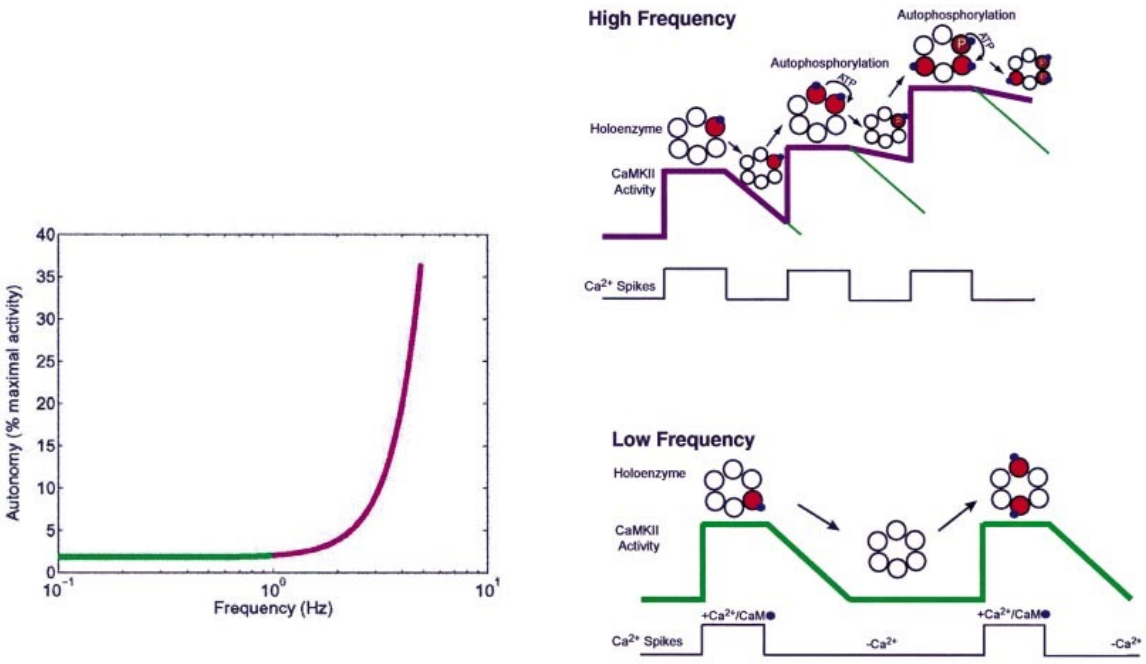

Figure 1.8. Activation frequency sensitivity of the CaMKII holoenzyme. [27]

The major limitation with this model of phosphorylation is that it assumes all subunits gain activity independently and is not a cooperative process. It has been described as a coincidence detection model, where the completed holoenzyme phosphorylation cascade (the detection) is made based on the integration of calcium bursts within a time window (the coincidence). However, Chao 2010 argues against this simplicity because of the known cooperativity of the holoenzyme [67].

Catalytic dimerization inhibits activation

Rosenberg *et al.* produced a crystal structure that showed that a catalytic module dimer forms through an anti-parallel coiled-coil interaction between the two regulatory segments, specifically R2 and R3 [42]. The coiled-coil buries the regulatory segments and blocks activation until separation. It is proposed that activation occurs because dimerization is a weak interaction but supported by the high local concentration of catalytic domains in the holoenzyme. Therefore, upon one subunit gaining bound Ca2+/CaM, the second subunit becomes available for activation.

The potentiation of the second subunit by activation of the first may account for a Hill coefficient >1. Truncated catalytic modules in solution were found to form dimers weakly, with a K_D of 200–600 μM [44]. Still, this idea is controversial, as there is conflicting evidence for the formation of this dimer. It was suggested that catalytic dimers could be an artifact of crystal packing [70]. Early structure data suggested that dimerization does not occur because of the large distance between catalytic modules, effectively 40 – 50 Å, as seen in the RCT reconstruction [57], but data imposing D6 symmetry showing coplanar mirrored catalytic modules, did agree with dimerization [58]. It was also suggested that inter-subunit phosphorylation cooperation required that the ATP domains face each other [44]. Fluorescence tagging experiments found that the extended conformation was predominantly seen, with dimerization of catalytic modules in approximately 20% of cases [60]. The compact conformation was not seen.

Autoinhibited inter-subunit capture

The higher Hill coefficients reported suggested additional cooperation beyond dimerization. It was proposed that the first dimer disrupted and freed from the hub could also dislodge adjacent, inhibited catalytic modules from the hub. Although not bound by Ca2+/CaM, a disruption from the hub propels potentiation and achieves higher cooperativity. Further cooperativity could occur when the regulatory domain of an inhibited but potentiated kinase is captured by its active neighbor and priming the phosphorylation action.

Subunit exchange

It has been reported in a fluorophore labeling experiment that phosphorylated subunits do exchange between holoenzymes [59]. Two populations of autoinhibited CaMKII were incubated in contrasting fluorophores, mixed and activated with Ca2+/CaM and ATP, then characterized for fluorophore colocalization using single-particle total internal reflection fluorescence (TIRF) microscopy. After 50 minutes, 40% of active holoenzymes had colocalization, whereas only 5% colocalization was detected in autoinhibited holoenzymes. Exchanges also occurred multiple times. It was also shown that both the wild-type linker and the truncated linker gave equal colocalization. Thus, linker length was not important to colocalization. Another experiment proposed that the regulatory segment sequestered into the hub assembly in-between vertical hub

dimers to "wedge open" the vertical space between two hub dimers [53]. The exchange was proposed on weak lateral interactions that could facilitate opening the hub assembly into a C-shape then re-anneal back into a ring shape. The affinity of the regulatory segment for the kinase domain (IC_{50} ~1 μM) is stronger than that of the hub (100–50 μM), which suggests that only autonomous subunits could volunteer dislocated regulatory segments to the hub. This exchange mechanism would foster inter-holoenzyme activation and extension of the active state beyond the lifetime of any single holoenzyme.

1.5 Purpose of the Study

The specific problem is that the experiments conducted to-date yield holoenzyme structures that are impacted by the method of observation and may not yield a true representation of its quaternary conformation. Specific to these reports:

- X-ray crystallography methods required removing the linker and packing the catalytic module and hub domain together so that the subunit could be crystallized. This conformation may not represent a full-length subunit docking conformation. The structure also imposes D6 symmetry, and therefore no inter-subunit conformational effects can be determined because the 12-mer is created from the dihedral symmetric mapping of an independent subunit to the rest of the structure.
- SAXS measures the scattering spectrum of monodisperse particles in solution. Therefore, the macromolecule must adopt a discrete number of conformations to be able to de-convolve the compound spectrum. For CaMKII, this becomes a problem set of 13 interdependent particles (the assembled hub plus 12 catalytic modules), which is very difficult to resolve. The rigid body model used to synthesize SAXS projections may not robustly describe the structure.
- The sample preparation process for negative stain TEM can deform non-rigid protein shapes. For CaMKII, catalytic modules may be flattened away from the hub from the forces of stain and dehydration, and catalytic domains that collide during solvent wicking may be interpreted as dimers when in fact they are not. The hydrophilic carbon support required for negative stain also encourages CaMKII to adopt a face-up preferred orientation, which may be why only this view is picked for 2D class averages. Lastly, negative stain TEM limits resolution

because the contrast is formed from the edge of stain avoidance around the protein.

- The 3D density map computed from cryo-EM data differs dramatically in thickness from the other methods of observation and was limited to 30 A resolution, less than the negative stain map. The cryo-EM particles were picked using a template of projections from the negative stain reconstruction, which likely imposed model bias on the reconstruction.
- It is proposed that the 3D density map generated from negative stain tomography does not fully represent the dynamics of the quaternary structure because of the same limitations mentioned for single-particle negative stain TEM. The coplanar arrangement of the catalytic subunits may be an artifact of the staining and dehydration process.

Therefore, the purpose of this study is to examine the quaternary structure of autoinhibited full-length human CaMKIIα by cryo-EM to reveal the potential equilibrium between extended and compact conformations with a full-length linker as well as the presence or absence of kinase dimers in this equilibrium. The key to the success of this study is the preparation of CaMKIIα samples that can form quaternary structures without bias from the sample preparation method. Gaining an unambiguous view of catalytic module placement within the holoenzyme will shed light on the mechanisms of inter-subunit phosphorylation and as well as its regulatory role in the PSD.

CHAPTER 2. TEM AND SINGLE PARTICLE ANALYSIS OF CAMKII ALPHA USING FUNCTIONALIZED LIPID AFFINITY GRIDS

2.1 Introduction

Cryo-EM is a technique that has revolutionized structural biology within the last ten years and can elucidate biological structures with resolutions comparable to x-ray crystallography. While cryo-EM has been around for decades, it was only within this timeframe that groundbreaking advances in imaging sensitivity have pushed the resolution of structures into the atomic range. The enhanced resolution comes in part from the use of a direct detection device (DDD), a chip with an ultra-sensitive CMOS surface capable of detecting single electrons down to sub-pixel resolution [71]. The DDD also has rapid scanning and readout that enables the detected electrons to be output individually as a dose-fractionated movie. Since the TEM grid and sample are not completely conductive, the initial electrons from the beam can charge the sample surface and induce significant motion. Although most of the drift occurs during the initial dose, there still is residual drift throughout the entire acquisition time [72-73]. If the movie frames are integrated into a single frame similarly to a CCD camera, then image blurring and loss of high-frequency detail occur. Fortunately, the DDD movie may be aligned in post-processing by a global motion compensation algorithm followed by integration to produce a single image with increased contrast [74]. Another improvement coupled with the DDD is the energy filter (EFTEM), which blocks inelastically-scattered electrons from detection, These elections have a non-deterministic path due to the partial absorption of energy from collisions with atoms in the sample. These random electrons increase background noise and can reduce the signal-to-noise ratio in half [75].

Once high-quality image data has been collected, single particle analysis algorithms are used to align similar particles grouped by orientation to amplify their contrast. A representative set of 2D orientation projections is then used to back-project onto a 3D template that then becomes an initial model for the reconstruction. Templates include ab-initio random spherical shapes as well as a priori models from x-ray crystallography, negative stain TEM reconstruction,

random conical tilt or tomography models. Individual particles are then finely mapped back onto the initial model to improve detail and resolution. Two excellent reviews of the single-particle cryo-EM workflow are listed here [76-77].

Many software choices now exist for processing TEM movies and 3D model construction, including integrated workflow environments such as Appion, RELION-3, cisTEM, and EMAN2 [78-81]. These applications pull together discrete tasks into a common software environment and minimize the conversion of data between tools. Tasks in the workflow include including movie alignment, defocus estimation, CTF correction, particle picking, 2D class averaging, model building and refinement, and resolution validation.

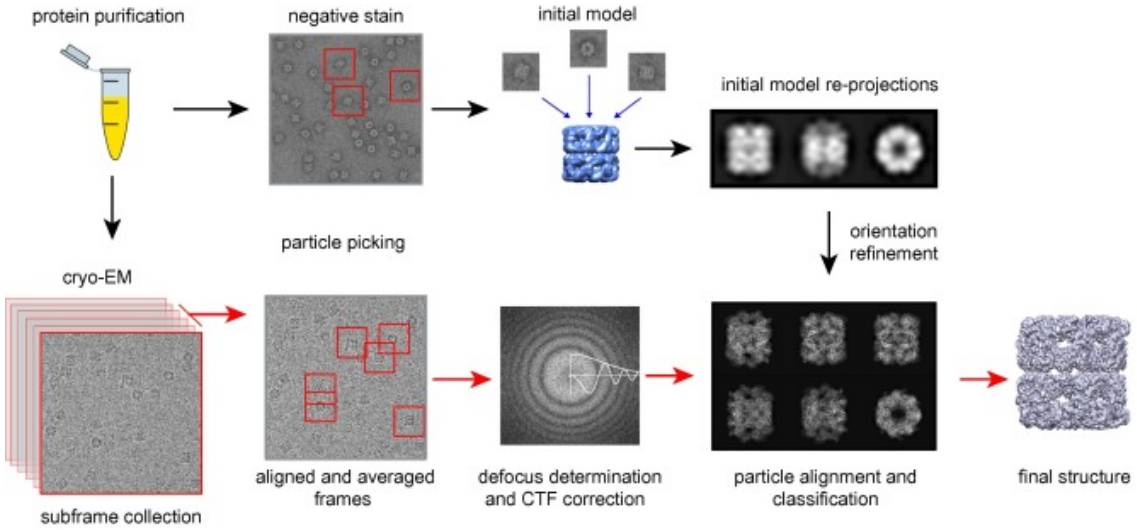

Figure 2.1. General cryo-EM workflow. Adapted and modified from Carroni, M.; Saibil, H. R. *Methods* **2016,** *95*, 78-85[82].(CC BY)

The most challenging, and least automated, aspect of the cryo-EM process is sample preparation. The preparation of cryo-EM samples often requires much empirical iteration to find successful conditions. Buffers that stabilize protein folding or complexation, additives to resist aggregation, reducing agents and chelators that improve sample stability often have a negative effect in cryo-EM because they can interfere with proper ice formation and reduce contrast. Some excellent TEM sample preparation reviews are listed here [77, 83-86].

Producing data for single particle analysis typically involves three steps: biological specimen preparation, followed by negative stain TEM, then finally cryo-EM. For the first step, the buffer composition mentioned above must be optimized while maintaining an adequate

particle concentration. A low concentration will produce fewer particles per target image, increasing the number of images that must be collected and increasing the burden of post-processing. Additionally, the specimen in the sample should be homogenous to reduce the burden of removing unwanted particles or specimens that have been compromised by debris. In the second step, negative stain TEM is used to verify particle morphology and heterogeneity either by conformational variations or sample contamination. When successfully processed, the results can provide a particle-picking template for cryo-EM images and offer a low-resolution 3D initial model for reconstruction. In the third step, grid choice, sample application and, parameters must be optimized to form vitreous ice with optimal thickness to support high-quality image collection. After the identification of proper ice formation conditions and visible particles on the grid, a second round of optimization follows to fix these common problems:

1. charged surface areas on the particle may preferentially adsorb to the carbon support and fix orientation to one or a limited number of views,
2. charged particles may adsorb entirely to the carbon support and not to thinner sections used for imaging,
3. hydrophobic patches on the particle may adsorb to the air-water interface, where strong hydrophobic forces can denature tertiary structure [87] [88], and
4. sample deposition and blotting may encourage particle self-association.

Charged adsorption and particle self-association can potentially be minimized by adjusting the buffer pH or by manipulating glow discharge settings to alter grid hydrophobicity. Changing support material from carbon support to graphene, for example, can also improve sample dynamics. Adsorption to the air-water interface may be altered by introducing a non-ionic detergent that, at its critical micelle concentration (CMC), will self-assemble into a surface monolayer. This will shield the air-water interface and instead present a hydrophilic interface to limit particle deformation [89].

2.2 TEM of CaMKII

As discussed in Chapter 1, the quaternary structure of the CaMKII autoinhibited holoenzyme may vary greatly dependent upon the placement of the catalytic modules. A face-up particle orientation could potentially vary from 20-30 nm and could exhibit a star-like face with

extended catalytic modules, or it could appear as a disc with catalytic modules docked to the hub. A side-view orientation could vary in thickness from 6 nm with no pore to 20 nm with one or two pores. The primary observation is that the morphology obtained from each TEM experiment appears to be dependent upon both staining and the grid type. A list of TEM experimental conditions is shown in Table 2.1.

Table 2.1 Reported TEM Experimental Conditions. Legend: NS – negative stain TEM; RCT – random conical tilt; NST – negative stain tomography; CEM – cryo-EM

Ref	Experiment	Grid	Conc. (μg/mL)	Voltage (keV)	Å/pix	Dose ($e^-/Å^2$)	Defocus (μm)
Kanaseki[63]	NS	Mica	n/a	80	n/a	50	n/a
Rosenberg[62]	NS	Carbon	15-30	200	1.9	n/a	2 3
Bhattacharyya[53]	NS	Carbon	15	120	2.2	35	0.8 1.5
Kolodziej[57]	NS RCT	Carbon	15	100	5.7		0.5 1
Myers[60]	NST	Carbon	15	120	4.4		1.5 2.5
Kolodziej[57]	CEM	Holey carbon	70	100	5.7	9	1.7
Rosenberg[62]	CEM	Carbon	150	300	2.2	20	2 5
Myers[60]	CEM	Holey carbon	56	300			3 5

An interesting conclusion from the reported TEM findings is that side views are not well represented; only Kolodziej *et al.* observed a side view directly. One observation is that they were the only group to report data generated from holey carbon grids that do not have any support surface to encourage face-up particles. Myers *et al.* did report the use of holey carbon grids but did not show any image data. Additionally, only Kolodziej *et al.* and Myers *et al.* computed side views from tilted images, but both were from negative stain data. Therefore, to aid in finding CaMKII particles in a variety of orientations, 2D projections were generated using density maps from reported structures that included opposing states of the compact-extended equilibrium. The linker-less compact holoenzyme from Chao *et al.* (Figure 2.2A) and the extended-conformation holoenzyme from Myers *et al.* (Figure 2.2B) were both filtered to 20 Å and projected at 4.37 Å/pix in 15° increments using D6 symmetry and shown as pseudo-class averages. The linker-less hub appears larger than the extended-conformation hub due to the added catalytic domains docked at each gear point. Interestingly, neither set of projections produces a two-pore side view as observed by Kolodziej *et al.*

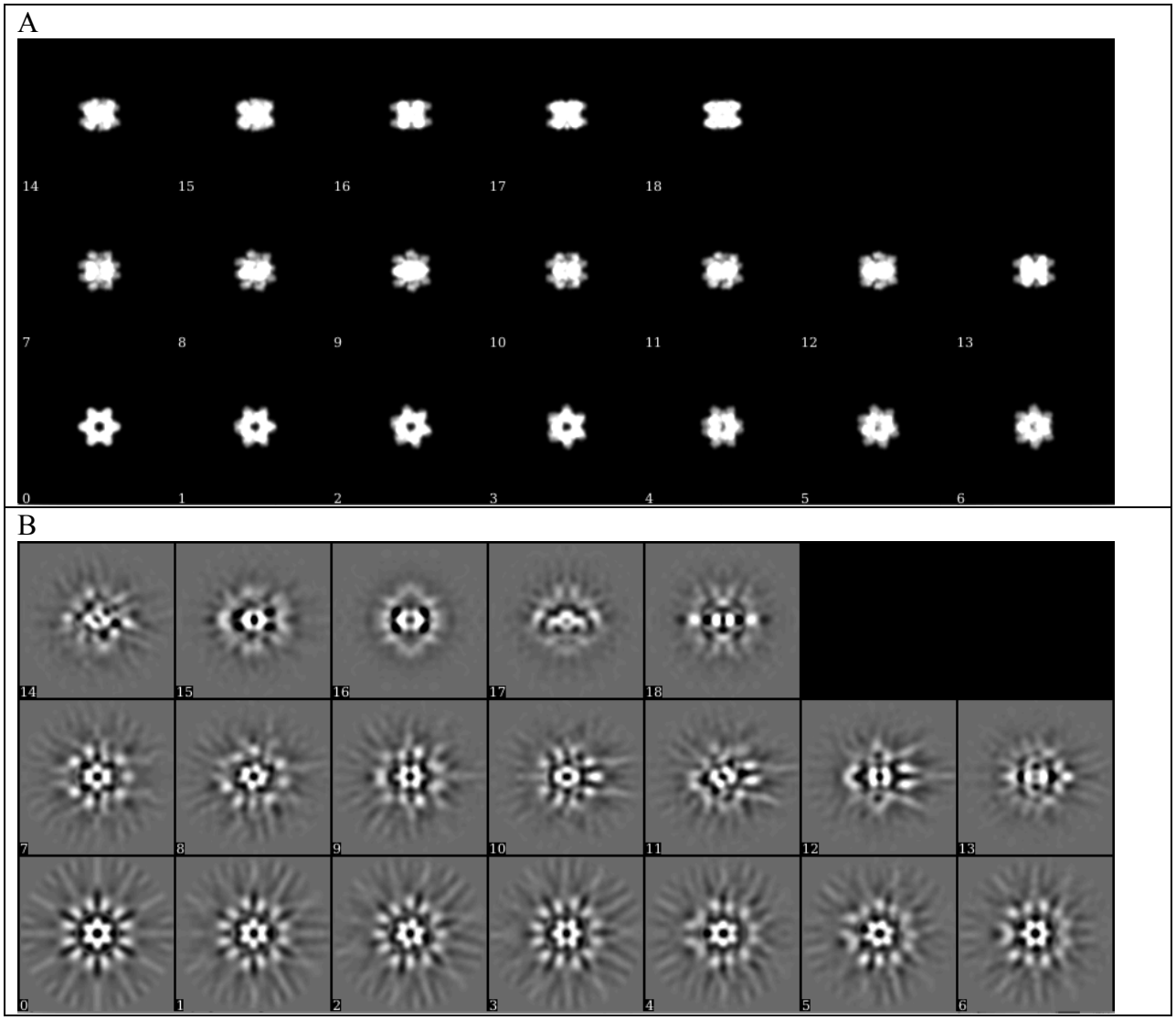

Figure 2.2. Comparative 2D projections of A) CaMKII compact conformation crystal structure (PDBID 3SOA) and B) CaMKII extended conformation electron density map from negative stain tomography (EMD-8514).

2.3 20S Proteasome Structure Example

To demonstrate the correct functionality of the negative stain TEM workflow, a test experiment with a known, good sample was conducted. This test included grid preparation, microscope operation, and single particle analysis. The 20S proteasome is commonly used to gauge the effectiveness of new EM methods [90]. Here, we used commercially available purified 20S.

2.3.1 Materials and Methods

Human 20S proteasome (Boston Biochem) at 150 μg/mL in buffer comprised of 50 mM HEPES, pH 7.6, 100 mM NaCl and 1 mM DTT was mixed with 150 μg/mL BSA (Sigma) at a 1:1 20S:BSA molar ratio. Electron microscopy samples were prepared with either 20S alone or with the 1:1 20S:BSA mixture. Ultra-thin, continuous carbon film topped lacey carbon TEM grid (#01824, Ted Pella) was glow discharged for 30 s at 15 mA using a PELCO easiglow discharge system. Immediately after glow discharge, 3 uL of sample was applied to the carbon side of the grid, followed by 2 drops of buffer wash. Two sequential drops of PTA stain were incubated for 20 sec, then wicked dry. Micrographs were taken on a Philips CM200 TEM equipped with FEG operating at 200 keV. Defocus ranged from -0.3 μm to -4.0 μm.

2.3.2 Results and Discussion

The 20S was found to exhibit preferred adherence to the lacey carbon support (Figure 4.1 panel A). Therefore, we added BSA to the sample to compete for the thick carbon and encourage the 20S to spread over the lacey carbon holes (Figure 2.3 panel B) [86].

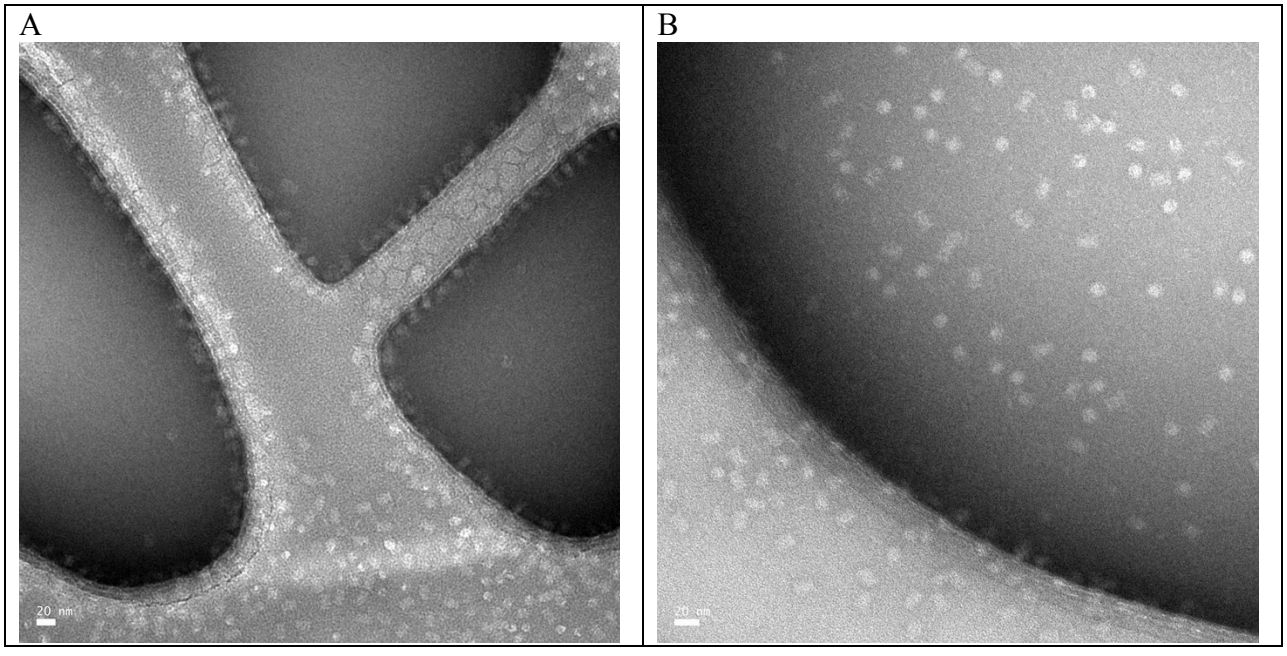

Figure 2.3. Representative micrographs of negative stain 20S on carbon-coated lacey carbon. A.) 20S protein is largely adsorbed by the lacey carbon support and not over the holes. B.) A 1:1 mix of 20S and BSA limits adsorption over the lacey carbon and encourages 20S to spread over the holes.

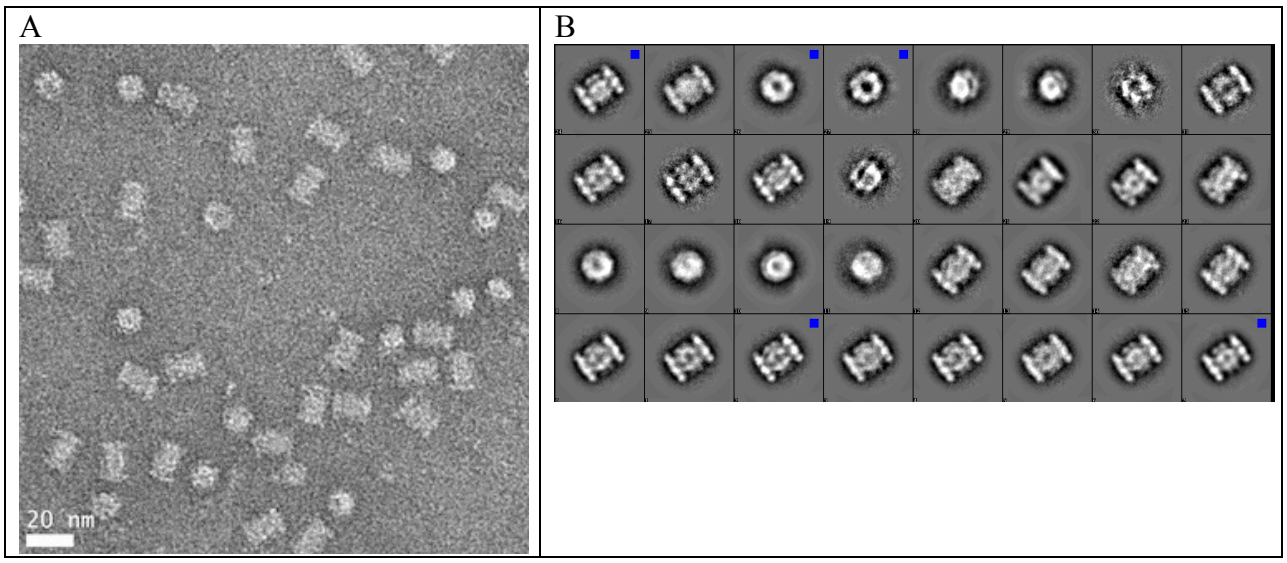

Figure 2.4. 20S particles used in 3D reconstruction. A.) Representative micrograph showing stained particles on ultra-thin continuous coated lacey carbon. B.) 2D class averages, with blue squares indicating classes used for reconstruction.

To perform the reconstruction, 33 micrographs were captured and imported into EMAN 2.1 for processing [81]. A total of 8984 particles were picked automatically due to the high contrast exhibited by the stained sample. 2D classification was performed and is shown in Figure 2.4 panel B. The resulting class averages included 2 well-defined top-view representations and multiple side-view representations with the rest of the classes representing incoherent particles compromised by noise or contamination. The clearest classes, two top-view classes and three side-view classes shown with blue squares, were used to generate an ab-initio 3D model with D7 symmetry applied. The model was refined using the particle set and resulted in a model with 14.9 Å resolution as determined by FSC gold standard (0.143 criteria).

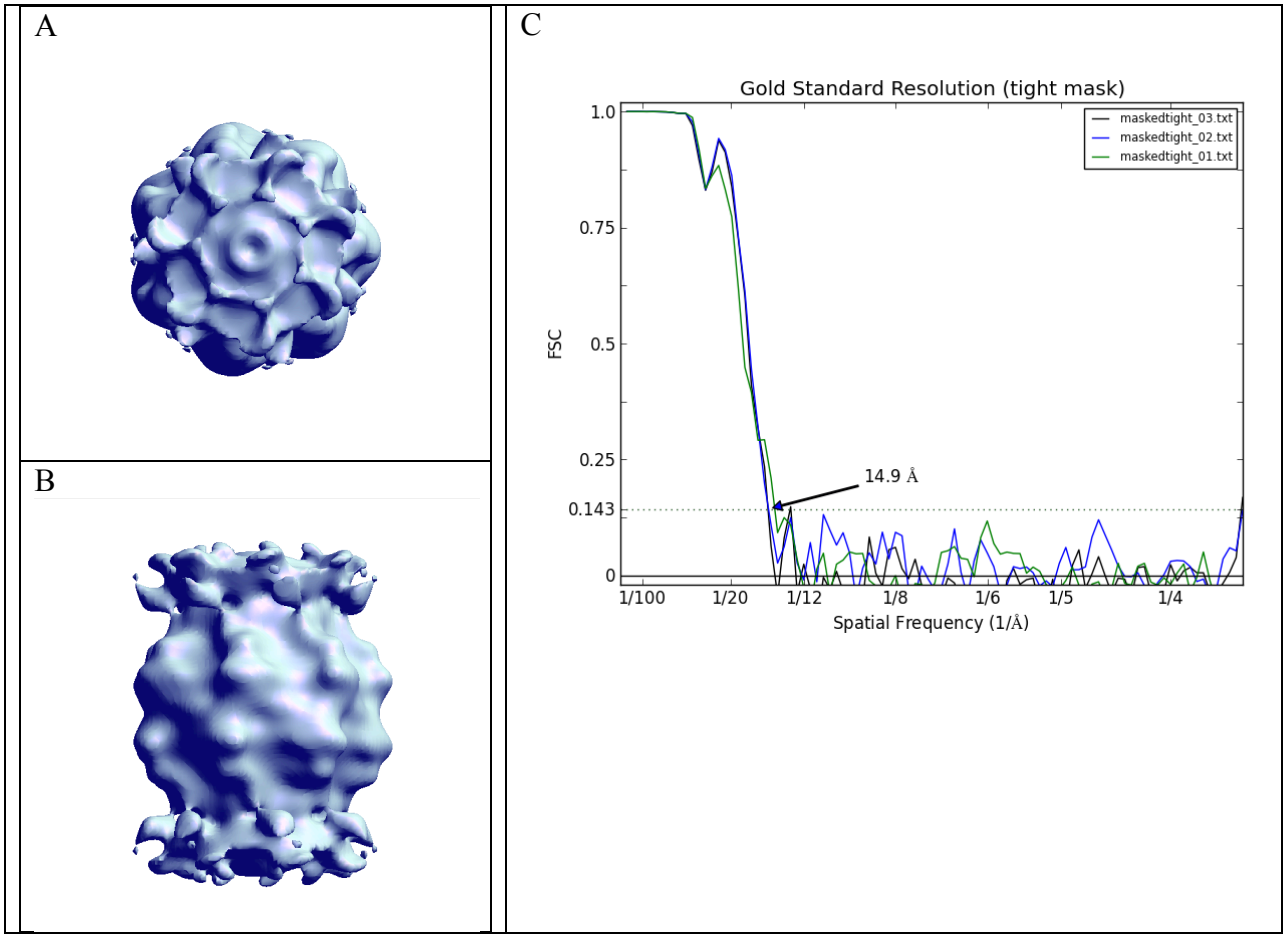

Figure 2.5. Reconstruction of 3D density model from 20S negative stain data. A.) Top view and B.) Side view. C.) Gold standard Fourier shell correlation (FSC) analysis shows that the reconstruction achieved approximately 15 Å resolution.

Overall, the visibility and contrast of the negatively stained particles enabled a low-resolution 3D density model that agrees with published structures [91]. We concluded from this experiment that the workflow of EM sample preparation, imaging, and data reconstruction was viable for experiments with CaMKII.

2.4 TEM of CaMKIIα using an Affinity Grid

A preliminary goal was to demonstrate the use of monolayer affinity grids to selectively capture and enrich CaMKII holoenzymes on the TEM grid surface. The Thompson lab has developed two affinity grid materials to improve sample preparation for cryo-EM: functionalized

anti-fouling lipid monolayers and functionalized graphene oxide sheets [92-93]. In the next section and Chapter 3, we investigated the use of these materials in the cryo-EM sample preparation workflow.

The affinity grid serves two purposes: to enrich the specimen concentration and to hold the specimen close to the grid surface to avoid the air-water interface. When selective capture ligands are coupled with an anti-fouling monolayer, nanoscale purification of the specimen is possible during capture and enrichment. Affinity ligands tethered by a longer linker can also minimize contact with the anti-fouling surface and potentially reduce preferred orientation. Therefore, recombinant proteins fused with an affinity tag, selectively captured directly from expression lysate while non-specific debris is washed away from the anti-fouling surface. One of the benefits of affinity chromatography is the enrichment of target protein. This can be duplicated with the affinity grid by sequentially incubating drops of lysate (mobile phase) on the grid surface (stationary phase). Lastly, the affinity grid supports washing steps to remove debris and exchange into a cryo-EM buffer for vitreous ice formation.

Affinity grids require a continuous coating of hydrophobic carbon or graphene to support the attachment of the monolayer. The carbon thickness supporting the monolayer over the holes limits the amount of contrast in the images. While thick carbon-coated copper mesh grids may be used for negatively stained samples because of the high contrast stain, holey or lacey carbon grids containing an additional ultra-thin continuous carbon coating are more commonly used in cryo-EM. A schematic of this is shown in Figure 2.6. A copper or gold mesh grid with perforated carbon support is coated with an ultra-thin layer of continuous carbon (<4 nm) or a monolayer of graphene (<1 nm) to provide support over the holes. The lipid monolayer is comprised of a mixture of predominantly short anti-fouling PEG-lipid and a small amount (typically 1%-5%) of functional PEG-lipid and that has been compressed into a brush regime by Langmuir trough. The monolayer is then adsorbed onto the hydrophobic carbon grid surface by Langmuir-Schaefer transfer.

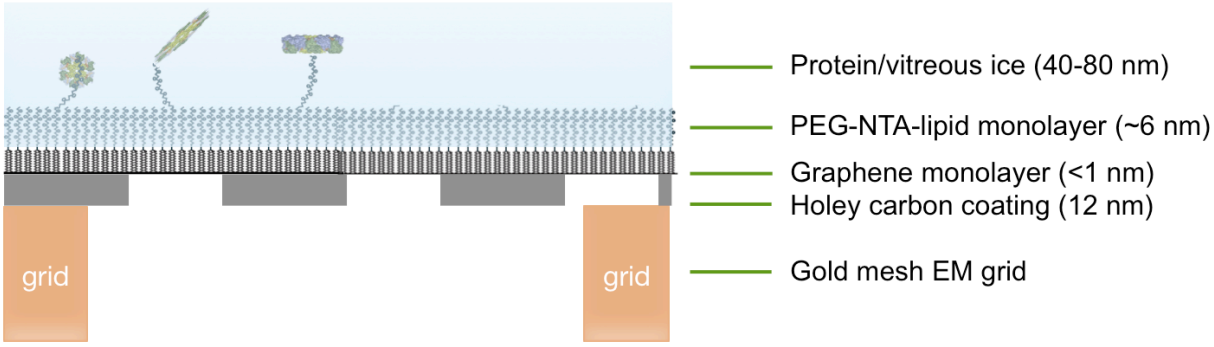

Figure 2.6 Composition of a Ni-NTA affinity grid having anti-fouling properties.

A potential disadvantage with the affinity grid method is the background noise added to the particle images, and discontinuities of the monolayer can create a strong contrast that makes automated particle picking challenging. In spite of these considerations, a 22 Å reconstruction of the 50S ribosomal subunit (approximately 1.6 MDa) from ~26,000 particles was reported [94].

In summary, the lipid monolayer affinity capture experiments of His-tagged GroEL, the potential of nanoscale purification of His-tagged CaMKIIα from lysate, and the potential of reduced preferred orientation motivated us to pursue experiments with this technique.

2.4.1 Materials and Methods

Expression of the tagged protein CaMKII was performed in E. coli BL21(DE3) cells. Cultures were grown to log-phase at 37°C in LB broth with shaking at 250 RPM. The culture was then cooled to 10°C and 1 mM IPTG was added and mixed briefly. Cultures were then incubated with shaking at 250 RPM overnight at 18°C. Cells were pelleted at 3000 x g for 15 min at 4°C, washed once with TBS, then pelleted again and flash frozen in LN2 at stored at -80°C. Cell pellets were thawed and suspended in cold lysis buffer (25 mM HEPES, pH 8.0, 150 mM NaCl, Roche cOmplete protease inhibitor, 0.1 mM PMSF, 1 mg/mL lysozyme, 1 mM DTT, 0.01% Tween 20) and allowed to incubate for 1 hr at 4oC. Following incubation the, cells were mechanically lysed on ice and pelleted at 15,000 x g for 10 min at 4°C. The clarified supernatant was reserved on ice and used immediately in affinity grid preparation.

For experiments using purified CaMKII-6xHis, lysate, as prepared above, was incubated with CaM-Sepharose as reported earlier into a final buffer of 40 mM Tris pH 7.5, 1 mM DTT,

200 mM NaCl and 2 mM EGTA [95]. Total protein concentration for the purified sample was 0.142 mg/mL as measured by Bradford assay.

Tris-NTA affinity capture TEM grids were prepared by the Langmuir-Schaefer transfer method. Briefly, a lipid mixture comprised of 95 mol% DSPE-mPEG(350) (Avanti Polar Lipids) and 5 mol% DSPE-PEG(2000)-trisNTA in chloroform was prepared at 10 mg/ml stock concentration. 3 μL of the solution was deposited on 25 μL of H_20 and allowed to rest for 10 min. Compression was applied to 50 mN/m (monolayer failure occurred at 60 mN/m). Graphene-coated Quantifoil grids (Graphenea) were inverted to face the air-water interface, touched to the compressed lipid for 1 s then allowed to dry. The trisNTA ligands were activated by incubating the grid inverted over a 25 μL drop of 10 mM $NiSO_4$ solution. Excess nickel was removed by inverted incubation over 3 water droplets. Nickel-activated grids were incubated on a 25 μL drop of clarified lysate for 10 min at 4°C. The grid was then washed 3 times by inverted incubation over 25 μL drops of lysis buffer. The incubation and wash steps were repeated 3 times to enrich the affinity capture. Lastly, the grid was washed and buffer exchanged 3 times by inverted incubation over droplets of water before staining or cryofixation using a CP3 plunger with 2.0 sec blot time.

For negative stain TEM, the final wash steps were performed with pure water to eliminate large stain crystals formed in the presence of buffer containing high salt concentration. Samples were stained with 2 drops of UF without blotting in-between steps and only wicked dry at the end. Images were captured using a Philips CM200 containing a 2k X 2K CCD camera controlled by Digital Micrograph software (Gatan) and were recorded at 27,500 X magnification (5.5 Å/pix).

Cryo-EM samples were imaged using an FEI Titan cryo-TEM at 300 keV equipped with a Gatan K2 Summit camera producing 7k x 7k pixel images when set to superresolution mode. Imaging was conducted at 18,000 X magnification (0.8 Å/pix) in low-dose movie mode, with an exposure of 8 e^-/pix/sec for 10,020 ms. Automated data collection was performed using Leginon. Defocus for target images was set to random values between -0.6 μm and -3.0 μm. Movie frames were motion corrected using motioncor2 software and summed to produce images.

2.4.2 Results and Discussion

Clarified lysate from BL21(DE3) expressions was run in SDS-PAGE Western gels and stained with two antibodies for CaMKII: 6G9, a monoclonal antibody that recognizes the N-terminal kinase domain, and a 6xHis antibody that recognizes the polyhistidine tag located at the end of the CaMKII sequence at the C-terminus (Figure 2.7). The Western gels indicate that both full-length protein is detected by both antibodies at 50 kD. The 6G9 gel also shows a band at 35 kD suggesting a catalytic module fragment, and the 6xHis antibody gel shows additional bands near 15 kD. Combining the two fragment masses gives 50 kD which suggests these fragments may be from full-length protein that is cleaved during expression.

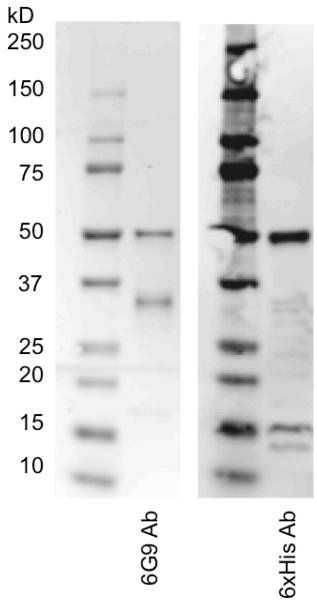

Figure 2.7 Expression Truncation or Cleavage when expressed in BL21(DE3) cells. Western gels show full-length CaMKII at 50 kD, ~35 kD N-terminal fragment (left) and ~15 kD C-terminal fragment (right).

Affinity Grid Negative Stain EM

Images showed largely monodisperse particles, ranging from 20 nm – 30 nm in diameter, and were distinctly visible from the background, but some aggregation was seen and was identified by larger dark patches of stain that encompass the aggregation (

Figure 2.8). There were also a small number of rectangular particles showing two parallel densities sandwiched together. A representative list of particles picked from images is shown in Figure 2.9. The apparent sizes of the particles were larger than previously reported for full-length

holoenzymes (20 nm) or the hub domain (13 nm), but this could be a factor of the negative staining process. Negative stain occurs around the outer perimeter of the particle and the process of staining and dehydrating the surface can flatten flexible proteins. Even with these deformations, the particles still exhibited the characteristic ring shape and were considered a positive result. Interestingly, there were particles identified that could be considered a side-view or axial view of CaMKII. Thus, the experiment suggested further analysis with cryo-EM.

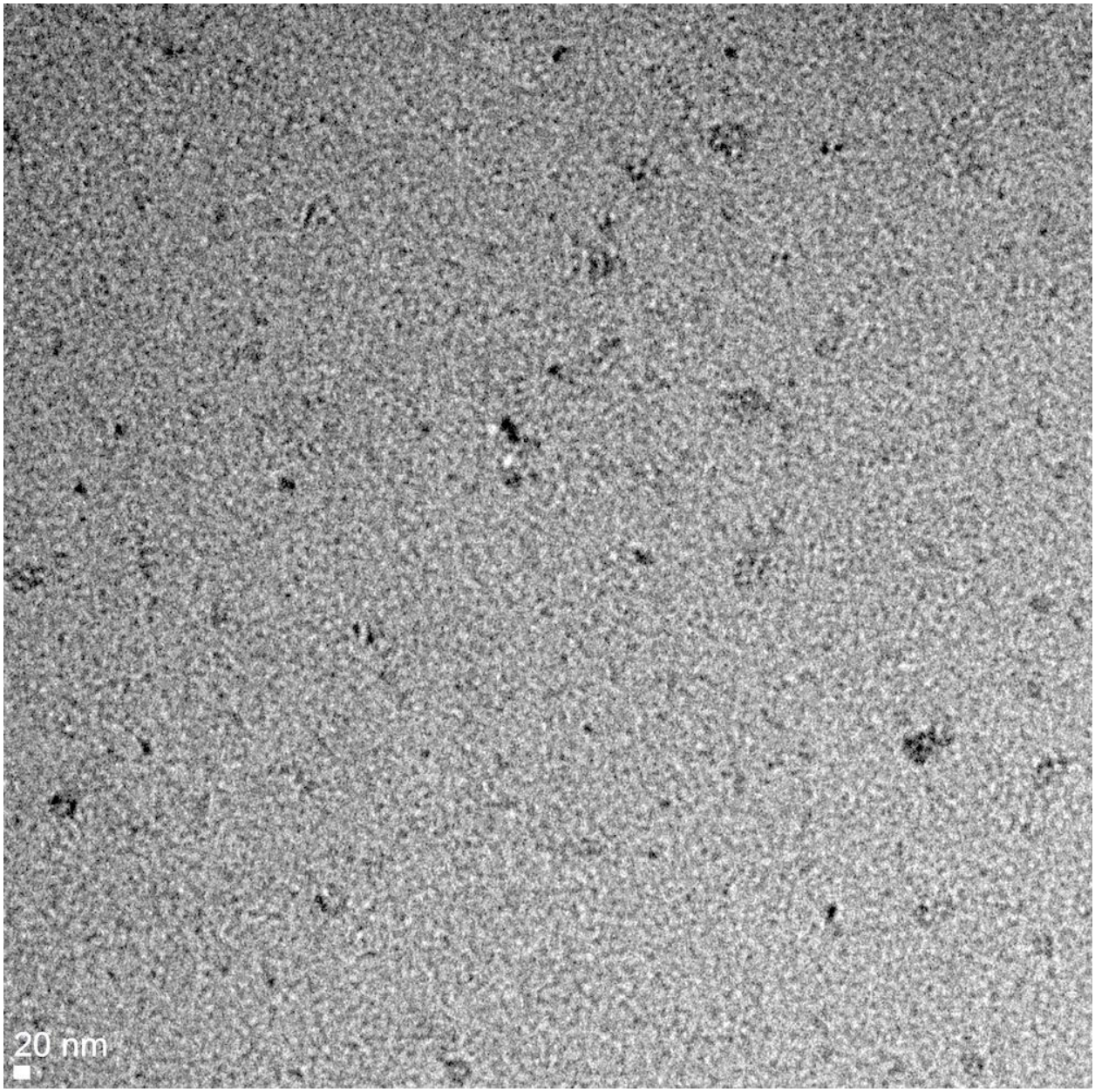

Figure 2.8 Representative image of CaMKII-6xHis captured from lysate onto Tris-NTA affinity graphene support grid stained with uranyl formate.

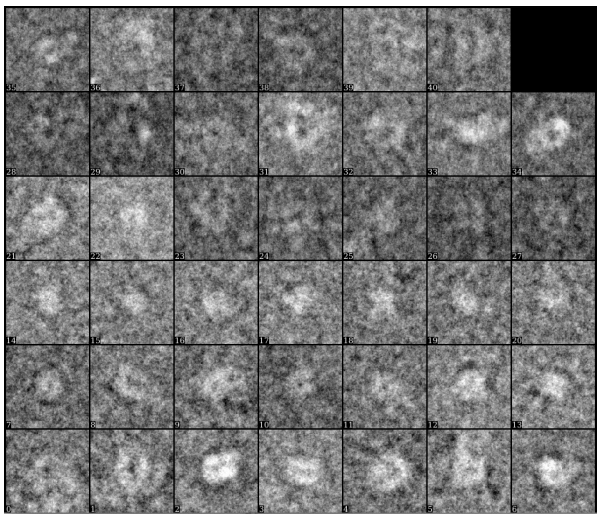
Figure 2.9 CaMKII-6xHis negative stain particles.

Affinity Grid Cryo-EM

In contrast to the negative stain images, CaMKII particles were challenging to discern from the background because there was little contrast. There were, however, many images containing particles that were surrounded by a large halo of dark contrast, which was unexpected. A possible explanation for this unusual feature is the compression of the particle into the monolayer during blotting. Also, streaks of light contrast were present in all the images, likely from the presence of residual Tween-20 detergent that could not be washed from the PEG surface. Few particles were monodisperse: most were groups of two or three self-associated hub domains, and large aggregates were found, as seen at the center top of Figure 2.10. Particles were picked manually and are shown in Figure 2.11.

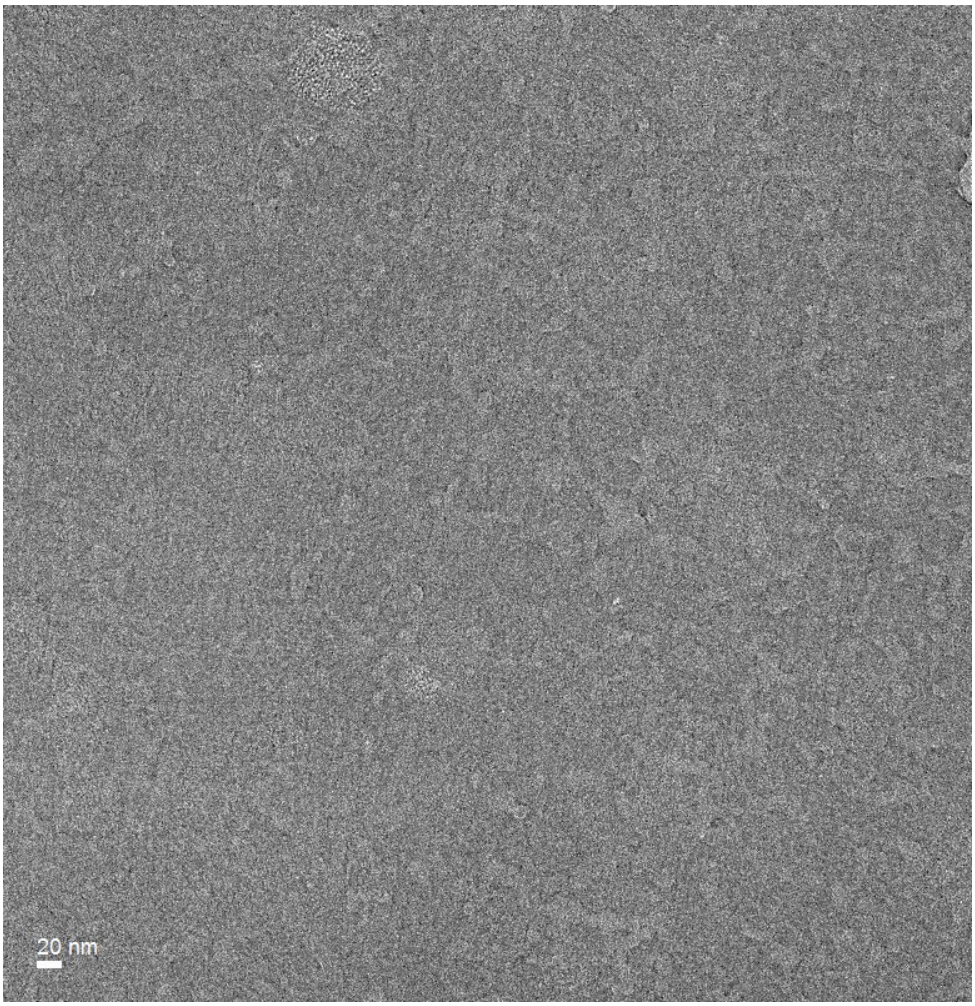

Figure 2.10. Representative image from nanoscale purification of CaMKII-6xHis using Ni- NTA affinity grid cryo-EM.

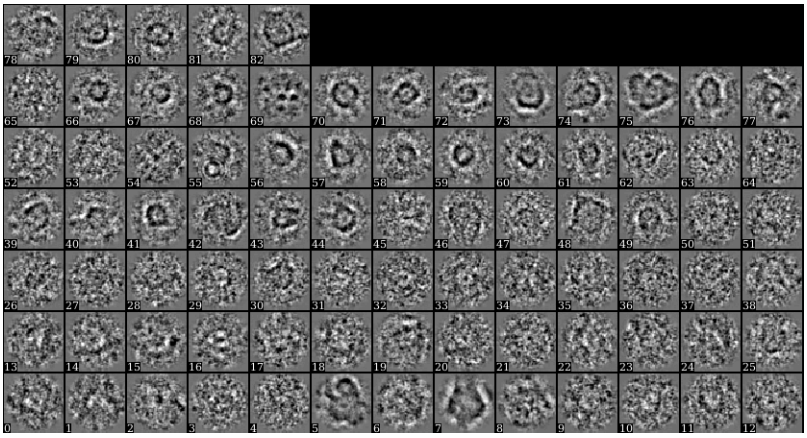

Figure 2.11 Particles from nanoscale purification of CaMKII-6xHis using Ni-NTA affinity grid cryo-EM.

The most consistent ring-like structure appeared to have a diameter of only 6 nm, which is only half the expected size. These particles were also substantially different in size than the ones observed in negative stain EM. Further, the dark halos around many of the particles did not show any consistent spokes radiating from the hub that would be indicative of tethered kinase domains. In conclusion, the images, which did not look like published results, led to a fundamental question: is the affinity monolayer incompatible with a flexible protein like CaMKII, or instead is the sample preparation of CaMKII inadequate for EM?

To answer this question, we split the experiment into two control experiments. The first control experiment was to purify CaMKII-6xHis using Ca^{2+}/CaM-Sepharose, an orthogonal affinity purification technique that would enrich full-length CaMKII in a low-contaminant buffer, followed by incubation of the sample with the Ni-NTA affinity grid. The outcome of this experiment would determine if the Ni-NTA affinity grid ligand was functional. The second control experiment was to apply the Ca^{2+}/CaM-Sepharose-purified CaMKII directly to a hydrophilic carbon grid, which was the preferred technique of published work. A successful result would show our CaMKII matching reported morphology discussed in Chapter 1.

Affinity Grid Cryo-EM with Purified CaMKII-6xHis

Titan results showed a strong background signal and little contrast from particles. Many circular "particles" of widely varying sizes stood out from the background noise, prompting question if these densities were debris or aggregation of denatured CaMKII protein. This was unexpected, considering that the affinity grid was washed 3 times with drops of water. For the few particles that were identified, however, the 2D class averaging yielded noisy classes that retained the characteristic face-up shape of CaMKII, though only the hub domain could be identified (Figure 2.13). It was not possible to identify side-view CaMKII.

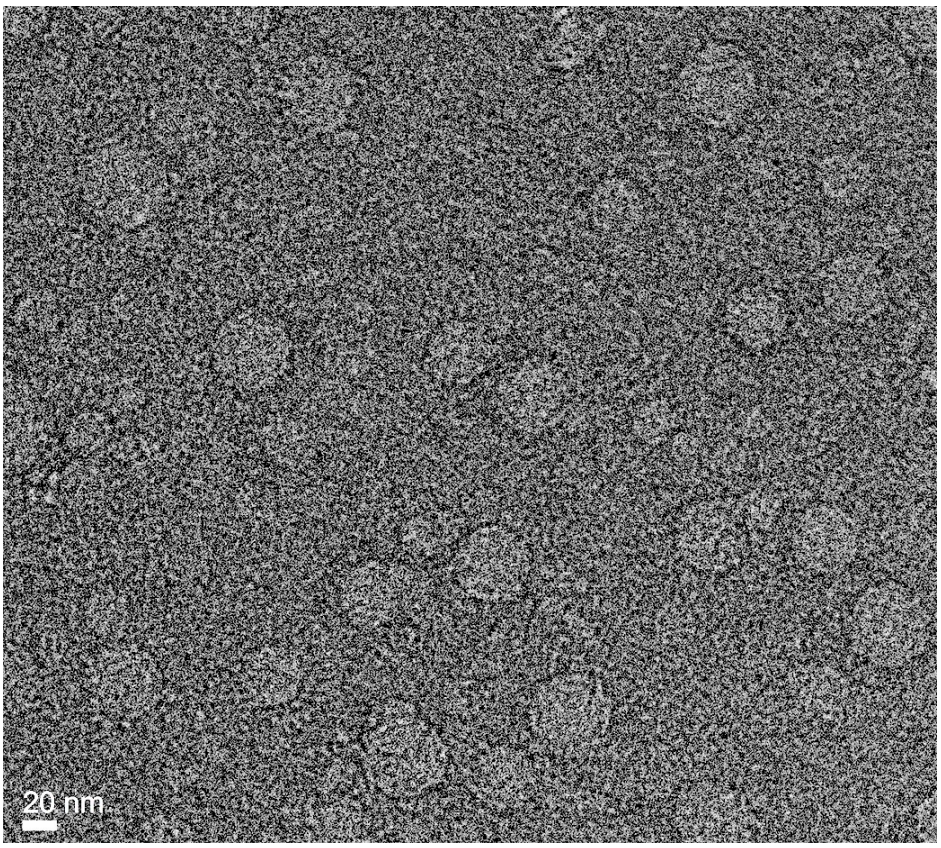

Figure 2.12. Representative image from purified CaMKII-6xHis captured by affinity grid.

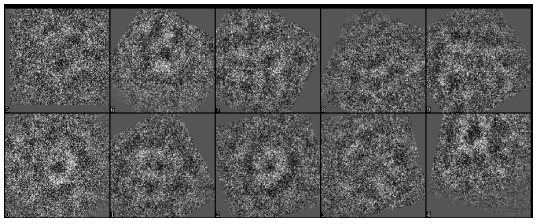
Figure 2.13. 2D class averages of purified CaMKII-6xHis captured by affinity grid.

Cryo-EM with Purified CaMKII-6xHis on Hydrophilic Carbon

For the second control experiment, purified CaMKII-6xHis was deposited directly onto glow discharged ultra-thin lacey carbon grids. In this manner, CaMKII adsorbs to the charged carbon surface, along with other contaminants, and is imaged without affinity monolayer background noise. Images revealed high particle density and strong contrast against the background. Unfortunately, the contrast appeared not as particle density against the background, but instead as a 3–4 nm dark halo enveloping each lighter particle (Figure 2.14). The particles inside the halos varied in size and shape, which suggests that a significant number of particles

may be contaminants. 2D class averaging of a limited number of particles (~600) enabled the sorting of the particles by size and by center pore (Figure 2.15). Five of 20 classes had a noticeable pore, yet the particles had a varying diameter size, indicating there may be differences in assembly. It was possible that some of the differences may be the result of truncated hubs forming 14-mer assemblies, but the lack of clear hub and spoke definition, minimal pore visibility, and the widely variable particle radius did not make this evident.

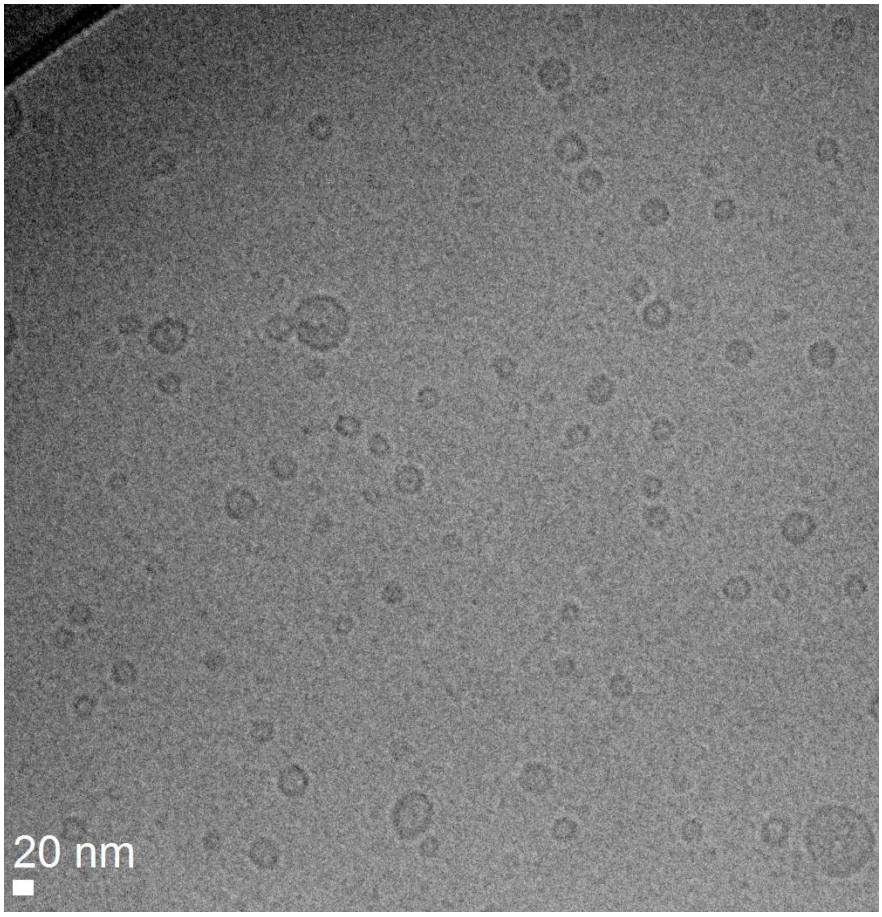

Figure 2.14. Representative cryo-EM image of CaM-Sepharose purified CaMKII-6xHis on hydrophilic lacey carbon grids.

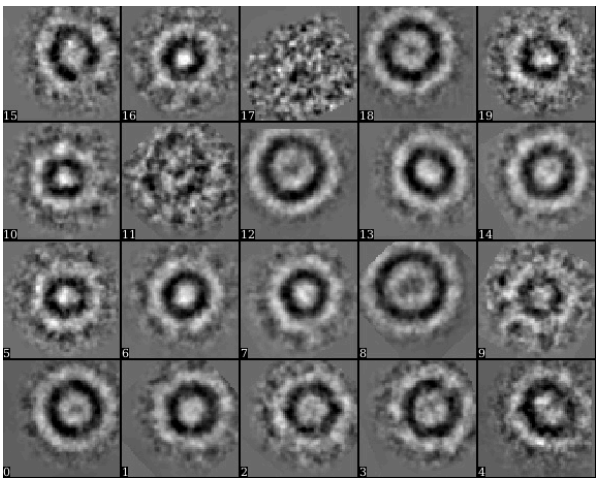

Figure 2.15. 2D class averages from cryo-EM of CaM-Sepharose purified CaMKII-6xHis on hydrophilic lacey carbon grids.

2.4.3 Conclusions

The affinity grids were successful at capturing CaMKII holoenzymes, but it was not possible within these experiments to find conditions that allowed clear visualization of the particles. It was not clear if this limitation was due to lysate debris or effects of the monolayer. It is possible clarification of the lysate using standard centrifugation (15,000 x g) may not generate enough force to remove amphipathic contaminants that could interact with the lipid monolayer and resist washing steps. It is also possible that the lipid monolayer also made it difficult to see the contrast of the hub assembly. Interestingly, it may be that the added density of contamination increased the contrast of the "particles", which may explain why the CaM-Sepharose purified sample failed to reveal much particle contrast. In either case, the addition of strong noise by contaminants and the lack of contrast with the purified sample made it too challenging to create high-resolution, coherent 2D class averages. Our conclusion is that it is certainly possible to find optimal conditions to remove in advance most of the contamination in the buffer and prevent fouling of the lipid monolayer surface, but the holoenzyme may still be at the edge of visible contrast in this environment and thus not optimal for high-resolution reconstruction using the lipid affinity monolayer technique.

The images captured with hydrophilic grids also showed particles of low contrast and significant contamination from the halos. The aberration of the halo made picking particles easier, but the diameter of the halo was 20-30 nm – where catalytic modules were expected to be. When

the evaluation of the biological sample preparation is decoupled from the challenges of the affinity grid, it became clear that the purification technique was not adequate.

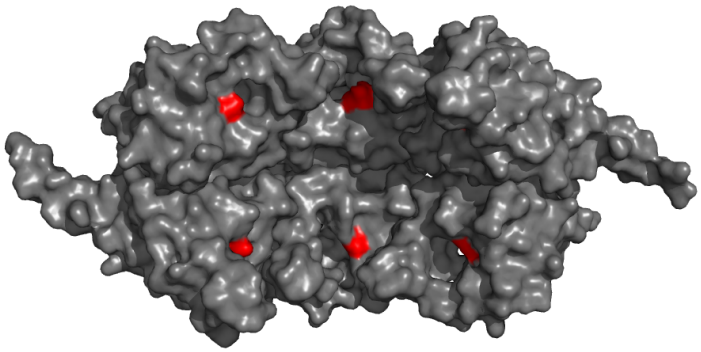

Figure 2.16. Cutaway surface model showing the interior pore of the hub assembly with C-terminal cavities shown in red. Six truncated hub domains (3 vertical pairs) are shown for clarity. The locations of the C-terminals are shown in red. (PDB 1HKX) [61].

The initial recombinant sequence of CaMKII had a 6xHis tag appended to the C-terminus of each subunit (residue 478). Results of Ni-NTA purification with the His tag did not give a high yield in comparison to Ca^{2+}/CaM-Sepharose purification, and this problem had been reported to us by the Waxham lab, who had used a C-terminal his-tag as well (Neil Waxham, personal communication). One possible explanation for the poor yield is the location of the His tag within the hub assembly, shown in red in Figure 2.16. The surface model depicts an interior cutaway of the hub assembly where the C-terminals are receded into cavities within the central pore and are not well positioned for ligand access. CaM-Sepharose purification avoids this problem by binding the regulatory segments along the circumference of the holoenzyme, plus it has a more specific affinity for CaMKII than does Ni-NTA. Lastly, placing the His tag in the hub domain could pose a risk to the correct assembly of the oligomer, especially considering that holoenzymes have a propensity to self-associate even at low concentrations[96]. The class-averaged data shown in these experiments show smooth circumferences of density and not gear-shaped rings, which may be due to smoothing the random dislocations hub domain caused by His-tag interference. The many challenges revealed in these experiments prompted the re-evaluation of two major tenets of the study: that affinity grids are transparent to the electron

beam and give visibility to small or thin particles (less than 250 kDa), and the generation of a homogenous CaMKII holoenzyme sample free of contaminants detrimental to cryo-EM. In the next two chapters, techniques to achieve the above tenets are investigated.

CHAPTER 3. SELECTIVE CAPTURE OF HISTIDINE-TAGGED PROTEINS FROM CELL LYSATES USING TEM GRIDS MODIFIED WITH NTA-GRAPHENE OXIDE

Originally published in Scientific Reports as: Benjamin, C. J.; Wright, K. J.; Bolton, S. C.; Hyun, S. H.; Krynski, K.; Grover, M.; Yu, G.; Guo, F.; Kinzer-Ursem, T. L.; Jiang, W.; Thompson, D. H., Selective Capture of Histidine-tagged Proteins from Cell Lysates Using TEM grids Modified with NTA-Graphene Oxide. *Sci Rep* **2016,** *6*, 32500.

3.1 Introduction

Single particle cryo-EM analysis (SPA) is a rapidly growing method for elucidating structure of biological materials at near atomic resolution[97, 98] due to recent advances in instrumentation and computational algorithms[77]. One aspect of the SPA process that is not well optimized, however, is sample preparation. Traditionally, proteins targeted for structural analysis must be overexpressed and subjected to time-consuming purification and concentration steps, sometimes under harsh conditions that disrupt protein-protein interactions of interest. Recently, there have been efforts reported that seek to address these limitations, either by improving grid rigidity to reduce beam-induced motion[99-101] or by effecting on-grid purification with 'affinity grids'[94, 102-104] that employ metal chelating lipids that were originally developed for two-dimensional protein crystallization at the lipid-water interface[105-108]. The latter approach seeks to selectively capture biological target molecules from complex mixtures such as cell lysates as an integral part of the TEM sample preparation process[92, 102].

Although lipid monolayer affinity grids have shown some success in producing samples for cryo-EM reconstruction at 20 Å resolution[94], robust performance of the reported grid coatings may be limited by film instability and non-uniformity under the evaporative casting methods that are often employed. Additionally, these lipid films require a thin polymer layer or a holey carbon substrate layer to provide mechanical support of the deposited film. The electrical conductivity of monolayer graphene is six orders of magnitude higher than amorphous carbon, and although the level of conductivity in graphene decreases with the extent of oxidation, it has been shown to recover much of this conductivity upon reduction with H_2 plasma[104]. Additionally, unlike unsupported lipid monolayers, the elasticity of graphene makes it ideal to resist permanent deformation due to mechanical transfer techniques from the material-water interface. Our interest

in utilizing graphene-based affinity substrates is focused on exploiting the superior mechanical strength and conductivity it offers. By conferring better target specificity to this substrate, affinity graphenic substrates have the potential to offer both improved stability and resistance to non-specific adsorption such that direct capture from cell lysates may be feasible.

We sought to address the limitations of lipid monolayer coated affinity grids by employing a GO derivative that minimizes background signal due to the single atom thickness and improved conductivity as a way to combat sample charging and instability during image capture[109]. Here we demonstrate the utility of affinity grids using Langmuir-Schaefer (L-S) transfer of GO monolayer sheets that have been functionalized with covalently linked N^{α}, N^{α}-dicarboxymethyllysine (GO-NTA). Using these affinity grids, we were able to selectively capture both His_6-T7 bacteriophage and His_6-GroEL. When the prepared grids were further modified with bovine serum albumin (BSA), a common antifouling agent that limits non-specific adsorption of non-targeted cellular debris, we were able to selectively capture these proteins directly from bacterial lysate while avoiding deposition of non-target proteins (Figure 1).

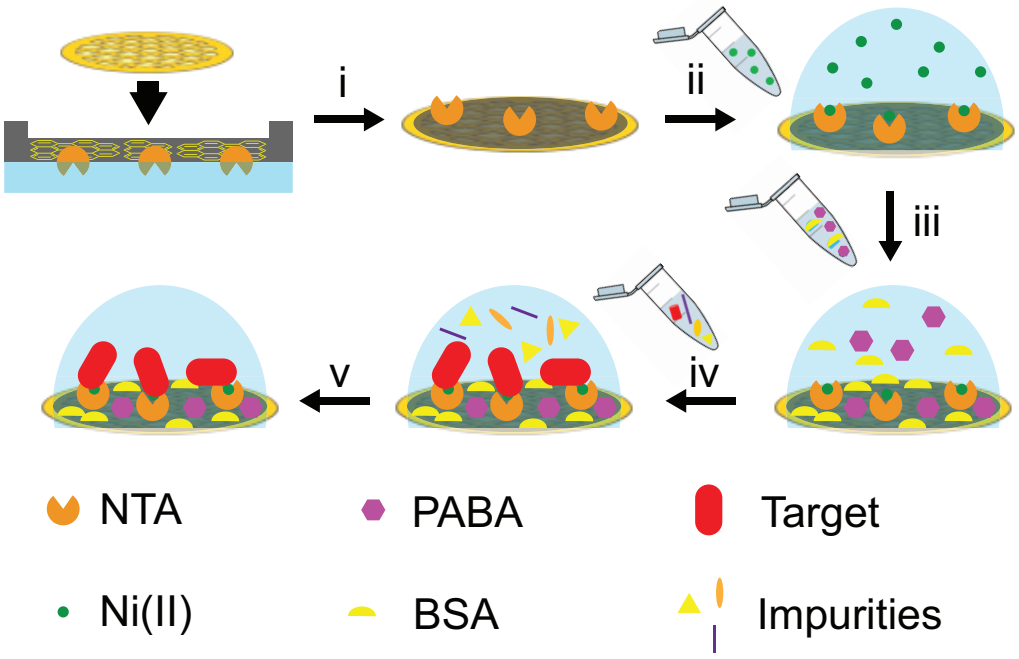

Figure 3.1. Conceptual diagram of sample preparation using a GO-NTA modified TEM grid. (i) GO-NTA monolayer deposition onto TEM grid via L-S transfer; (ii) activation of NTA with Ni^{2+}; (iii) blocking of non-specific reaction and/or adsorption sites with 4-aminobenzoic acid (PABA) and bovine serum albumin (BSA); (iv) incubation of clarified lysate with blocked grid; (v) washing of non-target molecules from grid, followed by cryo-fixation or staining.

3.2 Experimental Methods

3.2.1 Graphene-Oxide-NTA Synthesis.

GO was synthesized as described by Marcano *et al.* [109]. This intermediate (335 mg) was stirred in a mixture of $SOCl_2$ (60 mL) and DMF (1.5 mL) at 70 ˚C for 3 d before evaporating the $SOCl_2$ and DMF and washing the residue with dry DCM (3 x 50 mL). ACN (50 mL) and Et_3N (3 mL) were then added and the mixture stirred for 30 min. Tris(O-*t*-butyl)-N^{α},N^{ω}-dicarboxymethyllysine ester (533 mg) was then added and the mixture stirred at 100 ˚C for 3 d before washing with THF and H_2O (9,000 rpm for 15 min, 3 times for each solvent), before vacuum drying at 60 ˚C for 24 h. TFA (10 mL) in THF (30 mL) was added to the dried *t*-butyl-NTA ester intermediate (180 mg) and stirred at 60 ˚C for 5 h before washing with THF and H_2O (11,000 rpm x 15 min, 3 times for each solvent) [110-111].

3.2.2 GO-NTA Exfoliation.

The GO-NTA sheets were ultrasonically exfoliated at 1 mg/mL by suspension of the powder in 5:1 MeOH:H_2O using probe sonication at 150 watts for five cycles (45 s sonication followed by 45 s of rest in each cycle). The product was centrifuged at 1200 g for 10 min, after which the supernatant of exfoliated GO-NTA sheets was removed from the sediment of aggregated sheets and subjected to another 5 rounds of sonication. A final centrifugation at 1200 g for 10 min was performed prior to removal of the supernatant to yield a GO-NTA solution that was stored for subsequent grid coating experiments.

3.2.3 Langmuir-Trough Setup.

Exfoliated GO-NTA was deposited at the air-water interface of a Kibron μTrough via a syringe pump fitted with a 20 mL syringe. The GO-NTA dispersion was loaded into the syringe and slowly introduced at the air-water interface at a rate of 100 μL/min until the surface pressure reached 15 mN/m. The film was then allowed to relax for 5 min, followed by slow compression of the film to 15 mN/m. IPA was then added to the subphase and the film transferred to either Si wafers, bare 1500 mesh TEM grids, or holey carbon grids by Langmuir-Schaefer (L-S) transfer.

3.2.4 4-Aminobenzoic acid (PABA) Modification of GO-NTA.

GO-NTA (1 mg/mL) was partially deactivated by adding PABA (30 mg) to a 10 mL GO-NTA dispersion. This mixture was probe sonicated at 150 W for 30 sec of continuous sonication, followed by shaking for 24 h on a rotary mixer. The PABA-GO-NTA was then exfoliated and washed as described above for GO-NTA exfoliation.

3.2.5 Fluorescein Modification.

Fluorescein modification of GO-NTA was performed by adding 2 mg of aminofluorescein to an aqueous solution of PABA-GO-NTA (10 mL at 1 mg/mL). This mixture was probe sonicated for 30 s at 150 W of continuous sonication and then placed on a rotary mixer in the dark for another 24 h. The material was then centrifuged to pellet the GO species before re-suspending in water, addition of 5:1 MeOH:H_2O, re-pelleted, and decanted a total of 10 times before exfoliation of the Fluorescein-PABA-GO-NTA (F-PABA-GO-NTA) product as described above for GO-NTA.

3.2.6 Bovine Serum Albumin (BSA) Modification.

Following L-S transfer of GO-NTA or PABA-GO-NTA onto EM grids and overnight drying in a desiccator, the grids were placed on a strip of Teflon before addition of BSA (10 μL of 0.1 mg/mL) and incubation for 5 min, followed by 3 x 20 μL double deionized H_2O washes. The modified grids were then stored in a desiccator until use.

3.2.7 Fluorescence Microscopy Sample Preparation.

F-PABA-GO-NTA was deposited onto 1500 mesh grids in the dark by L-S transfer as described above. After transfer, the grids were allowed to dry in the dark for 1 d before sandwiching them between a glass and cover slip with 5 μL of double deionized H_2O and the sandwich sealed with nail polish. The glass slide was then mounted on a light microscope for epifluorescence imaging.

3.2.8 GO Concentration Measurements.

The concentrations of the GO-NTA dispersions were measured at different steps of the synthesis by monitoring the UV-vis spectra of the products. The extinction coefficient data used for one batch of GO-NTA is shown (Figure S1A). Since each batch of GO-NTA has minor differences in concentration, each preparation was evaluated for its own experimentally determined extinction coefficient for subsequent concentration measurements. Standard solutions used to determine the extinction coefficients were prepared by dispersing a weighed amount of dry GO-NTA into known volumes of 5:1 MeOH:H_2O and measuring the absorbance at 280 nm across a series of dilutions with 5:1 MeOH:H_2O. The extinction coefficient was derived from the slope of these concentration-dependent absorption plots.

3.2.9 GO-NTA Grid Treatment with Purified His_6-T7 Bacteriophage.

Purified C-terminal gp10 His_6-T7 bacteriophage was initially prepared at a concentration of 10^{12} particles/mL, with dilution to 10^{10} particles/mL in HEPES buffer (pH = 7.4) before application to the affinity grid surface. GO-NTA modified grids were placed on a Teflon strip, 1 mM $NiSO_4$ (10 μL) added and the grids incubated for 5 min before washing with double deionized H_2O (2 x 20 μL) and HEPES buffer (1 x 20 μL). Purified phage (3.5 μL) was then applied to the surface and incubated for 2 min before washing with HEPES (2 x 20 μL), double deionized H_2O (1 x 20 μL), and staining with 2% uranyl acetate (5 μL).

3.2.10 GO-NTA Grid Treatment with His_6-T7 Bacteriophage Lysate.

BL21 bacterial cells in 1 mL of LB media were grown to an OD of 0.8 before adding 1.0 μL of His_6-T7 bacteriophage (1 x 10^{12} particles/mL) to the media and shaking the culture for 1 h. After bench top centrifugation of the cells, the supernatant was withdrawn for use in His_6-T7 bacteriophage particle capture studies. The grids were Ni^{2+}-activated as described above, except that His_6-T7 lysate (5 μL) was applied to the surface before incubation for 2 min. The grids were then washed with HEPES (2 x 20 μL), double deionized H_2O (1 x 20 μL), and then stained with 2% uranyl acetate (5 μL).

3.2.11 GO-NTA Grid Treatment with His_6-GroEL Lysate.

The ASKA Library was used to express N-terminal His_6-GroEL. Cells containing N-His_6-GroEL gene overexpression vector were grown to OD = 0.6 (in 100 mL of LB broth using a 37 ˚C shaker/incubator) and induced with a final concentration of 1.0 mM IPTG, before allowing the cells to grow for an additional 4 h. After centrifugation and removal of the supernatant, the cell pellet was re-suspended in lysis buffer (20 mM HEPES, 100 mM NaCl, pH = 7.4, 100 µg aprotinin, 174 µg phenylmethanesulfonyl fluoride (PMSF), and 500 µg of lysozyme) and allowed to sit for 20 min. Further disruption of the cell membranes was effected by 110 W probe sonication (35 pulses at 1 second/pulse), followed by centrifugation at 11,000 g for 10 min. The supernatant containing His_6-GroEL was diluted 10-fold and assayed for affinity binding using the Ni^{2+}-activation procedure described above, except that N-His_6-GroEL lysate (5 µL) was applied to the surface and incubated for 2 min. The grids were then washed and stained with 2% uranyl acetate as described above.

3.2.12 Affinity Capture of His_6-GroEL from E. coli Lysates onto BSA-PABA-GO-NTA Grids for Cryo-EM Imaging.

Samples were prepared as described above for negative stain TEM imaging, except that BSA-PABA-GO-NTA modified grids were exposed to His_6-GroEL lysate, after which the excess solution was removed by blotting twice for 6 s per blot using an offset setting of -1 at 80% humidity using a Vitrobot device (FEI Company). The grids were then plunged into liquid ethane for cryofixation and imaged at 300 kV on an FEI Titan Krios equipped with a Gatan K2 Summit direct electron detection camera using low-dose techniques. Integrated microscope automation software Leginon[112] was used to acquire a large set of micrographs at 11,000x magnification with an exposure time of 7.6 sec.

3.2.13 Single Particle Analysis of His_6- GroEL.

Direct electron detector movie frames were processed in Appion[78] to produce a set of averaged, motion-compensated micrographs to be used in subsequent steps. The micrographs had a 1.32 $Å^2$/pixel resolution across a 4096 Å x 4096 Å array. EMAN 2.1 software[81] was used for reconstruction of 5363 particles that were manually picked from 217 micrographs using a box

size of 256. Automatic contrast transfer function (CTF) estimation and structure factor were determined from the incoherent sum of particles using e2ctf and phase-flipped to generate high-pass CTF-corrected particle stacks. Defocus was estimated to range between 0.4 μm – 4 μm, but 55% of the particles were defocused between 2 μm – 3 μm which resulted in a somewhat jagged CTF slope. Particles were binned 2X for class averaging and 12 classes were chosen to create an initial model with imposed D7 symmetry. The classes contained a mix of top and side views. In the refinement steps, the input set of particles was divided into even/odd halves, each containing 2682 particles. Two independent refinements were generated, producing a gold standard of 8.1 Å (using 0.143 criteria) after 12 iterations over two refinements with an angular sampling of 1.76 degrees. Additionally, we performed Fourier shell correlation against an existing high-resolution cryo-EM map, EMD-5001[113]. The maps were rotated and translated using Chimera[114] to fit the volumes together. The correlation of our model against EMD-5001 (4.2 Å) gave an approximate resolution of 9 Å.

3.3 Results and Discussion

3.3.1 Synthesis of GO Sheets Functionalized with NTA.

GO was produced from graphene using Hummer's method[109]. Activation of the GO carboxylic acid groups with $SOCl_2$ prior to reaction with the tris-*t*-butyl ester of lysine NTA gave GO-NTA-(O-*t*-Bu)$_3$. TFA deprotection of this intermediate gave GO-NTA (Figure 2A). Fourier transfer infrared spectroscopy was used to monitor these reactions as shown in Figure 2B[115]. The spectra of GO displayed a broad absorption at 3236 cm^{-1} (O-H stretch) and a sharper absorption at 1648 cm^{-1} (C=O stretch) [109]. The NTA-GO tris-*t*-butyl ester displayed an additional absorption at 2933 cm^{-1} (C-H stretch) due to the incorporation of the lysine and *t*-butyl moieties. Following treatment of NTA-GO tris-*t*-butyl ester with TFA, the presence of the aliphatic C-H stretching was greatly reduced, indicating successful deprotection of the NTA chelator substituents[116].

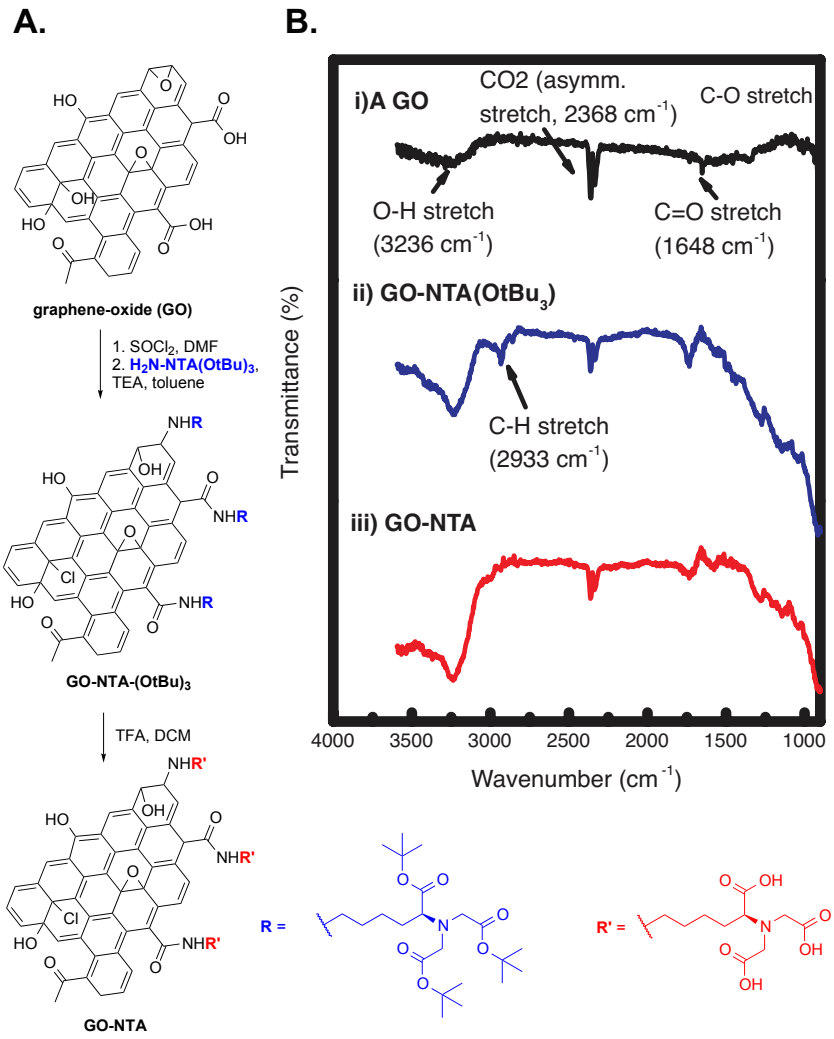

Figure 3.2. (A) Reaction sequence for preparation of GO-NTA from GO. (B) FTIR spectra of (i) GO, (ii) GO-NTA(O-*t*-Bu)$_3$, and (iii) GO-NTA.

Previous work has shown that the typical GO sheet absorption band at ~240 nm is shifted to ~270 nm when the GO sheets are dispersed in aqueous solution. The origin of this hypsochromic shift is due to n-π* electronic transitions arising from the C=O bonds introduced by oxidation[117]. GO-NTA samples prepared in this manner exhibited a major absorption peak at ~280 nm (Figure S1), in good agreement with these reports.

3.3.2 GO-NTA Monolayer Formation.

Most reports of Langmuir dispersions of GO at the air-water interface focus on surfactant-assisted dispersion methods to stabilize GO sheets dispersed in water[118]. Treatment of

GO with surfactants in these cases; however, biases the interfacial activity towards water-surfactant activity rather than GO-NTA activity due to their high relative abundance. The planar structure and functional group distribution on GO-NTA confers edge amphiphilicity due to the distribution of hydrophilic carboxyl, ketone, aldehyde, amide, and alcohol groups around the periphery of the hydrophobic aryl GO-NTA core (Figure 2A) [119]. Since GO-NTA becomes increasingly hydrophobic as displacement toward the core from the GO-NTA edge increases, larger sheets will tend to be more hydrophobic and migrate to the air-water interface, whereas smaller more hydrophilic GO-NTA sheets are displaced into the aqueous subphase by the larger GO-NTA sheets[120].

Previously, it was thought that the use of surface-active agents was needed to disperse GO sheets. More recent work; however, has shown that GO layers form at the air-water interface in the absence of surfactant molecules[121]. Brewster angle microscopy studies have shown that the interfacial refractive index of GO solutions change after a few hours of stirring pure GO dispersions in water[122]. This suggests a time-dependent mechanism for GO absorption at the air-water interface, with slower interfacial adsorption rates attributable to slower diffusion rates of large graphene sheets relative to typical surfactant molecules used for studies of the air-water interfaces. To increase the amount of surface-active graphene sheets present at the air-water interface while circumventing hours of stirring, studies using rising gas bubbles of CO_2 and N_2 as a way of transporting these sheets to the surface have proven successful[120]. These studies show that GO can migrate to the air-water interface, while other work suggests that the surface activity of GO sheets in water can be increased using volatile, polar protic solvents to enable their manipulation using Langmuir compression[121].

Compression of the GO-NTA material at the interface gave a characteristic surface pressure-area isotherm (Figure 3A), suggesting a progression from isolated GO-NTA sheets to close edge-to-edge packing of GO-NTA sheets, followed by folding, wrinkling, and sliding of the nearest neighbor GO-NTA sheets atop one another upon further compression[123], in a manner analogous to pressure-induced collapse of Langmuir phospholipid monolayer films[121]. Repulsive electrostatic interactions and attractive Van der Waals forces compete as GO-NTA sheets come into close contact. Previous work with GO monolayers has suggested that over-compression of GO causes irreversible coagulation above ~15 mN/m[23] due to the increasing participation of attractive van der Waals interactions once the repulsive electrostatic interactions between sheet

edges has been overcome by lateral compression. Transfer of these films onto silicon substrates at multiple surface pressures enabled the transfer of single layer GO sheets at surface pressures above 15 mN/m.

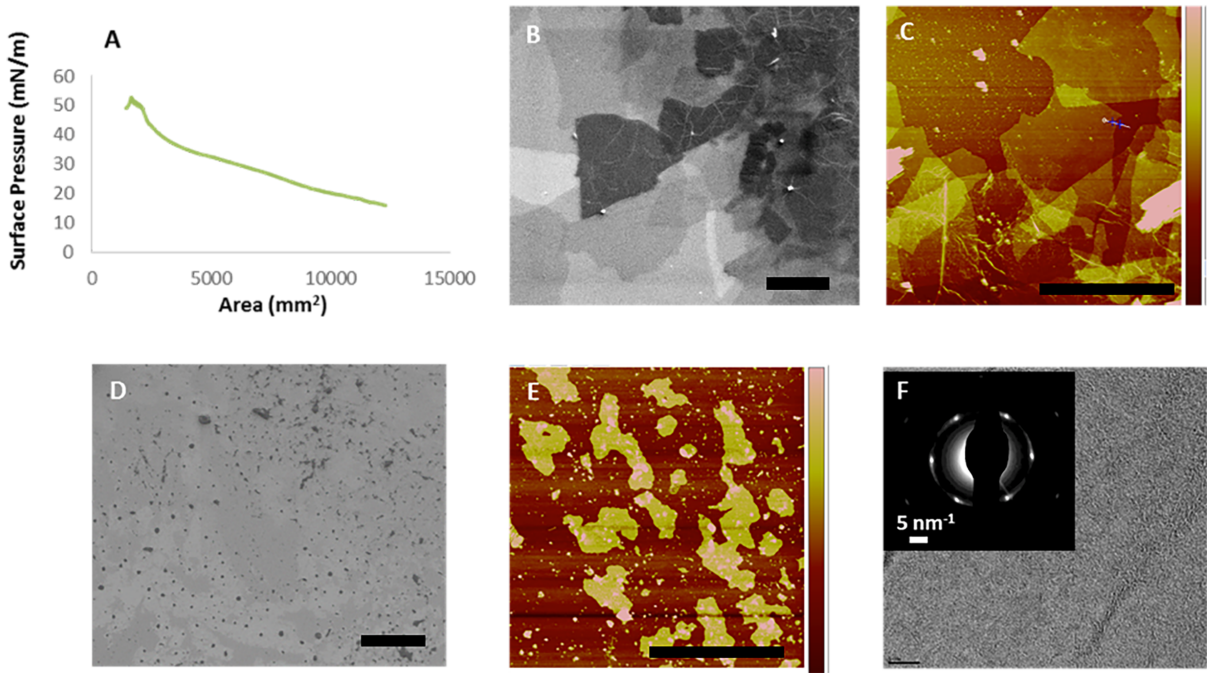

Figure 3.3. (A) Pressure-area isotherm for GO-NTA sheets at the air-water interface, dispersed at 67 ng/mL in water at 20 °C. GO-NTA sheets compressed at a rate of 500 mm^2/min. (B) SEM images taken 1.0 keV, with 5 µm scale bar and (C) AFM images of GO-NTA after LS-transfer onto Si wafers from a subphase of pure H_2O (5 µm scale bar). (D) SEM images taken at 0.5 keV (5 µm scale bar) and (E) AFM of GO-NTA after LS-transfer onto Si wafers from a subphase of IPA/H_2O (5 µm scale bar). (F) TEM image of GO-NTA monolayers after L-S transfer from a subphase of IPA/H_2O onto TEM grids; Inset: Selected area electron diffraction analysis of GO-NTA monolayer.

3.3.3 Characterization of GO-NTA Monolayers.

Epifluorescence microscopy, AFM, and SEM was employed to determine the thickness and lateral distribution of GO-NTA sheets deposited onto solid substrates by L-S transfer from the air-water interface[124]. In particular, epifluorescence microscopy of F-PABA-GO-NTA monolayers proved useful because opacity of the graphene-based sheet is directly related to its thickness as revealed by analysis of monolayer-coated grid and negative control bare Cu TEM grid samples that showed significantly greater fluorescence intensity for grids coated with F-PABA-GO-NTA (Figure S2).

We then evaluated drop casting and L-S transfer deposition methods for the production of the thinnest films possible, while yielding films with the highest density of NTA capture ligands. Drop casting[124-125], followed by slow evaporation of solvent, resulted in a fluorescence signal that completely spanned the holes of Formvar-coated 400 mesh Cu grids (data not shown). Slow solvent evaporation enables GO sheets to settle on top of one another to form a multi-layered film covering the TEM grid holes. Although successful, our findings suggest that drop casting typically yields sheets that are too thick and heterogeneous for protein structure elucidation applications by cryoEM. L-S transfer in the presence of 2-propanol (IPA) proved successful for depositions onto 1500 mesh grids, both with and without Formvar coating; however, L-S transfers with pure water resulted in thicker heterogeneous coatings over a limited area of the holes. L-S transfer onto Si wafers under identical conditions confirmed the presence of multilayered films (Figure 3B & D). We were not able to fabricate functional coatings with 400 mesh grids using L-S transfer, a finding we attribute to the mismatch between the average GO-NTA sheet size of ~16 μm x 16 μm and the 37 μm x 37 μm grid holes of these grids. It is worth noting that the GO-NTA sheet size can vary as a function of oxidation reaction duration and sonication time employed during GO synthesis[126].

To gain further insight into the structure of these GO-NTA films, SEM and AFM analyses were performed after compression to 15 mN/m and L-S transfer of GO-NTA monolayer sheets onto Si wafers. To prepare Si wafers for L-S transfer, ~2.25 cm^2 wafers were cut and glued (bottom side) onto a transfer tube. The surface pressure was maintained until the Si wafer contacted the monolayer; the film was then recompressed to 15 mN/m after the L-S transfer step. The area difference before and after L-S transfer indicated transfer efficiencies of 75 – 85%. Image analysis of the coated Si wafers revealed the presence of GO-NTA monolayer sheets transferred from IPA-containing subphases with ~1.3 nm thicknesses that were relatively uniform (Figure 3D & E), in good agreement with previously reported values for single layer GO[111]. In the absence of IPA; however, data from SEM and AFM experiments revealed GO-NTA films comprised of overlapping sheets and undesirable layer thickness variations (Figure 3B & C).

Selected area electron diffraction analysis of GO-NTA L-S films, deposited onto bare 2000 mesh grids from the air-IPA/H_2O interface, revealed a hexagonal diffraction pattern,

indicative of a single layer of graphenic material (Figures 3F). The measured intensity of the inner and outer peaks confirms the presence of a single GO-NTA layer (Figure S3) [125].

3.3.4 Affinity Capture of His_6-T7 Bacteriophage from *E. coli* Lysate Using GO-NTA Monolayer Purification and PABA + BSA as Antifouling Agents.

The capacity of GO-NTA coated grids to capture His_6-T7 bacteriophage (His_6-T7) by affinity interaction was examined first by negative-stain TEM. After a 2 min exposure of purified His_6-T7 on GO-NTA modified 1500 mesh grids, dense clusters of phage particles were found on the GO-NTA surface in the absence of Ni^{2+} (Figure 4A). Paradoxically, we observed fewer phage particles after charging the GO-NTA grids with Ni^{2+} (Figure 4B). We attribute these findings to non-specific and random covalent coupling of lysine residues with epoxide and aldehyde residues on the GO sheets that are inactivated upon exposure to the metal ion[127]. To obviate this problem, we chemically deactivated these functional groups by treatment of GO-NTA with 4-aminobenzoic acid (PABA) after L-S transfer. The resulting PABA-GO-NTA grids showed a reduction in, but incomplete abrogation of, non-specific His_6-T7 binding under the same incubation conditions (Figure 4C). When activated with Ni^{2+}, PABA-GO-NTA grids revealed a higher density of phage particles due to engagement of the NTA:Ni^{2+}:His_6 affinity interaction (Figure 4D). To further enhance the anti-fouling properties of this material, we incubated the PABA-GO-NTA grids with BSA immediately before the affinity capture step. Under these conditions, BSA appears to complete the blockade of non-specific viral particle adsorption (Figure 4E), suggesting that BSA inhibits non-specific binding more effectively than PABA modification. After Ni^{2+} activation of the BSA-blocked PABA-GO-NTA surfaces, we observed a recovery in His_6-T7 binding to the grids (Figure 4F). To further demonstrate the Ni^{2+} dependence of this interaction, we treated the grid with 500 mM imidazole, leading to the elution of His_6-T7 from the grid (data not shown). Taken together, these findings demonstrate the importance of deactivating highly reactive chemical functionalities on the surface of GO prior to use in affinity capture experiments.

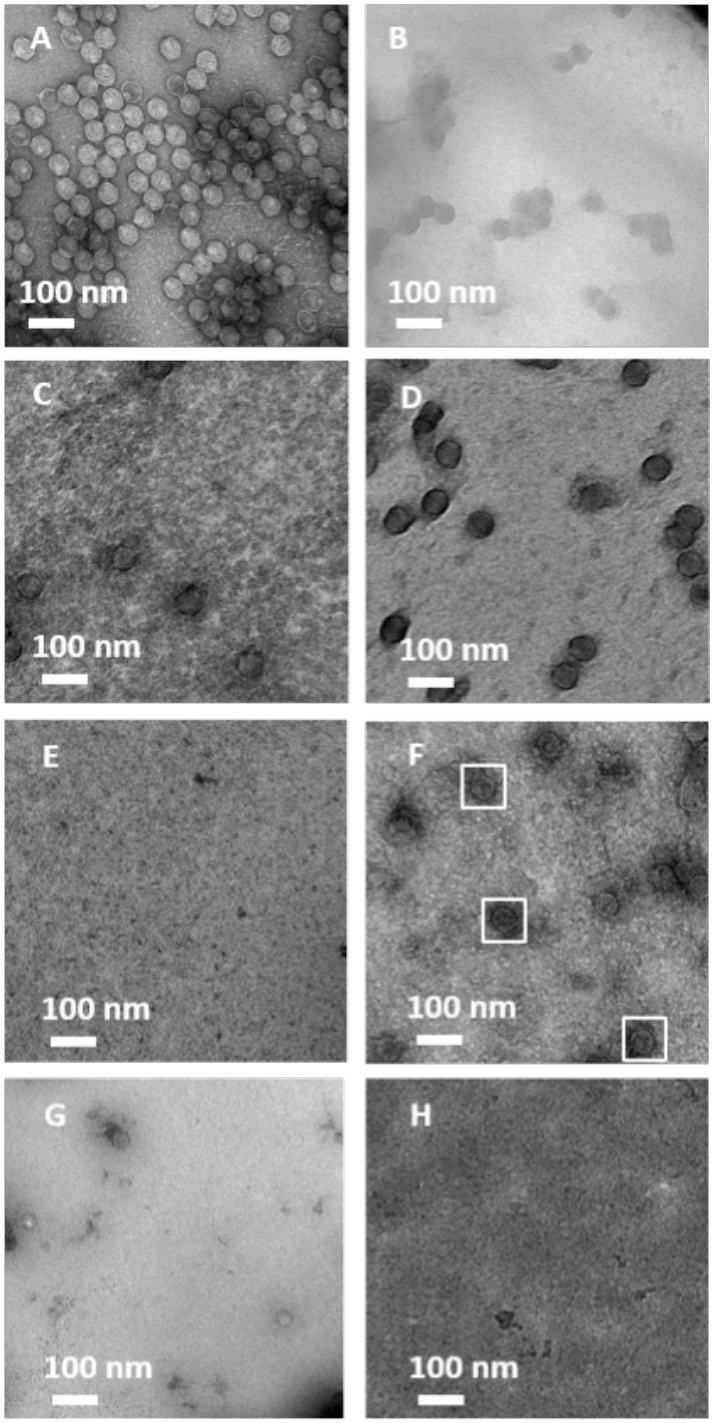

Figure 3.4. Micrographs of negatively stained his_6-T7 bacteriophage using various TEM grid coatings: (A-B) GO-NTA; (C-D) PABA-GO-NTA; and (E-H) BSA-PABA-GO-NTA. Negative controls (A,C,E) demonstrate no capture of purified phage when Ni^{2+} is absent, whereas coatings treated with Ni^{2+} (B,D,F) show capture of purified phage. Affinity capture of phage from lysate (G) can be reversed by incubation of (G) with 500 mM imidazole (H) that removes the Ni^{2+} from the coating and abrogates the affinity interaction between the phage and the grid surface.

Next, we sought to capture His_6-T7 directly from clarified *E. coli* lysate. The engineered His-tag does not interfere with His_6-T7 infectivity, thereby enabling the infection of BL21 cells and viral replication *in vitro*. A negative control experiment demonstrated that Ni^{2+}-free BSA-PABA-GO-NTA grids resulted in little or no capture of phage and minimal background adsorption from non-targeted cellular material (Figure S4); however, Ni^{2+} activation prompted selective His_6-mediated binding of bacteriophage to the grid surface (Figure 4G). As an additional control, the grid was washed with 500 mM imidazole after Ni^{2+}, but prior to incubation with lysate, to demonstrate that imidazole stripping of the metal ion results in the abrogation of His_6-T7 binding (Figure 4H). These results indicate that BSA-PABA-GO-NTA coated grids are able to effectively purify His_6-T7 directly from clarified lysate on the grid using the reversible NTA:Ni^{2+}:His_6 affinity interaction.

3.3.5 Affinity Capture of GroEL From *E. coli* Lysate Using BSA-PABA-GO-NTA Monolayer Purification.

The performance of antifouling BSA-PABA-GO-NTA coatings for high-resolution single particle reconstruction analysis was then evaluated by performing on-grid affinity capture of His_6-GroEL from *E. coli* lysates. As observed for His_6-T7 capture, specific binding of His_6-GroEL occurred only with Ni^{2+}-activated (Figure 5B), but not Ni^{2+}-free (Figure 5A) or 500 mM imidazole treated grids (Figure 5C). Next, we obtained cryo-EM images of His_6-GroEL deposited onto BSA-PABA-GO-NTA coated grids (Figure 5D). Initial attempts at His_6-GroEL capture and cryofixation on 1500 mesh grids coated with BSA-PABA-GO-NTA generated unacceptably thick sample vitrification; however, high quality samples of His_6-GroEL captured from lysate were afforded by BSA-PABA-GO-NTA films deposited by L-S transfer onto lacey carbon-supported 400 mesh copper grids.

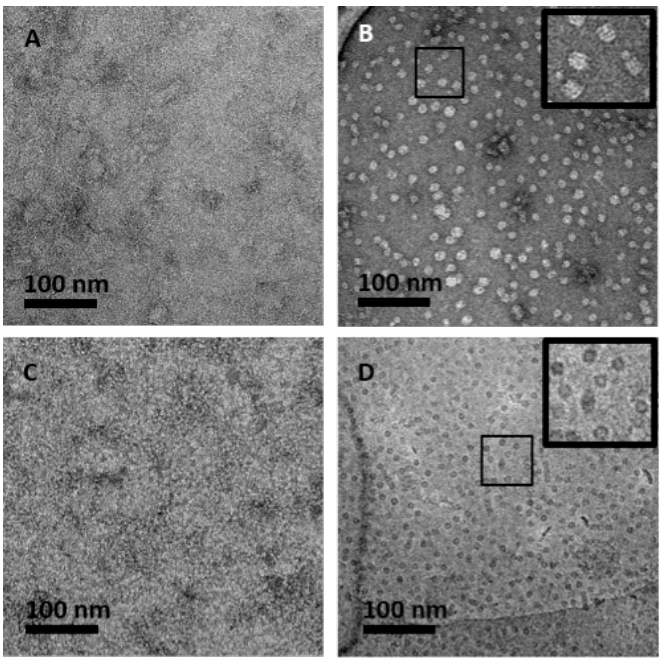

Figure 3.5. Micrographs of his_6-GroEL lysate affinity capture using BSA-PABA-GO-NTA TEM grid coating. Micrographs (A-C) are negatively stained. (A) Negative control showing no capture of his_6-GroEL when Ni^{2+} is absent. (B) Affinity coating activated with Ni^{2+} displays specific capture of his_6-GroEL from lysate. Treatment of the grid in (B) with 500 mM imidazole (C) leads to Ni^{2+} stripping from the coating and abrogation of his_6-GroEL capture. (D) Representative cryo-EM image of affinity captured his_6-GroEL from lysate.

3.3.6 Single Particle Analysis of His_6-GroEL.

EMAN 2.1[81] was used for single particle analysis of His_6-GroEL deposited onto BSA-PABA-GO-NTA coated grids since this protein target is often used for gauging workflow performance and data processing robustness[113, 128-129]. The reconstruction effort followed the usual steps from within the application, except that the particles were manually picked. Background signal contributions by the BSA blocking layer may also have contributed to the difficulties encountered during attempts at automated particle picking. Nonetheless, 5363 particles were hand-picked from 217 micrographs and the particles rapidly converged into coherent classes displaying high contrast (Figure 6A).

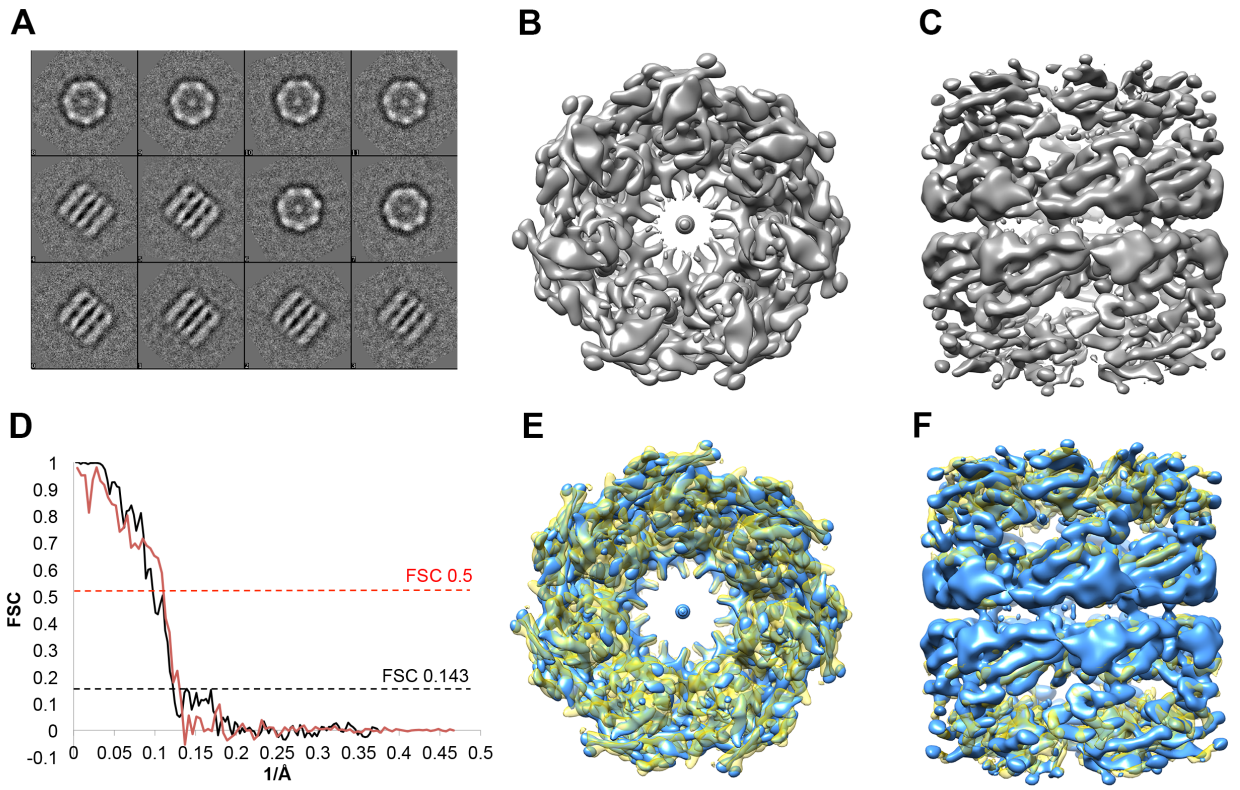

Figure 3.6. (A) Class averages of his_6-GroEL images captured from BSA-PABA-GO-NTA coated grids that were used to build the initial model; (B) Top and (C) side views of refined his_6-GroEL EM map at 8.1 Å resolution (gold standard, 0.143 criteria); (D) Fourier Shell Correlations: gold standard using conservative masking (black), and cross-validation between published GroEL map EMD-5001 and our map (red); (E) Top and (F) side views of overlay with our his_6-GroEL EM map (blue) and EMD-5001 (yellow) [113]

Of 50 total class averages, 12 were chosen to produce an initial model with imposed D7 symmetry (Figure 6A). After 12 refinement iterations with an angular sampling of 1.76 degrees, we were able to produce a gold standard (0.143 criteria) density map having 8.1 Å resolution using conservative masking (Figures 6B-D). There were visible nodes in the FSC curve at regular intervals that resulted from an uneven distribution of micrograph defocuses.

To verify the accuracy of our model, we performed a comparison with published 4.2 Å resolution cryo-EM map EMD-5001[113] that was also produced by EMAN using D7 symmetry. Chimera[114] was used to fit the volumes before calculating the FSC, yielding a 9 Å resolution using 0.5 criteria (Figure 6D-F).

A substantial difference between our map and the published structure was observed, wherein additional electron density within the inner pore of the protein was found in the case of our His_6-GroEL map. We attribute this finding to the extended amino acid sequences at the N- and C-termini (i.e., MRGSHHHHHHTDPALRA and GLCGR, respectively) of our His_6-GroEL construct derived from the ASKA Library.

Wild type N- and C-termini of the protomers are located at the surface of the inner pore lining the assembled tetradecameric complex. Thus, the 14 engineered subunits comprising our His_6-GroEL complex yield an additional 308 residues that occupy the pore, of which 84 are histidines. Given the large number of potential metal chelation regioisomers and topoisomers, as well as the high potential for conformational flexibility in the N- and C-terminal sequences, we believe that this density is unlikely to adopt a defined structure and instead appears as a filled "droplet" within each ring. Also, there is a noticeable decrease in density in the flexible apical region that suggests less structural coherency. We infer from these findings that the additional pore residues, along with NTA chelation, may create dynamic distortions to the structure of GroEL that could vary for each particle, reducing coherency and map density at the apical ends. Further experiments that vary the length and number of his-tag linkers per particle may allow for a better model convergence with improved resolution, and potentially improved resemblance to wild type GroEL.

3.4 Conclusions

Our findings show that a new functionalized GO-NTA monolayer sheet can be used as a coating to facilitate on-grid affinity purification from clarified cell lysates for negative stain TEM and cryo-EM single particle reconstruction analysis. GO sheets were successfully functionalized with lysine-NTA affinity ligands and compressed monolayer films at the air-water interface were prepared by employing an IPA/H_2O mixture to lower surface tension before L-S transfer onto EM grids. SEM, AFM, fluorescence spectroscopy, and TEM analysis of these films suggests that single monolayer sheets of GO-NTA can be transferred onto Si wafers, bare copper grids, and holey carbon grids using this method. Since GO films are thinner than amorphous carbon substrates and offer better electron dissipation than lipid-based affinity grids, we believe these two benefits will yield improved contrast for cryo-EM image acquisition of biological molecules.

Two blocking techniques, PABA coupling and BSA adsorption, were needed to deactivate the reactive GO surface towards non-specific adsorption of occult impurities present in complex samples such as cell lysates. Our data shows that further investigations into blocking agents that minimize background noise and improve cryofixation reliability are needed. Nonetheless, this grid coating approach showed good specificity for capture of His-tagged T7 bacteriophage and GroEL from highly complex cell lysates, while limiting background adsorption of non-targeted cellular material.

The utility of these grids for on-grid purification from cell lysates and single particle reconstruction was demonstrated using His_6-GroEL. Capture of this target onto the surface of GO-NTA affinity grids from clarified cell lysates was then used as the key step to enable selection of 5363 particles for reconstruction analysis, yielding a map with a gold standard resolution of 8.1 Å. The presence of additional His-tag and linker amino acids in our engineered GroEL was distinctly visible in our density map, but our final map could still be fit to a published high-resolution EM map to 9 Å resolution using 0.5 criteria. We conclude based on these findings that affinity capture-based graphenic materials offer great potential for simplified and accelerated cryo-EM sample preparation for high-resolution structure elucidation. These coatings possess many advantages over NTA-lipid-modified grids[94, 103] or other grid coatings that lack protection from non-specific binding[99-101], thereby offering substantial improvements in sample preparation time and reduced sample volumes needed to acquire high resolution structural information of a given protein target and, potentially, its interaction partners.

CHAPTER 4. OPTIMAL METHOD FOR THE EXPRESSION AND PURIFICATION OF HUMAN CAMKII ALPHA

This work has been submitted for publication to *Biochemistry*.

4.1 Introduction

The CaMKII protein family is comprised of four highly similar genes identified as α, β, γ, and δ[65]. Together these genes and their variants constitute approximately 40 different isoforms. The α and β isoforms are predominantly found in neurons and comprise 1–2% of total protein in the hippocampus[32]. CaMKII works in concert with neuronal signaling pathways to strengthen synapses and enhance plasticity, long-term potentiation, and cell growth. There are many excellent reviews on CaMKII function[24-27, 30, 130]. The holoenzyme in neurons exists as a dynamic oligomer with a mix of α and β isoforms and is assembled into a 12 - 14 subunit complex[53, 59, 131]. To better decode the complex functionality of the enzyme as an oligomer, however, recombinant enzymes are produced solely with the α isoform. The flexibility of its tethered catalytic domains enables the autophosphorylation of neighboring subunits as well as downstream proteins. It is this flexibility that has generated interest in understanding its structure and function. To better enable these studies, a high yield of homogenous, mono-disperse and viable protein is needed. Given the short viability time and aggregation-prone behavior of CaMKII, the purification conditions and handling time must be optimized to ensure the recovery of the intact, autoinhibited holoenzyme in high yield[96, 132].

There have been two main methodologies for generating pure recombinant CaMKII protein from cell culture reported in the literature: wild type baculovirus insect expression and his-tagged bacterial expression. Table 4.1and Table 4.2 list the different purification techniques that have been reported, and yield information (when given) is listed in Table 4.3.

Table 4.1. BEVS Expression Purification Steps

Ref	Step 1	Step 2	Step 3	Step 4	Step 5
Brickey[133]	Ammonium Sulfate	CaM-Sepharose	–	–	–
Putkey[134]	Ammonium Sulfate	CaM-Sepharose	Ammonium Sulfate	sucrose	Phosphocellulose
Kolb[135]	CaM-Sepharose	Mono S	sucrose	SEC	–
Singla[136]	Phosphocellulose	CaM-Sepharose			
Torok[137]	CaM-Sepharose	Mono Q	–	–	–
Rosenberg[42]	HiTrap SP	HiTrap Q	SEC	–	–

Table 4.2. E.Coli Expression Purification Steps

Ref	Step 1	Step 2	Step 3	Step 4	Step 5
Chao[67]	IMAC	Mono Q	SEC	–	–
Rellos[44]	IMAC	HiTrap Q	SEC		

Table 4.3. Reported Yields after Purification

Ref	Expression	Mutations	Yield (mg/L)
Brickey[133]	BEVS	WT	8 – 20
Torok[137]	BEVS	WT	12.5
Rosenberg[42]	BEVS	D135N	0.005 – 0.01
Chao[67]	E. coli	C-terminal 6xHis	0.0025

The Soderling lab first described the expression of recombinant wild-type rat-isoform CaMKIIα using a baculovirus/Sf9 expression system. They reported cell homogenization to produce a CaMKII lysate in the presence of glycine betaine, a zwitterionic osmolyte that aids in protein stabilization and the solublization[133, 138]. They claimed that the use of betaine prevented CaMKII from forming aggregates that would precipitate from solution during centrifugation. Additionally, betaine can be used at high concentrations with negligible effect on the operating pressure of chromatography columns. One of the main observations was that the use of betaine in the lysis buffer allowed greater recovery of CaMKII due to the added solubility. Using both ammonium sulfate and calmodulin-Sepharose purification steps, a final yield of 8 – 20 mg of purified CaMKII per liter of Sf9 cell culture was obtained, based on an expression density of $3x10^6$ cells/mL, assuming all cells were multiply infected (MOI of 10) and viable. However, Török *et al.* later reported a method omitting betaine, avoiding ammonium sulfate, and adding an ion exchange step.[137] Since betaine was not part of the protocol, the high yield may be due to the presence of 10% fetal bovine serum (FBS) added to the Sf9 growth medium, that has been

shown to limit the non-specific binding of virus particles to cells and subsequently increases infection multiplicity.[139]

The technique of Brickey *et al.* was adopted by the Waxham lab in a series of papers using similar expression conditions and lysis buffer, but used different purification schemes: from multiple rounds of ammonium sulfate, CaM-Sepharose, sucrose, then phosphocellulose[57, 65, 134], to CaM-Sepharose, ion-exchange, and sucrose[135]. These methods were eventually condensed to phosphocellulose followed by CaM-Sepharose[136, 140]. In the Kuriyan lab, Rosenberg *et al.* used similar expression conditions as Török *et al.* (without mention of FBS supplementation) and modified the lysis buffer to replace betaine with 10% glycerol. Purification occurred in four steps: cationic exchange, buffer exchange, anionic exchange, and finally gel filtration. This process reduced the yield approximately 1000-fold to 10 μg kinase per liter of cells.[42] Later, Chao *et al.* demonstrated the use of a bacterial system to express CaMKIIα.[67] To limit the hyper-phosphorylation of the kinase during expression, the protein was co-expressed with λ-phosphatase, as this happens for many kinases when expressed in bacteria.[141] The CaMKII gene also included a C-terminal 6xHis tag to replace the CaM-Sepharose affinity step. The three-step purification process included IMAC, followed by an anionic exchange and gel-filtration sequence to produce 2.5 μg of purified CaMKII per liter of cells. In spite of the low yields afforded by this method, this technique would find continued use in later publications.[53, 59, 142]

Meanwhile, protein expression studies of baculovirus insect expression systems have been ongoing since Brickey *et al.* first reported CaMKII expression 20 years ago.[143-144] Improved insect expression tools and declining published yields motivated us to revisit the expression and purification of purified CaMKIIα. Here we document an optimized method to minimize handling time while maximizing the yield of this complex holoenzyme.

4.2 Materials and Methods

4.2.1 Baculovirus Insect Expression of CaMKII.

A pFastBac vector (GenScript) incorporating the wild-type human CaMKIIα isoform 1 gene at cloning site BamHI-Xhol (1 ng) was transformed into 100 μL DH10Bac cells by incubation on ice for 30 min, followed by heat shock at 42 °C for 45 sec. Transposition of CaMKII into the bacmid proceeded by adding SOC medium (to 1 mL), followed by incubation at

37 °C on an orbital shaker at 225 rpm for 4 h. TKG (Tetracycline, Kanamycin, and Gentamicin) plates were streaked with 100 µL of culture before incubation at 37 °C for 48 h. A successful colony (white) was picked and transferred to a fresh TKG plate using the quadrant streak method and incubated at 37 °C for 16 h. A single white colony from the fourth quadrant was picked for bacmid prep and inoculated into 4 mL LB medium containing TKG and incubated at 37 °C with shaking at 225 rpm for 16 h. The cells were pelleted and the baculovirus DNA extracted using a Qiagen mini-prep kit following the manufacturer's standard protocol. DNA was stored at 4 °C until use. ESF 921 growth medium (150 µL, Expression Systems) without antibiotics was mixed with 9 µL transfection reactant in a 24 well block before the addition of 10 µL baculovirus DNA and incubation at 20 °C for 30 min. Next, 850 µL of Sf9 cells ($2x10^6$ cells/mL) were added to the well, sealed with a breathable membrane, and incubated for 5 h at 27 °C with 120 rpm shaking. Media (3 mL) containing 10% heat-inactivated FBS was added before incubation at 27 °C with 120 rpm shaking for 1 wk. P0 viral stock was reserved from the supernatant of pellet centrifugation. Further viral amplifications were performed using adherent Sf9 cells in a T-75 flask containing ESF 921 growth medium plus 5% heat-inactivated FBS at 27 °C. After cells reached 50% confluence, 30 µL of viral stock was added and allowed to incubate 4 – 5 d. The amplified virus preparation was harvested from the media by centrifugation at 300 x g for 10 min, then passed through a sterile 0.22 µm filter. Viral amplification was iterated four times, creating P1, P2, P3, and P4 preparations. Lastly, protein expression was accomplished by incubating 2 mL of P4 stock (1:100 v/v) in a 1 L spinner flask (Corning) containing 200 mL of Tni cells ($1x10^6$ cells/mL) in ESF 921 growth medium at 27 °C with 140 rpm shaking. After 24 h, the culture was supplemented with 10 mL (5%) Boost Production Additive (Expression Systems) and the culture was allowed to incubate with shaking for an additional 24 h. Cells were pelleted at 300 x g for 10 min, washed once with buffer (50 mM HEPES, pH 7.5, 200 mM NaCl, 1 mM EGTA and 1 mM EDTA) and pelleted again, then used immediately for purification or flash-frozen in LN_2 and stored at -80 °C.

4.2.2 Bacterial Expression of CaMKII.

A pD444-SR cDNA vector (ATUM) containing a T5 promoter with wild-type human CaMKIIα isoform 1 and λ-phosphatase gene inserts was transformed into 100 µL BL21-CodonPlus(DE3) cells (Agilent) by incubation on ice for 30 min, followed by heat shock at

42 °C for 10 sec. SOC media (950 µL) at room temperature was then added to the cells and incubated at 37 °C for 1 h with shaking at 1250 rpm. Agar selection plates containing ampicillin were warmed to 37 °C, followed by spreading 100 µL – 400 µL of cells and incubating overnight. Successful colonies were picked and amplified in 5 mL of LB media containing ampicillin overnight at 37 °C with shaking at 250 rpm. Protein was expressed by growing 200 µL of culture overnight in 200 mL of LB containing ampicillin at 37 °C with shaking at 250 rpm until OD_{600} = 0.8. Cell cultures were chilled to 4 °C, induced with 0.5 mM IPTG and 0.4 mM $MnCl_2$ and then incubated at 16 °C with shaking at 250 rpm for 16 h. Cells were harvested by centrifugation at 3000 x g at 4 °C for 15 min, washed once with buffer (50 mM HEPES, pH 7.5, 200 mM NaCl, 1 mM EGTA and 1 mM EDTA), then flash frozen in LN_2 and stored at -80 °C.

4.2.3 Purification of CaMKII.

Insect cells were processed based on modifications to the method described by Singla *et al.*[136] Briefly, frozen cells were thawed and resuspended in ice-cold lysis buffer comprised of 50 mM HEPES (pH 7.2, 7.5 or 8.0) containing 5% betaine, 1 mM EGTA, 1 mM EDTA, and 1X HALT protease inhibitor (Thermo Scientific). Insect cells were homogenized on ice with 10 strokes of a douncer. Bacterial cells were incubated briefly with lysozyme on ice then lysed by probe sonication. After homogenization, the crude lysate was clarified by centrifugation at 12,000 x g for 20 min at 4 °C, followed by ultracentrifugation of the supernatant at 100,000 x g for 1 h at 4 °C. The supernatant was decanted and then passed through a sterile 0.22 µm filter. The filtered sample was loaded at 0.5 mL/min onto an AKTA FPLC system fitted with either a Mono S 5/50 GL column or freshly-prepared phosphocellulose column (5 mL bed volume) with binding buffer containing 50 mM HEPES (pH 7.2, 7.5 or 8.0), 100 mM NaCl, and 1 mM EGTA. The column was washed with 5 column volumes (CV) of binding buffer, then eluted using a 100 mM – 1000 mM NaCl gradient in 4 CV. Peak fractions (typically 2 – 3 mL) were combined; 2 mM $CaCl_2$ and 10% glycerol were added and mixed. The sample was then transferred to a 5 mL tube containing 100 µL CaM-Sepharose beads equilibrated in 50 mM HEPES (pH 7.2, 7.5 or 8.0), 2 mM $CaCl_2$, 200 mM NaCl, and 10% glycerol. The reaction mixture was incubated on a rotisserie for 1 h (up to overnight) at 4 °C. The beads were washed 3 times by centrifugation at 500 x g for 5 min with three rounds of washes with wash buffer (10 CV, followed by 6 CV, followed by another 6 CV) containing 50 mM HEPES (pH 7.5), 2 mM $CaCl_2$, 500 mM NaCl,

and 10% glycerol, then incubated for 15 min with 2 CV of elution buffer containing 50 mM HEPES (pH 7.5), 400 mM NaCl, 4 mM EGTA and 30% glycerol. Aliquots of eluted protein were immediately flash frozen in LN_2 and stored at -80 °C.

4.2.4 CaMKII Phosphorylation and Activity.

Phosphorylated CaMKII (Thr286P) was produced by a reaction previously described by Bradshaw *et al.*[68] Briefly, a mixture containing 18 μM CaMKII, 50 μM CaM, 500 μM ATP, 500 μM $CaCl_2$ and 4 mM $MgCl_2$ was incubated on ice for 30 min. CaMKII phosphorylation was verified by gel Western staining with 22B1 anti-phospho-CaMKII antibody (Invitrogen).

Kinase activity was determined by radiolabeled ATP assay. A reaction mixture containing 50 mM HEPES, pH 7.5, 200 μM $CaCl_2$, 10 mM $MgCl_2$, 1 mg/mL BSA, 1 μM CaM, and 100 μM Syntide-2 was incubated at 30°C before adding 60 μCi/mL γ-^{32}P ATP (to a final concentration of 100 μM). The reaction was started by the addition of 10 nM CaMKIIα. Samples were spotted onto Whatman P81 paper every 15 s for the first minute, then every 30 s for the next two minutes. Papers were washed with 15% phosphoric acid four times and allowed to dry before scintillation counting.

4.2.5 Negative Stain TEM.

For negative stain EM, a final polishing step to confirm isolation of 12-mer holoenzymes was performed using a Superose 6 10/100 size exclusion column resulting in an elution fraction of 20 μg/mL in final buffer 20 mM HEPES, pH 7.5 and 200 mM NaCl. 3 μL of the sample was incubated on a glow-discharged, carbon-coated 400 mesh copper grid (CF400-Cu, Electron Microscopy Sciences) for 1 min, followed by washing with three drops of a freshly-prepared 1% uranyl formate solution, then wicked dry. Grids were imaged on an FEI Talos F200C equipped with a 4k x 4k BM-Ceta CCD camera operating at 200 kV in low-dose mode (10 e^-/A^2sec) at 73,000 X magnification and -5 μm defocus.

4.3 Results and Discussion

4.3.1 Expression of CaMKIIα

CaMKIIα was expressed in both E. coli cells and Tni insect cells to evaluate protein yield, cleavage/truncations, and autophosphorylation during expression. For E. coli expression, 1 L of BL21(DE3) cell culture was grown to OD_{600} = 0.8 before induction, chilled to 16 °C, then induced to express protein for 16 h. BL21 lanes show a faint band at 50 kD (Figure 1A) indicating lower expression, as noted previously [67]. While the yield can be increased by expressing larger volumes of cell culture, it is still hampered by the expression of a significant amount of truncated protein as seen in the band at 35 kD, caused either by early termination during translation or enzymatic cleavage, even when using a codon-optimized sequence and rare-codon enhanced BL21(DE3) cells. Allowing the expression to continue out to 72 h does not appear to increase full-length protein yield, but does enable CaMKII degradation during this extended period (shown in Figure 1A). An important addition to bacterial expression is the inclusion of a second gene containing human λ-phosphatase, which de-phosphorylates any kinase that may have been phosphorylated during expression. A small amount (0.4 mM) of $MnCl_2$ is required during expression as a cofactor for phosphatase activity. We observed almost no phosphorylation of CaMKII when expressed with this method as shown in Figure 1F. Lane 1 represents total CaMKII (6G9 mAb), and lane 2 shows a very slight band of Thr286-phosphorylated CaMKII (22B1 mAb).

For insect cell expression, we used two different culture types to produce the target. First, viral amplification was employed in adherent Sf9 cells grown in media supplemented with 5% FBS, thus allowing for higher MOI, improved adherence, a longer (5 d) incubation time, and smaller volumes of intermediate titer stock. After four rounds of amplification, the baculovirus was added to 200 mL spinner cultures of Tni cells grown in serum-free media. The expression had several parameters to optimize: expression time, seed density, infection concentration, and the use of expression additive. The outcome of this optimization is shown in Figure 1C.

Our results showed that the major expression product was full-length and not phosphorylated CaMKII (Figures 1B and 1G). Protein expression time yielded an optimal balance between CaMKII expression and cell viability between 60 and 72 h (Figure 1B), however, seeding density is important. Starting infection at 1.0 x 10^6 cells/mL produced fewer

truncation products than at higher densities. (Figure 1C). This may be due to the age and density of cells after 48 h of expression. Varying the amount of virus to induce expression also shows similar behavior. At 0.1% (1:1000) v/v infection, the MOI is below 1 and many cells must divide to amplify the virus until the MOI is high enough to produce a measurable amount of protein (Figure 1D). The increased cell density is similar to the higher seed density mentioned above. At 5% (1:20) v/v infection, however, the MOI is high enough to multiply infect all cells. The higher stress of excess virus and arrest of cell replication produces full-length protein, albeit at a lower yield. Boost Production Additive (BPA) from Expression Systems is described as a nutrient boost for cells during late-stage infection and protein expression. We examined the use of this additive at 24 h post-infection (per the manufacturer's instructions). Figure 1E shows that a greater amount of full-length protein is produced with the addition of BPA. Cell count and viability at the end of expression were similar regardless of BPA addition (data not shown). In summary, we found that Tni cultures seeded at $1x10^6$ cells/mL and infected with 1% (1:100) v/v high-titer virus, followed by the addition of 5% BPA 24 h post-infection and harvested at 72 h gave optimal results.

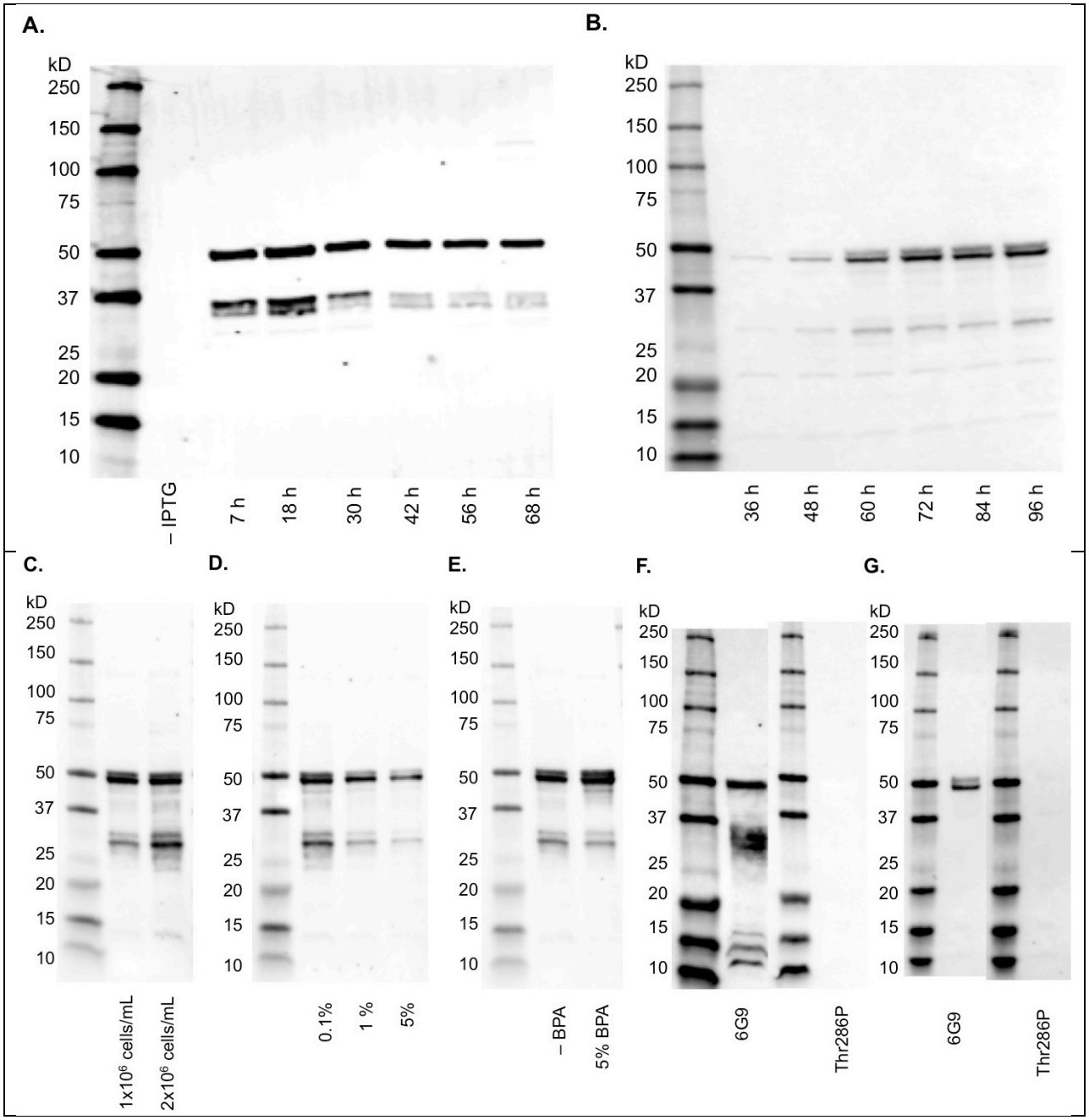

Figure 4.1. CaMKIIα expression time as a function of culture and cell type. (A) Bacterial expression system time course suggests that additional expression time does not enhance 50 kD full-length concentration, but does allow for degradation of 35 kD truncation products. (B) Baculovirus insect expression system time course demonstrates that full-length CaMKII (50 kD) and degradation products are expressed at a consistent ratio. Peak expression occurs at approximately 48 h. (C) BEVS seed density optimization (D) BEVS infection concentration optimization (E) BEVS expression additive optimization Clarified lysate of both (F) BL21 and (G) Tni expressions show no CaMKII phosphorylation during expression.

4.3.2 Purification

The goal of initial separation by ion-exchange chromatography was to concentrate the protein 10 fold to minimize the CaM-Sepharose purification volume in the second affinity step. While a slow gradient of salt can improve the removal of non-specific contaminants from the desired CaMKII elution fractions, it also increases the elution volume and may reduce protein concentration in further processing steps. Thus, we chose to vary the pH during ion exchange purification to find the optimal binding characteristics and maximize enrichment.

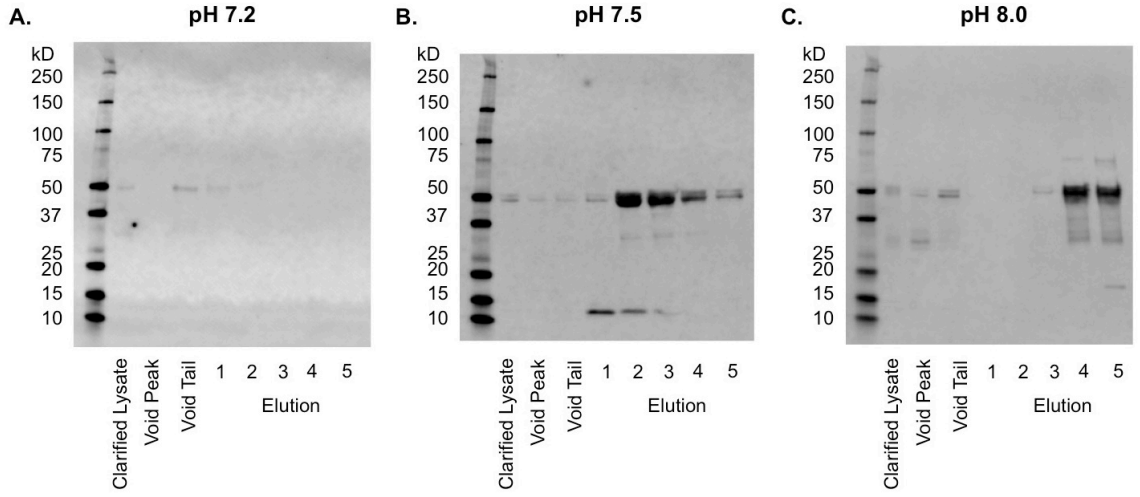

Figure 4.2. Ion-Exchange Chromatography Optimization – Initial separation of CaMKII from clarified lysate at (A) pH 7.2, (B) pH 7.5, and (C) pH 8.0. SDS-PAGE Western gels are labeled with anti-CaMKII monoclonal antibody 6G9.

The isoelectric point (pI) of CaMKII is approximately 6.6, as computed by the ExPASy server isoelectric point algorithm[145]. We chose three pH values to optimize the retention of CaMKII in the stationary phase while eliminating non-specific adsorption of other cellular proteins and debris. A Mono S column equilibrated at pH 7.2 binds CaMKII in lysis sample buffer completely and would be expected to maximize the selectivity for the protein since it is within one pH unit of the isoelectric point. However, the use of 5% betaine resulted in a significant change in ionic strength when the sample buffer was flushed from the column after loading. This operation caused a significant amount of CaMKII to desorb from the column before the elution step (Figure S1). In contrast, when running at pH 7.5, the column shows near complete retention of CaMKII until elution. The elution results in a single, narrow and

symmetric peak (Figure 2B). At pH 8.0, the Mono S column also shows complete retention of CaMKII as expected, however, the elution peak shows an asymmetric tail (Figure S2C), which is likely due to CaMKII re-binding to the column and increasing the elution volume. There also appears to be contamination eluting with the full-length protein (Figure 2C). Our results indicate that a pH of 7.5 is ideal for the initial separation of CaMKII from lysis buffer containing betaine.

The utility of phosphocellulose as a cationic exchange resin for CaMKII purification was also evaluated. Phosphocellulose powder is resuspended in water and must undergo several rounds of fines removal, followed by washing in an acid solution, a basic solution, then stabilization in buffer before pouring the column. This is a time-consuming effort that can produce varying results depending on the contact time with activation agents and the number of residual fines from handling. In contrast, pre-packed ion-exchange columns have predictable performance as well as simple regeneration. A side-by-side purification of insect clarified lysate was performed by comparing phosphocellulose and Mono S. Because the column volumes between Mono S and phosphocellulose differed (1 mL and 5 mL, respectively), we employed a CaM-Sepharose concentration step identically to both column elutions and made comparisons of those results (Figure 3).

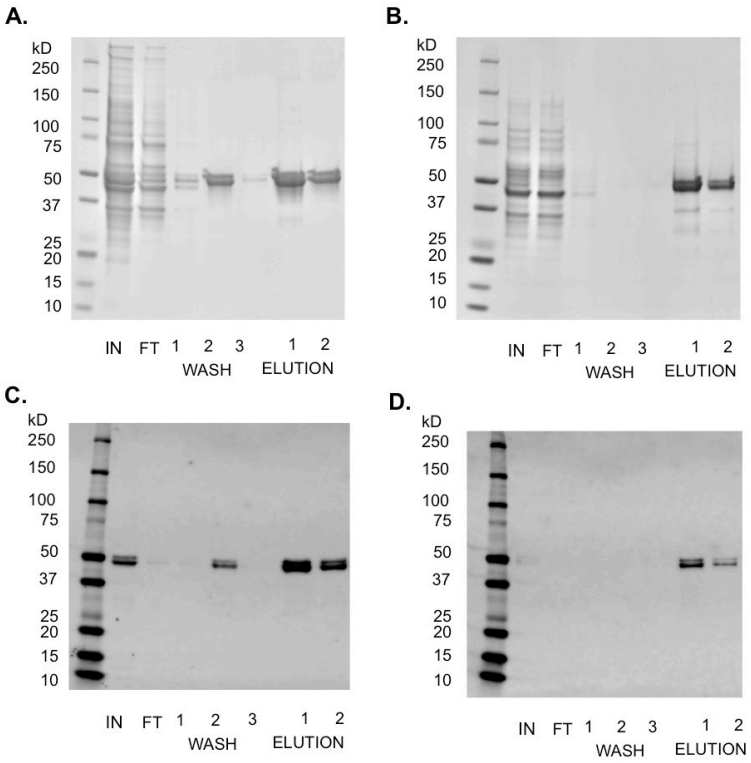

Figure 4.3. Analysis of concentrated CaMKII eluted from CaM-Sepharose after initial separation by either Mono S or phosphocellulose columns. A.) CaM-Sepharose enrichment Coomassie from 3 mL Mono S elution volume Coomassie. B.) CaM-Sepharose enrichment from 15 mL phosphocellulose elution volume Coomassie. C.) Western of A. D.) Western of B.

By using a batch method to purify CaMKII from ion-exchange elution buffer, we were able to increase the concentration 6-fold (Mono S) or 19-fold (phosphocellulose). One sample loading artifact observed in Figure 3A and Figure 3C is the band of CaMKII seen in wash step 2 in the Mono S purification that is not present in the phosphocellulose purification. This is attributed to some of the CaM-Sepharose resin accidentally being washed away when decanting the wash buffer from the resin after centrifugation. While this is not a common occurrence, we note that care must be taken when decanting to retain the resin during the wash and elution steps to maximize protein recovery. A more representative set of Mono S / CaM-Sepharose gels that do not have this artifact is shown in Figure 4.4.

4.3.3 Yield Comparison

Using our techniques with the BEVS system, we produced approximately 4 mg of CaMKII per liter of insect culture and a final concentration of 0.5 mg/mL (8.9 μM). While our yield is less than the results reported by Brickey et al, it contrasts greatly with the 10 μg/L yield reported by Rosenberg et al [42, 133].

Bacterial systems are ubiquitous in laboratories and are easier to set up and maintain than BEVS. However, the published yields of bacterial expression were remarkably low. Therefore, we performed an identical purification experiment in a bacterial system using the optimized conditions determined above to compare expression yields. The comparison results are shown in Figure 4. Our bacterial expression produced approximately 400 μg of CaMKII per liter of culture at a final concentration of 0.45 mg/mL. This measurement, however, is compromised by the remaining impurity still found in the CaM-Sepharose elution fractions, specifically two bands at approximately 100 kDa and 30 kDa that were bound by Ca^{2+}/CaM (Figure 4A), but were not detected by anti-CaMKII antibody (Figure 4C). Overall, the BEVS yield produces ten-fold more full-length CaMKII per liter of culture, at higher purity. We conclude that this reduces the purification burden when handling large volumes of lysate.

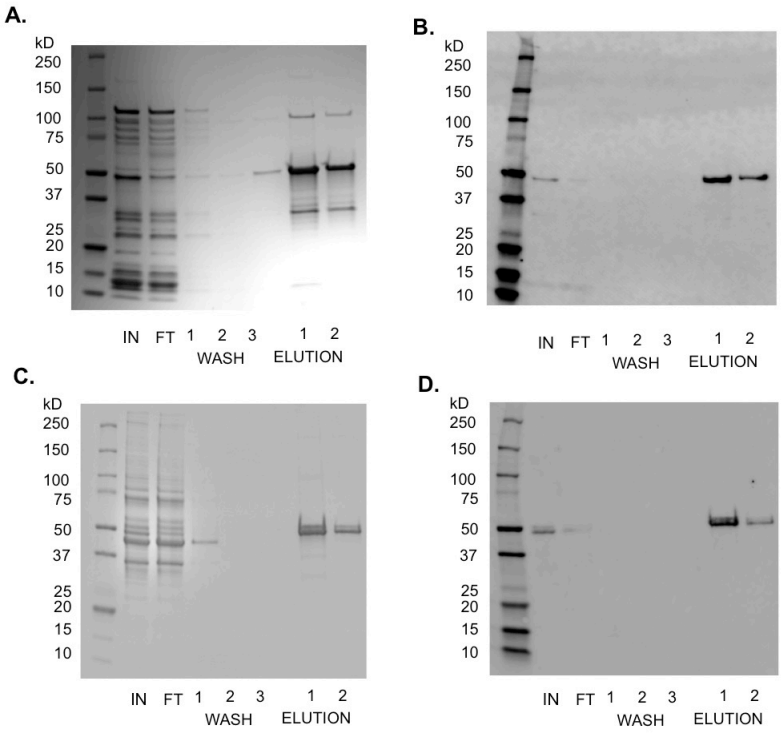

Figure 4.4. CaMKII CaM-Sepharose purification comparison between expression in BL21 cells (A and B) and Tni cells (C and D). Left side (A and C) are Coomassie-stained SDS-PAGE gels. Right side (B and D) are 6G9 Anti-CaMKIIα Western gels.

4.3.4 Characterization

Confirmation of CaMKIIα in dodecameric assembly was evaluated by two methods. A Coomassie-stained native PAGE gel shows a primary diffuse band just above the 720 kDa marker (expected mass is 648 kDa). A second faint band can be seen slightly higher. A size-exclusion chromatogram (Superose 6) contained a single peak eluting at the same time as thyroglobulin standard (660 kDa).

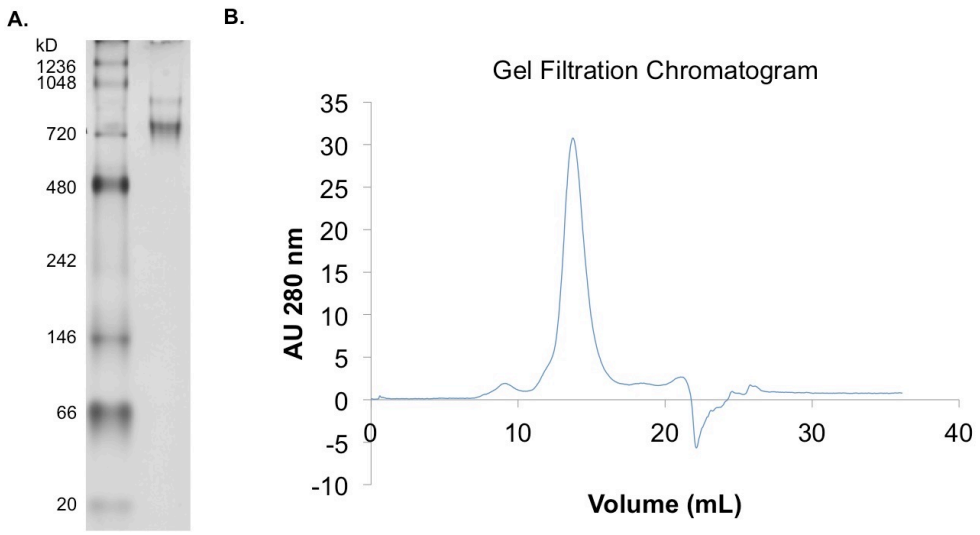

Figure 4.5. Characterization of two-stage purified CaMKII obtained from Tni cell expression. A.) Native PAGE, Coomassie staining. B.) Superose 6 size-exclusion chromatogram.

The specific activity of CaMKII was determined by the gold standard radiolabeled γ-32P-ATP assay using syntide-2 as a substrate. At 30 °C, the specific activity was measured to be 5 μmol/min/mg (Figure 6), which is comparable to previous reports [133, 136].

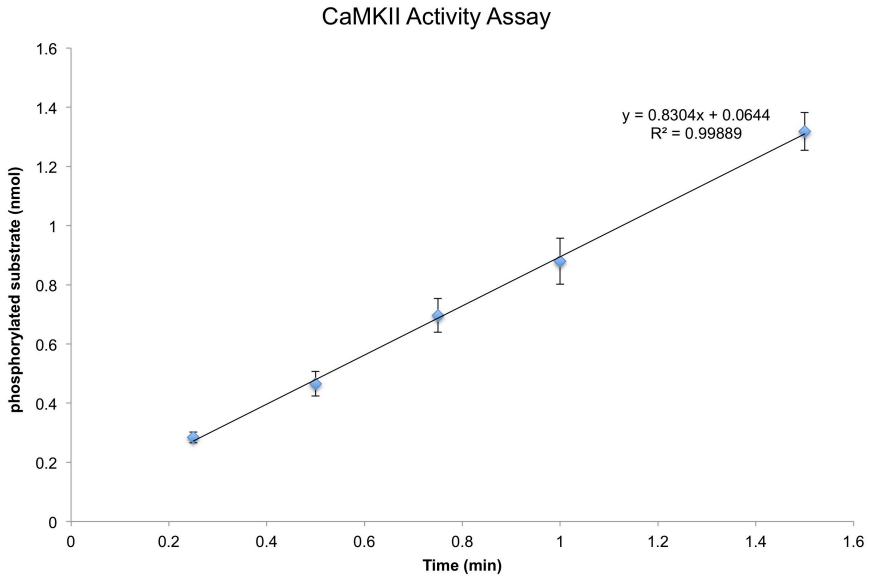

Figure 4.6. CaMKIIα Specific Activity. A.) Radiolabeled ATP Assay with Syntide-2 substrate performed at 30 °C gives a linear response within the first 90 s. Specific activity measured is 5 μmol/min/mg. Error bars represent n=3.

Negative-stain TEM micrographs show a largely mono-disperse oligomeric assembly of CaMKII. This morphology is consistent with prior observations of inhibited kinase: a circular hub domain with a center pore and punctate kinase domains randomly distributed within several nanometers of the hub circumference (Figure 7). It is important to note that protein adsorption to the TEM grid and the negative staining procedure (blotting and sample dehydration) is expected to flatten and distort flexible oligomers such as CaMKII.

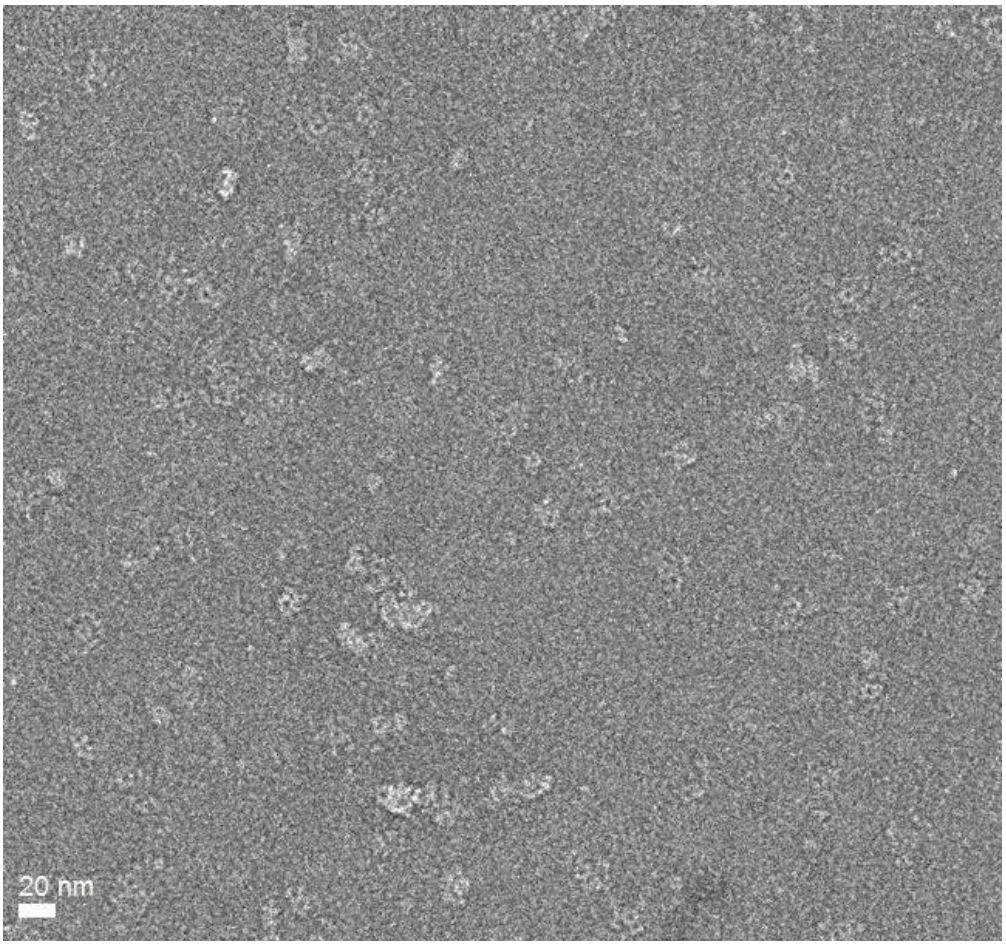

Figure 4.7. A representative negative stain TEM micrograph of CaMKIIα holoenzymes.

4.4 Conclusion

We have presented a detailed protocol and evaluation for the efficient, high-yield expression and purification of full-length wild-type human CaMKIIα. Our method is able to yielded 4 mg of autoinhibited enzyme per liter of baculovirus insect culture. A bacterial expression produced protein with a 10-fold lower yield. We demonstrated the purification of

either lysate to a final concentration of approximately 0.5 mg/mL while maintaining holoenzyme monodispersity. Lastly, it was shown that a Mono S ion-exchange column is preferable to phosphocellulose due to increased yield, purity, and ease of use.

CHAPTER 5. CRYO-ELECTRON TOMOGRAPHY OF CAMKII ALPHA

5.1 Introduction

Earlier in Chapter 2, it was concluded that both sample preparation and affinity grid design needed improvements to facilitate the structural study of CaMKII. Investigations in Chapters 3 and 4 yielded important information that motivated the design of new experiments. The negative stain TEM experiment in Chapter 4 demonstrated that multiple rounds of purification are needed to produce a homogenous and contaminant-free CaMKII sample amenable to structural study. It was also shown that the catalytic modules adsorb to the grid surface, either by the effect of the negative stain or by electrostatic attraction. Functionalized graphene oxide grids produced better transparency to the beam and enabled a sub-nanometer resolution structure of the test protein GroEL. Unfortunately, the graphene oxide surface was still able to nonspecifically adsorb protein to the grid, and the short length of the functional ligand may have distorted the conformation of GroEL from compression of the protein against the grid surface. Therefore, minimizing CaMKII catalytic modules adsorption to the grid is not possible with this surface. In summary, the lipid monolayer and graphene-oxide affinity grid techniques could not satisfy the requirements described in the purpose statement in Chapter 1. In this chapter, experiments were designed to investigate the quaternary structure behavior of hydrated CaMKII when no surface support is present. This is achieved by cryo-EM using holey carbon grids and optimally purified CaMKII by the method described in Chapter 4.

Two groups have performed cryo-EM using holey carbon grids, but the quaternary structures did not agree, and it was suggested that two different conformations had been observed[60]. Kolodziej *et al.* described a tall, cylindrical-shaped hub with foot-like extensions protruding out from the hub at a 30° angle [57] and produced a structure in a volume of 20 nm x 20 nm. In contrast, Myers *et al.* described a structure similarly seen in negative stain data, with catalytic modules occupying a 7.5–15 nm distance range coplanar to the 11 nm hub [60]. Therefore,

the reported holoenzyme diameter varied from 15 nm to 35 nm. Their data did not include a side view, however, and no thickness (or volume) was reported. The representative images reported in Figure 5.1 help explain the modes of the two reported models. On the left, the second and third class averages were chosen as side views to imply 6-2-2 symmetry. However, these views could also be interpreted as a self-associated dimer, both face-up and showing two pores, and a tilted face-up particle with a single pore. This might explain why the authors produced a 20 nm thick side view, which is the sum of two singular hub diameters, when other reports have not reported similar findings. On the right, the class average, shown in panel (d), used rotational symmetry on the face-up orientation to produce averages of the catalytic module placement that matched negative stain observations. In summary, cryo-EM experiments that produce side-view orientations and face-up averages without symmetry bias may corroborate previous reports or add new information about the conformation of autoinhibited CaMKIIα.

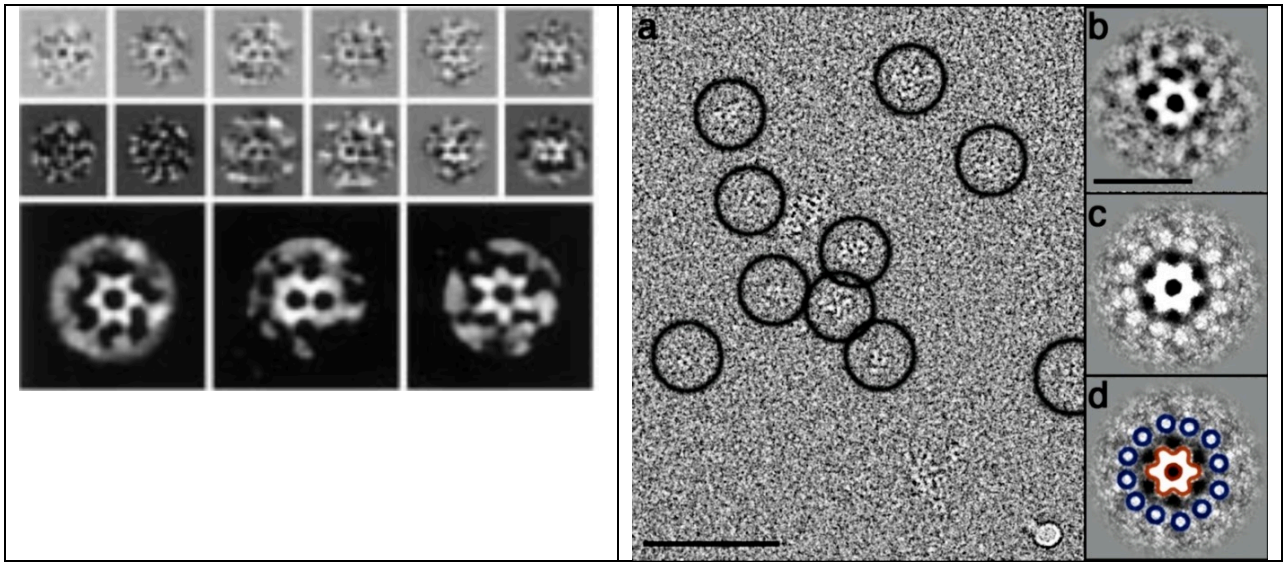

Figure 5.1. (Left) Cryo-EM class averages from Kolodziej *et al.*[57] with inverted contrast. (Right) Cryo-EM class average from Myers *et al.* [60] (supporting information). (CC BY)

5.2 Cryo-EM of Purified Wild Type CaMKIIα

5.2.1 Materials and Methods

For cryo-EM, wild type CaMKIIα expressed in Tni cells was purified according to methods described in Chapter 4, with the exception that CaM-Sepharose wash and elution steps

contained no glycerol, resulting in an elution fraction of ~0.4 mg/mL in final buffer of 50 mM HEPES, pH 7.5, 200 mM NaCl and 4 mM EGTA. Thick C-Flat holey carbon on 300 mesh copper grids (CF-1.2/1.3-3CU-T, Protochips) was negatively glow discharged at 15 mA for 30 s and used immediately. 5 μL of CaMKII was deposited onto the grid under 90% humidity, then immediately blotted for 1.5 s and plunged into liquid ethane using a CP3 plunger. Grids were imaged on an FEI Titan Krios equipped with an energy filter and K3 DDD camera. Images were captured in movie mode using 81,000 X magnification at 1.08 Å/pix and defocus range of -1.5 μm to -3.0 μm. The total dose was 55 $e^-/Å^2$. Movie frames were imported into EMAN 2.3 for the following post-processing steps: motion correction, particle picking, per-particle CTF correction, and reference-free 2D alignment.

5.2.2 Results and Discussion

Cryo-EM images were taken with an underfocus of 1.5 μm to -3.0 μm, which was closer to focus than in previous reports, and resulted in reduced particle contrast. However, the dose was increased to 55 $e^-/Å^2$ to compensate for the lower contrast. It became apparent, however, that the closer focus revealed individual particles with a pronounced star shape and this suggested an improved resolution overall (Figure 5.2). Additionally, particles showed little contamination contrast interference. Although ice thickness was calculated to be approximately 60 nm, aided by the use of 40 nm thick C-Flat holey carbon grids (data not shown), all recognizable CaMKIIα particles appeared to have a face-up orientation. Also seen in some of the images were particles embedded inside a halo of strong contrast, which may be indicative of particle adsorption to the air-water interface. Interestingly, catalytic modules extended away from the hubs were not easily seen when locating particles.

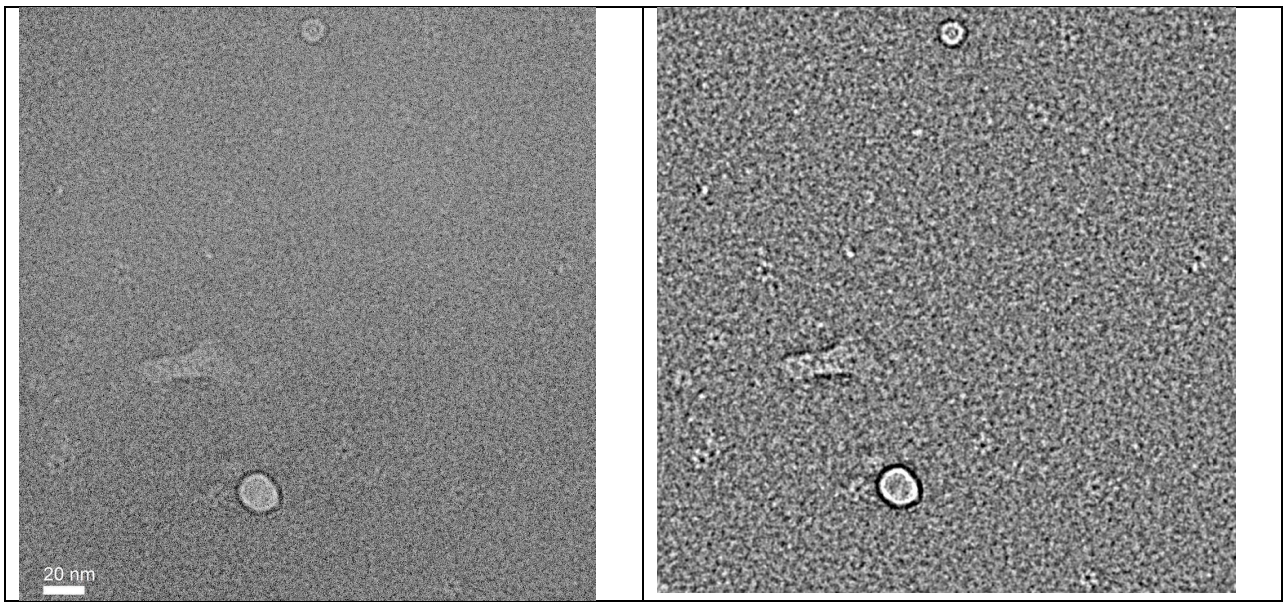

Figure 5.2. Representative cryo-EM image of purified BEVS WT CaMKIIα. (Left) Unfiltered image. (Right) Contrast-enhanced Wiener filtered image.

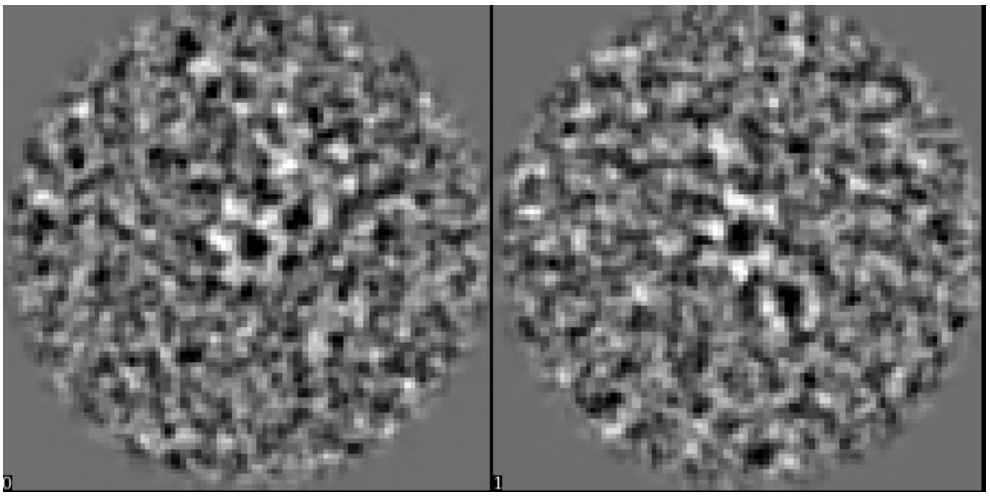

Figure 5.3. Two examples of self-associated holoenzymes.

Particle aggregation was present in the images, and two representative particles are shown in Figure 5.3 that resembles the proposed explanations of side-views (Kolodziej *et al.*) and catalytic module extensions (Myers *et al.*). The images show two distinct pores, but one particle of the pair has a more rectangular shape that may be a hub twisted axially from the other. One simulated projection of extended CaMKII conformation from Chapter 2, Figure 2.2, shows a side view with two stacked ring edges and a central pore that forms a rectangular shape. It is also

possible that interaction between the two hubs could impose a change in strain on one hub that partially dissociates the assembly, in a face-up orientation, into a flattened C shape.

Because of the similarity of views in this cryo-EM experiment, it is proposed that side-views cannot be unambiguously picked in this limited data set of 100 particles. Additionally, picking particles with a well defined central pore and star shape increases the certainty of picking "good" particles, but this method also mimics a template and produces bias. A much larger data set is likely to produce more discrete conformational classes, but these classes will suffer from orientation ambiguity as well.

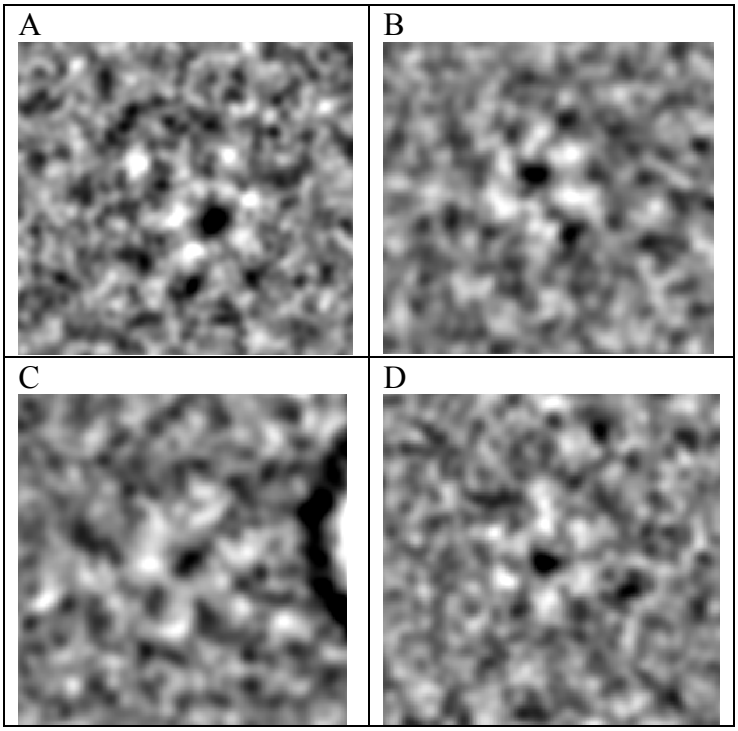

Figure 5.4. Individual cryo-EM particles with catalytic modules close to the hub.

Individual particles show strong punctate marks that decorate the hub and give the particle its gear-like shape (Figure 5.4). There are also instances where the punctate marks are distinct from the hub (Figure 5.4A), or closely linked (Figure 5.4B,C,D). Given that a vertical hub dimer (284 residues) is of similar size to a single catalytic module (311 residues), it is reasonable to expect the two to exhibit similar contrast. Therefore, these bright contrast marks may be catalytic domains, whether distant from the hub or coincident with the hub. The class

averages also lend support to this observation, as the spokes appear lengthened in the cryo-EM data (Figure 5.5). This could also be an artifact from the negative stain and dehydration, however.

It also appears that their in-plane directions vary. For example, Figure 5.4B shows elongated marks extending mostly outward from the center of the hub. In contrast, Figure 5.4D shows the elongated marks turned 90 degrees to follow the perimeter of the hub. This suggests that if the modules touch the hub, it may be because of a non-specific hydrophobic or electrostatic surface interaction that requires no rigid docking conformation. If these marks include the assembly of the hub domain, this indicates that the shape of the hub is more flexible than class averages from previous reports suggest and that distortions of the hexameric shape cannot be resolved unambiguously from rotations of the holoenzyme.

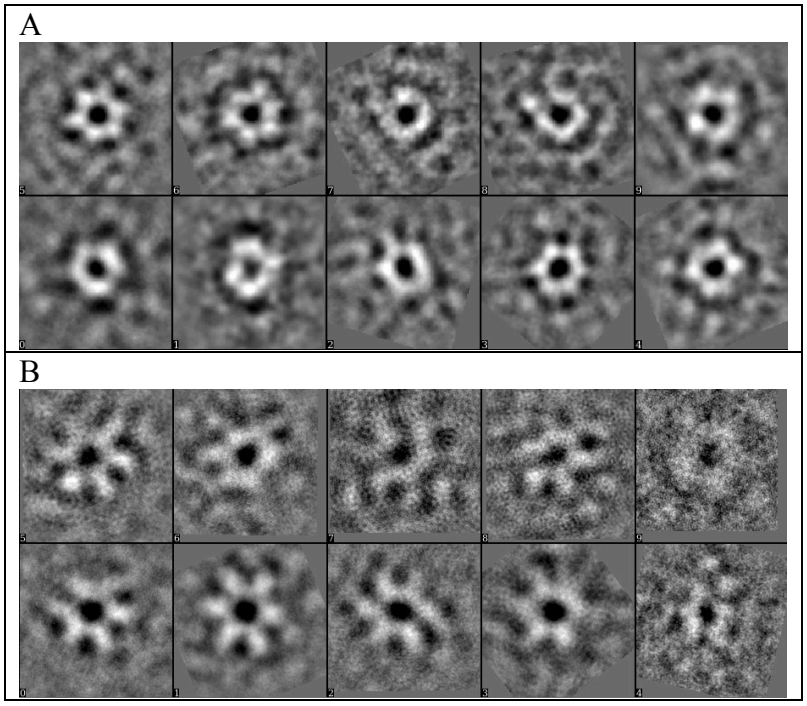

Figure 5.5. A) 2D class averages of 165 particles from multistage-purified wild-type CaMKII negative stain images. B) 2D class averages of 99 particles from BEVS WT CaMKII cryo-EM images.

In summary, not detecting a side view makes it impossible to place the catalytic modules within the holoenzyme volume. Although the bright punctate contrast seen in individual particles and coherent lengthening of the spoke in 2D class averages suggests that the catalytic modules may associate closely with the hub, it is still only a projection and therefore is constrained by superposition. It cannot be determined where the modules are orthogonal to the hub face, and the

variation in the orientation of each punctate mark also suggests flexibility of the hexameric ring. The combined problem makes the determination of the three-dimensional assembly using averaged 2D projections ambiguous and unresolvable. Therefore, to eliminate the problem of superposition, single-particle cryo-electron tomography can be used to generate unambiguous orientations of the hub and view distances of the catalytic modules from the top and bottom of the hub.

5.3 Cryo-Electron Tomography

The application of cryo-electron tomography (cryo-ET) and subtomogram averaging to elucidate high-resolution structures of heterogeneous complexes is still quite new, but recent experiments that exploit highly symmetric virus structure have produced sub-nanometer models [146] [147]. An additional benefit of cryo-ET is that experiments can be conducted in-situ, provided that the sample is sufficiently thin to allow the electron beam to pass through inelastically.

The collection of single-particle tomograms and the creation of detailed 3D density maps from subtomogram averages have challenges above and beyond cryo-EM, however. Data collection over a single target can take upwards of an hour because of the iterative process that requires focus calibration and location tracking for every tilt image in the series. Additionally, the data set created from the process is dramatically larger than in single-particle cryo-EM. Newer, highly-precise eucentric single-tilt stages are helpful to reduce the number of tracking and focus calibrations, permitting faster tilt-series capture [148]. Dual-axis tilt stages permit additional views to improve the missing wedge problem but are limited by further fractioning the dose into two dimensions. Instead of a typical 20-30 e-/A^2 dose for a single cryo-EM image, tilt series are collected over a much lower dose per tilt of 1-2 e-/A^2. Individual tilt images often do not display sufficient contrast, so the use of colloidal gold fiducials is required to align image stacks, though new algorithms have featured alignment using particles themselves, provided there is sufficient contrast [149]. Defocus and CTF estimation must be made on each reduced contrast tilt image. Even using a low-dose per tilt, the cumulative dose of the tilt-series is high enough to cause radiation damage. To improve image quality, a symmetric dose capture scheme distributes the initial dose at and near zero tilt where ice is thinnest and distortion from tilt angles is minimized. The dose is then split symmetrically across the tilt (+3°, +6°, -3°, -6°, etc.) until the maximal tilt is reached. Radiation damage is less important at these extremes because of the

distortions incurred by the high tilt angle. Computing subtomogram averages is analogous to single particle analysis in cryo-EM, and often thousands of subvolumes are needed to produce coherent averages because variations in morphology can occur in three dimensions rather than two. There are helpful reviews in the literature [150-151] [152] [153].

Ex-situ tomography has been performed on F-actin/CaMKII complexes to investigate the interaction of β subunits within the polymer [154] [155]. Surprisingly, the experiments used negative stain and not cryo-EM tomography.

5.3.1 Materials and Methods

Thick C-Flat holey carbon on 300 mesh copper grids (CF-1.2/1.3-3CU-T, Protochips) were negatively glow discharged at 15 mA for 30 s and used immediately. A 5 μL sample of CaMKIIα (~0.34 mg/mL) and 20 nm BSA-coated Au nanoparticles (0.4 mg/mL) in buffer of 50 mM HEPES, pH 7.5, 200 mM NaCl and 4 mM EGTA was deposited onto the glow-discharged grid under 90% humidity, followed immediately by 1.5 s blot and plunging into liquid ethane using a CP3 plunger.

Grids were imaged on an FEI Titan Krios operating at 300 keV equipped with energy filter and K3 DDD camera (8K x 8K pixels superresolution). Tilt-series images were captured in counting mode at 53,000 X magnification resulting in a pixel size of 0.825 Å/pix. Movies were collected using SerialEM software over a defocus range of -2.5 μm to -5.0 μm using a dose of 2 e^-/Å per tilt over a +60° to -60° tilt range with a 3° step using a dose-symmetric approach [156] [157]. The total dose for each tilt series was 82 $e^-/Å^2$. Movie frames were motion corrected using motioncor2 software, summed to produce tilt images, then CTF corrected using ctffind4 [74, 158].

Tilt series images were imported into IMOD for tomographic conversion [159]. Tilt alignment functions used image data binned by 8 (6.6 Å/pix), smoothed by anti-aliasing and linear filters, and fiducial markers. The resulting alignment parameters were used to generate an output tomogram using image data binned by 4 (3.3 Å/pix), then imported into PEET for particle sub-volume excising and subtomogram averaging [160]. Sub volumes of $(422)^3$ $Å^3$ were extracted from the tomogram. Volumes were aligned and averaged in four iterations of iterative angle refinement: 90° with 30° step, 45° with 15° step, 22.5° with 7° step, and 12° with 4° step. No symmetry was applied during averaging.

5.3.2 Results and Discussion

A set of 21 tilt series was acquired automatically using SerialEM software. The image capture was conducted at 0.826 Å/pix to give a balance between a resolution high enough to reveal the placement of subunits while still providing a field of view large enough to maintain tracking. The fractionated dose per tilt was 2 $e^-/Å^2$ and was considered the lowest dose able to generate contrast at high tilt angles. Total dose was 82 $e^-/Å^2$, which was high enough to cause radiation damage, but the use of a symmetric dose scheme isolated the damage to high-tilt images where distortion and ice thickness already compromised high-frequency features. Particle defocus ranged between -3.5 μm and -5 μm defocus.

It was confirmed that CaMKII particles surrounded by a halo were in fact at the air-water interface, and so these particles were avoided. Using the zero-degree tilt images to manually pick particles yielded 26 particles with contrast through all tilt angles. While more particles were visible in the comprehensive tilt series collection, many particles suffered from lack of visible contrast even at mild tilt angles, some particles were adsorbed to the air-water interface, and some tilt series did not maintain tracking making alignment impossible. A minimum of 3.5 μm underfocus was required to produce contrast in tilt images.

The tomogram was further processed by PEET software to extract subtomogram particle volumes. No catalytic module contrast was detected in any individual subvolume, which was similar to observations made with single particle cryo-EM. The subtomogram volumes were aligned through four rounds of iterative angle refinement with no implied symmetry, then summed to represent the average of all the particles. Samples of Z-slices through this averaged volume are shown in Figure 5.6.

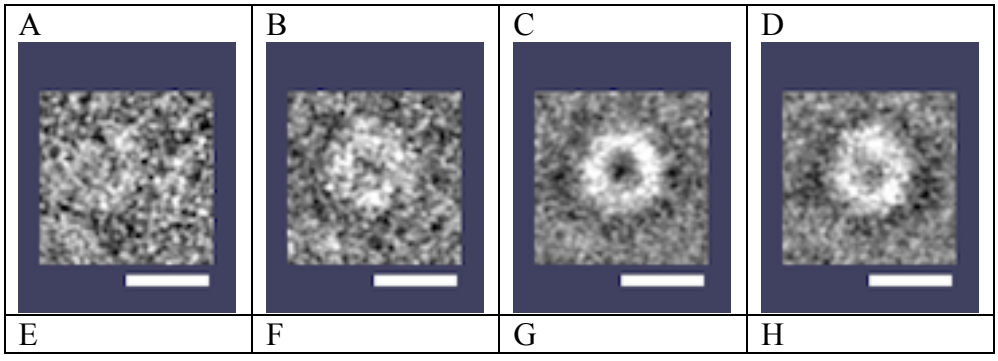

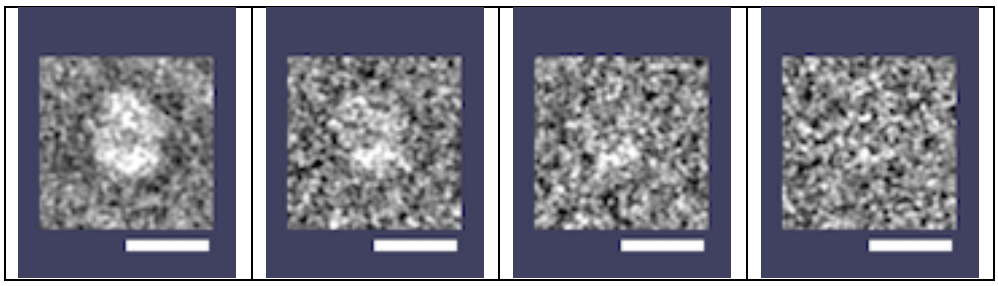

Figure 5.6. (A–H) Equidistant Z-slices through subtomogram average. Scale bar = 10 nm.

Lastly, the subvolume was mapped to a 3D contour model, shown in Figure 5.7A and B. As expected, a central pore is visible through a cylindrical hub that tapers in diameter at the top and bottom. Some density above the noise threshold is found within the region of extended catalytic modules, but this density could also be additive noise. The full length of the hub including the additional density measured approximately 30 nm, while the length of the hub barrel was measured to be approximately 16 nm.

Chimera was used to fit the model to the two reported models discussed earlier. The central hub of our model appears to have additional density above and below the EM density map reported by Myers *et al.* This additional density may be from catalytic modules that were observed as bright spots in cryo-EM images. Another interpretation of this density may be that elongation is often observed in the direction of the beam due to the missing wedge problem.

The additional density appears to fit better into the crystal structure of Chao *et al.* converted to an EM density map filtered to 20 Å, but the foot-like catalytic model extensions are not present in our map. In summary, the number of subtomograms used to produce the average is not sufficient to reveal the location probability of catalytic modules.

5.3.3 Conclusion

The next experiment must acquire many more particles to reduce noise and increase the resolution of the hub assembly. For rigid assemblies with high symmetry, thousands of particles are required to reduce noise and increase the resolution to the sub-nanometer range [147]. Even more will be needed for CaMKIIα, given the flexibility of the hub assembly. A significant improvement to the data collection process is to increase the concentration of CaMKII particles inside the grid holes yet avoid the air-water interface. An increased particle count on the grid may also yield more orientations. Another option is to increase the ice thickness to 80 nm, but

this must be balanced against the difficulty of finding the particle with reduced contrast. This must be balanced against the increase in aggregation seen at high concentrations during grid sample preparation. Lastly, the use of a eucentric single-tilt holder will also improve the speed of data collection and improve tracking, resulting in less wasted data from tracking corruption.

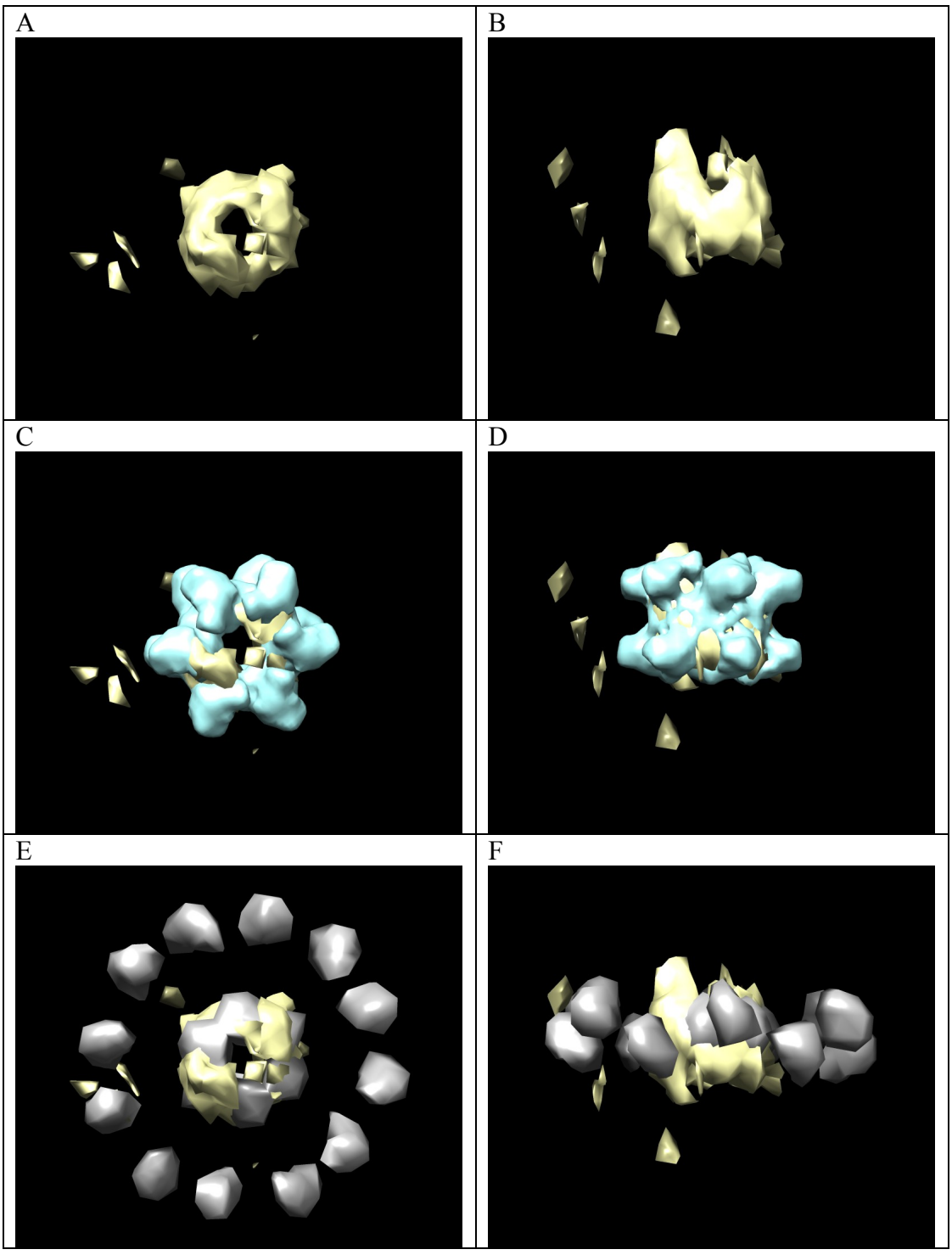

Figure 5.7. 3D contour model of the CaMKIIα holoenzyme from a subtomogram average of 26 particles. (A) Face view and (B) side view of the model, shown in yellow. (C) Face view and (D) side view of the model (yellow) fit to a proposed compact autoinhibited crystal structure (PDBID 3SOA) (blue). (E) Face view and (F) side view of the model (yellow) fit to a proposed extended autoinhibited EM density map (EMDB EMD-8514) (gray).

CHAPTER 6. CONCLUSIONS

The determination of the quaternary structure of the CaMKII holoenzyme has been attempted for nearly 20 years by a variety of methods, with no one method giving a definitive structure. Problems in obtaining a structure originated with observation methods that estimated quaternary shape from low-resolution ensemble averages or required significant alteration of the protein to enforce a particular conformation. When these limitations were removed by using full-length wild type CaMKIIα and observed under conditions free of surface interactions, it became apparent that its orientation in three-dimensional space could not be unambiguously determined. The assembly of the hexameric hub rings appeared to have flexible orientation, plus two-dimensional projections contained superposition problems that prevented the determination of the orientation of the hub and placement of tethered catalytic modules. The use of cryo-electron tomography and subtomogram averaging provides a way to resolve the superposition problems and form coherent 3D class averages to both solve the orientation of the hub assembly and evaluate the probability of catalytic modules found above or below the hub. Conditions were found to perform CET on CaMKIIα, but further work is needed to optimize the maximal dose, number of tilts, and number of monodisperse particles per tomogram to generate thousands of subvolumes containing catalytic module density. With this data, it is proposed that three-dimensional averages determined by maximum-likelihood classification resolve conformations of the hub, and then statistical methods may be applied to each conformer to highlight probabilities of catalytic association with the hub and any preference for specific locations on its sphere. Lastly, this analysis may reveal the existence of catalytic dimers.

Once the experiment has elucidated an unambiguous three-dimensional structure of the autoinhibited holoenzyme, it opens a world of experiments that observe the behavior of the holoenzyme in interactions with binding partners, both ex-situ and in-situ. A shortlist of experiments that will yield additional understand of holoenzyme structure and function are:

- Ca^{2+}/CaM-bound CaMKIIα
- Thr286-phosphorylated CaMKIIα
- Thr305/Thr306-phosphorylated CaMKIIα
- F-actin-bound CaMKIIα/β
- NR2B-bound CaMKIIα

These experiments can benefit from ongoing improvements to cryo-electron tomography, including the use of highly-precise eucentric single-tilt stages that enable faster data collection, increased DDD SNR to permit fractionation of smaller electron doses, automated tomogram reconstruction, 3D CTF correction, and inline reconstruction during target imaging to provide real-time microscope adjustments that minimize the processing of poor data. CaMKIIα is and remains a challenging molecule to observe, but there is good confidence that the latest generation of tools will reveal a solution to this structure and bring new functional insight towards this fascinating kinase.

APPENDIX A. SUPPLEMENTAL INFORMATION – OPTIMAL METHOD FOR THE EXPRESSION AND PURIFICATION OF HUMAN CAMKII ALPHA

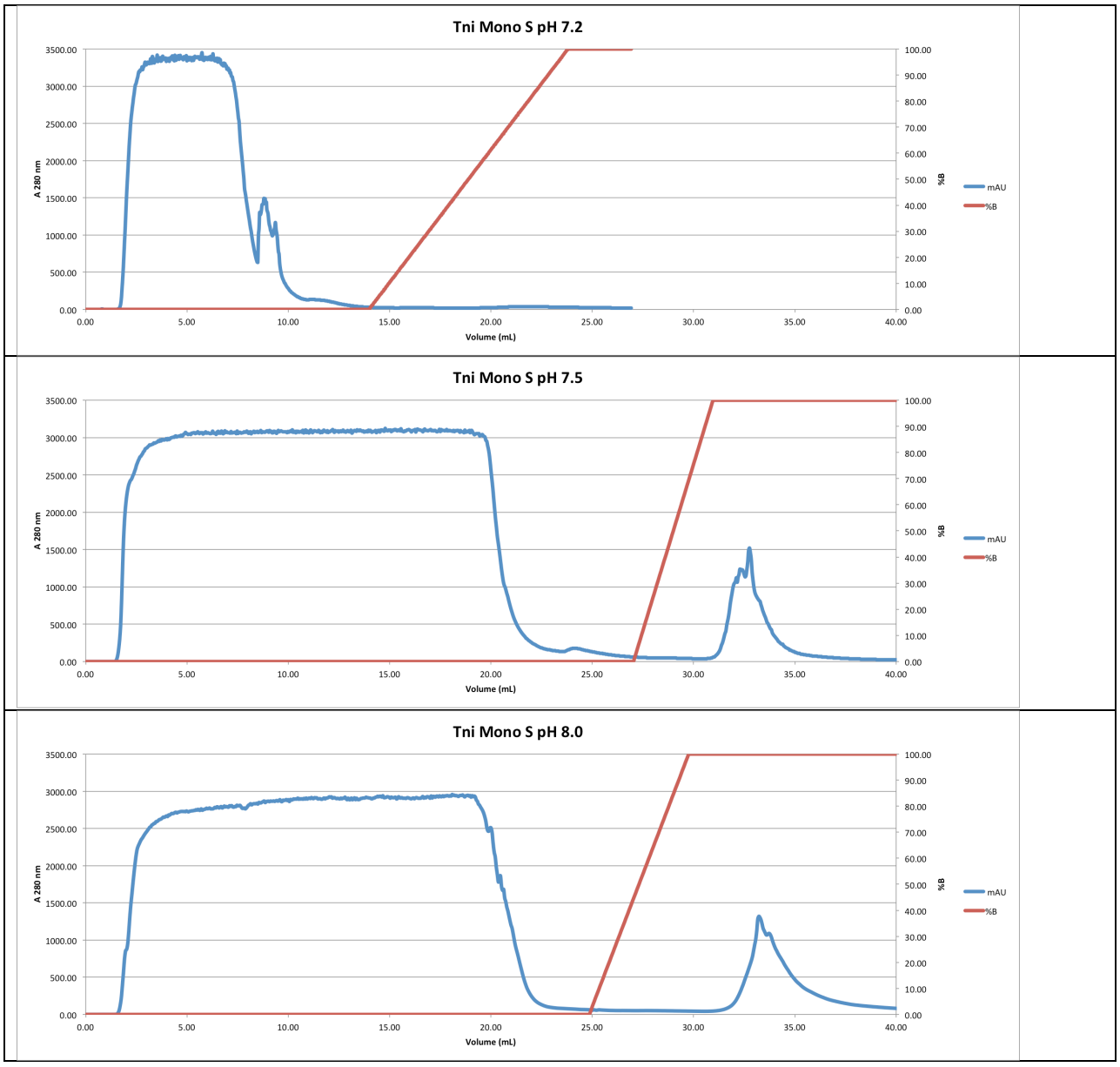

Figure S1. Mono S chromatograms at (A) pH 7.2, (B) pH 7.5, and (C) pH 8.0

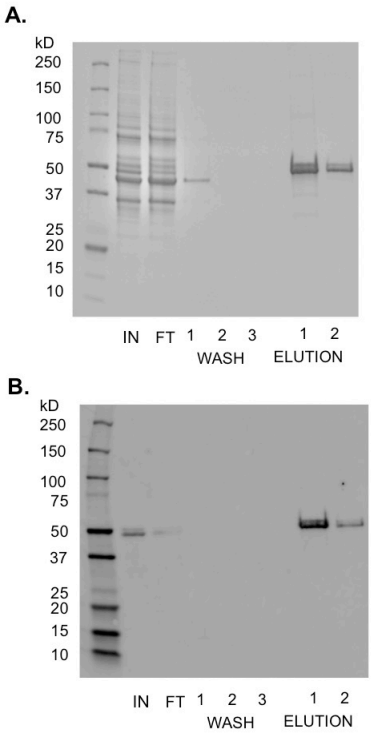

FIX

Figure S2. Representative SDS-PAGE and Western gels of the CaM-Sepharose purification step using Mono S elution from Tni lysate. Legend: IN – combined Mono S elution fractions, FT – CaM-Sepharose column flow-through.

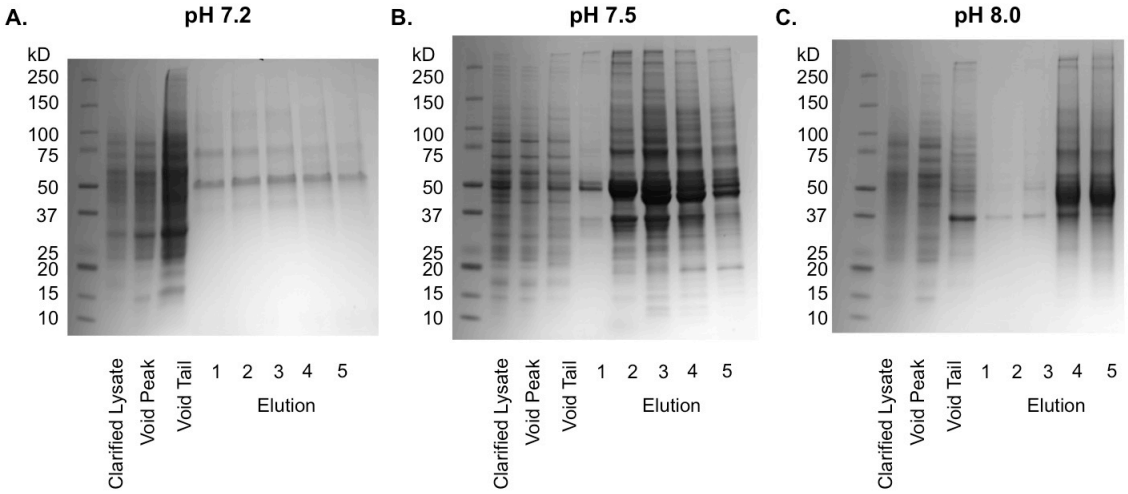

Figure S3. Ion-Exchange Chromatography Optimization – Initial separation of CaMKII from clarified lysate at (A) pH 7.2, (B) pH 7.5, and (C) pH 8.0. SDS-PAGE Coomassie gels directly correspond to Western-stained gels in Figure 4.2.

APPENDIX B. SUPPLEMENTAL INFORMATION – SELECTIVE CAPTURE OF HISTIDINE-TAGGED PROTEINS FROM CELL LYSATES USING TEM GRIDS MODIFIED WITH NTA-GRAPHINE OXIDE

Graphene-Oxide-NTA Synthesis. GO was synthesized using an improved Hummers' method that is easier to execute, is higher yielding, and does not evolve toxic gases (Figure 1B). It has been reported that there is no decrease in conductivity in the final product between the original and improved method, making it an attractive route for large scale production of GO [Marcano, D.C., *et al. ACS Nano* **2010** *4*, 4806-4814]. When a 9:1 mixture of H_2SO_4 and H_3PO_4 (130 mL total volume) was stirred with 1 g of graphite flakes (F516 flake graphite, 200-300 mesh, Asbury Carbons, Inc.) and $KMnO_4$ (6.0 g, 6.0 wt. equiv.), the reaction began with heating to ~40 °C and proceeded with further heating and stirring at 50 °C for 12 hours before cooling to 20 °C and pouring the reaction mixture into 120 mL of ice cold-water with 1 mL 30% H_2O_2. Next, this suspension was passed through a metal U.S. Standard testing sieve (W.S. Tyler, 300 μm) and then passed through a glass wool plug to filter larger particulates. The filtrate was then centrifuged at 4,000 rpm for 4 h, the supernatant discarded, and the pellet washed twice with a 1:1:1 volumetric ratio of H_2O, 30% HCl, and EtOH before passing the material through the testing sieve and centrifuging the filtrate at 4,000 rpm for 4 h to pellet the aggregated material. The supernatant was precipitated with Et_2O (200 mL) and filtered through a 0.45 μm PTFE membrane to gather the solid. The final material was dried under a 15 μm vacuum for 12 h, yielding 1.8 g of GO.

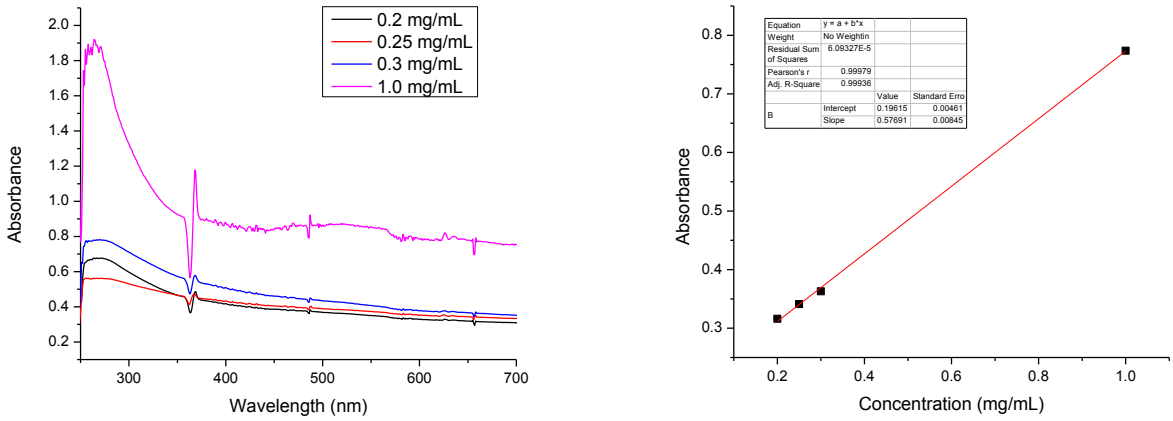

Figure S1. A: Absorption spectra for GO-NTA as a function of concentration; and B: Calibration curve for GO-NTA.

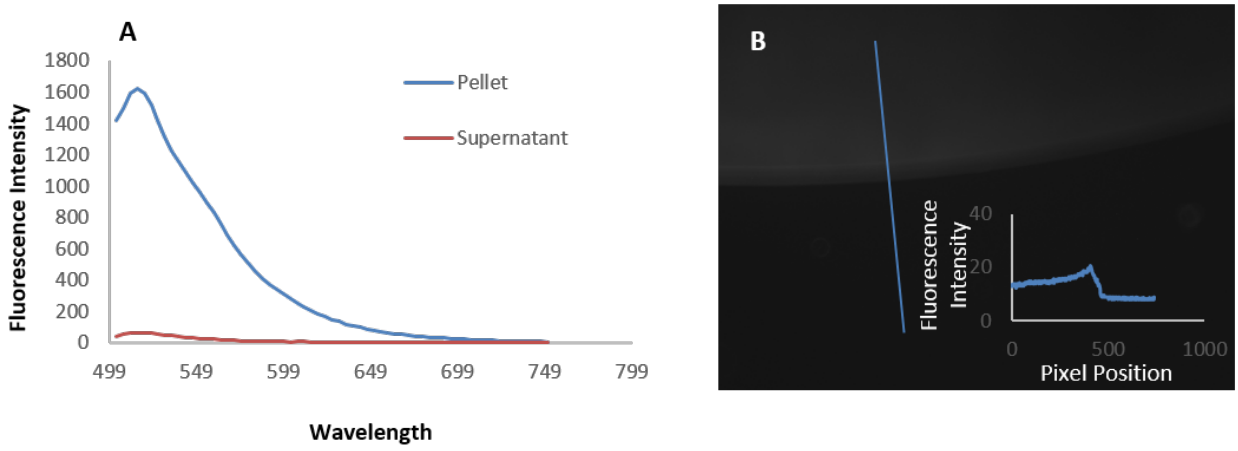

Figure S2. Analysis of Fluorescein-PABA-GO-NTA films by (A) fluorescence spectroscopy and (B) epifluorescence microscopy. Fluorescence spectra were measured for the supernatant (A, red spectrum) and the pellet (A, blue spectrum) after reaction of PABA-GO with amino-fluorescein. Epifluorescence image of F-PABA-GO-NA after LS-transfer onto a 400 mesh TEM grid; Inset: position-dependent intensity of F-PABA-GO-NA film on the TEM grid across the region indicated by the line in the epifluorescence image.

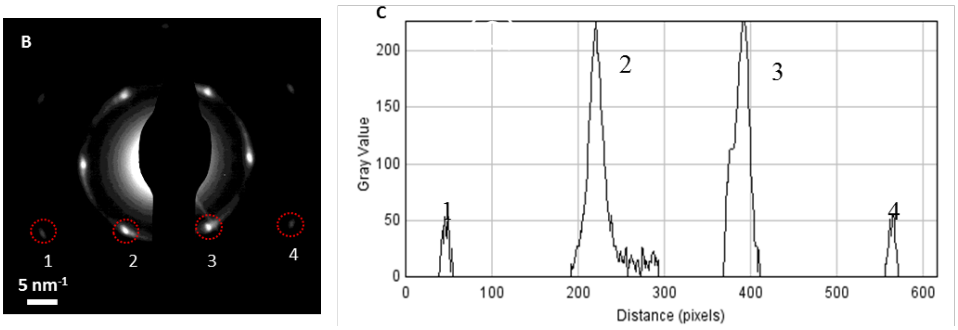

Figure S3. Selected area electron diffraction analysis of GO-NTA film on TEM grid. The hexagonal pattern of sharp diffraction peaks (left), as well as their spacing and intensity (right) are consistent with deposition of a single GO-NTA layer onto the grid via Langmuir-Schaefer transfer from IPA/H_2O.

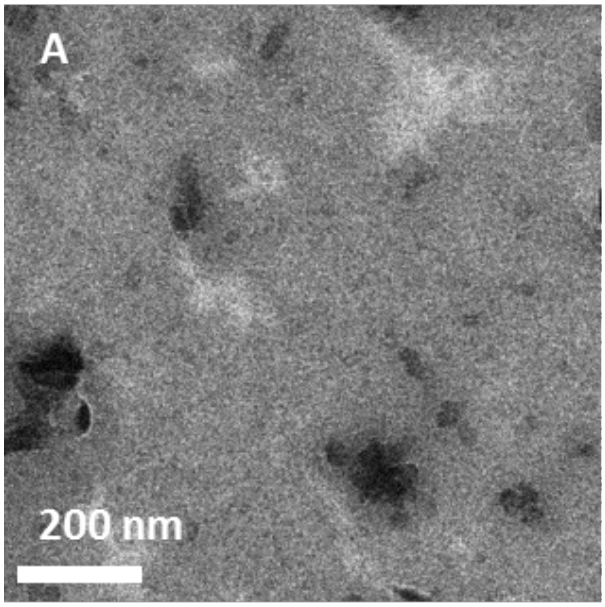

Figure S4. Negative stain TEM of his_6-T7 lysate deposited onto BSA-PABA-GO-NTA in the absence of Ni^{2+} activation.

REFERENCES

1. Frankland, P. W.; O'Brien, C.; Ohno, M.; Kirkwood, A.; Silva, A. J., Alpha-CaMKII-dependent plasticity in the cortex is required for permanent memory. *Nature* **2001,** *411* (6835), 309-13.

2. Mesulam, M. M., Neuroplasticity failure in Alzheimer's disease: bridging the gap between plaques and tangles. *Neuron* **1999,** *24* (3), 521-9.

3. Plassman, B. L.; Langa, K. M.; Fisher, G. G.; Heeringa, S. G.; Weir, D. R.; Ofstedal, M. B.; Burke, J. R.; Hurd, M. D.; Potter, G. G.; Rodgers, W. L.; Steffens, D. C.; Willis, R. J.; Wallace, R. B., Prevalence of dementia in the United States: the aging, demographics, and memory study. *Neuroepidemiology* **2007,** *29* (1-2), 125-32.

4. Alzheimer's, A., 2016 Alzheimer's disease facts and figures. *Alzheimers Dement* **2016,** *12* (4), 459-509.

5. Maresova, P.; Mohelska, H.; Dolejs, J.; Kuca, K., Socio-economic Aspects of Alzheimer's Disease. *Curr Alzheimer Res* **2015,** *12* (9), 903-11.

6. Anand, K. S.; Dhikav, V., Hippocampus in health and disease: An overview. *Ann Indian Acad Neurol* **2012,** *15* (4), 239-46.

7. Emery, V. O., Alzheimer disease: are we intervening too late? Pro. *J Neural Transm (Vienna)* **2011,** *118* (9), 1361-78.

8. Morrison, J. H.; Hof, P. R., Life and death of neurons in the aging brain. *Science* **1997,** *278* (5337), 412-9.

9. Sheng, M.; Hoogenraad, C. C., The postsynaptic architecture of excitatory synapses: a more quantitative view. *Annu Rev Biochem* **2007,** *76*, 823-47.

10. Ascher, P.; Nowak, L., The role of divalent cations in the N-methyl-D-aspartate responses of mouse central neurones in culture. *J Physiol* **1988,** *399*, 247-66.

11. Cheng, D.; Hoogenraad, C. C.; Rush, J.; Ramm, E.; Schlager, M. A.; Duong, D. M.; Xu, P.; Wijayawardana, S. R.; Hanfelt, J.; Nakagawa, T.; Sheng, M.; Peng, J., Relative and absolute quantification of postsynaptic density proteome isolated from rat forebrain and cerebellum. *Mol Cell Proteomics* **2006,** *5* (6), 1158-70.

12. Dosemeci, A.; Weinberg, R. J.; Reese, T. S.; Tao-Cheng, J. H., The Postsynaptic Density: There Is More than Meets the Eye. *Front Synaptic Neurosci* **2016,** *8*, 23.

13. Wayman, G. A.; Lee, Y. S.; Tokumitsu, H.; Silva, A. J.; Soderling, T. R., Calmodulin-kinases: modulators of neuronal development and plasticity. *Neuron* **2008,** *59* (6), 914-31.

14. Shonesy, B. C.; Jalan-Sakrikar, N.; Cavener, V. S.; Colbran, R. J., CaMKII: a molecular substrate for synaptic plasticity and memory. *Prog Mol Biol Transl Sci* **2014,** *122*, 61-87.

15. Snow, W. M.; Albensi, B. C., Neuronal Gene Targets of NF-kappaB and Their Dysregulation in Alzheimer's Disease. *Front Mol Neurosci* **2016,** *9*, 118.

16. Ghosh, A.; Giese, K. P., Calcium/calmodulin-dependent kinase II and Alzheimer's disease. *Mol Brain* **2015,** *8* (1), 78.

17. Yoshimura, Y.; Ichinose, T.; Yamauchi, T., Phosphorylation of tau protein to sites found in Alzheimer's disease brain is catalyzed by Ca2+/calmodulin-dependent protein kinase II as demonstrated tandem mass spectrometry. *Neurosci Lett* **2003,** *353* (3), 185-8.

18. Elgersma, Y.; Fedorov, N. B.; Ikonen, S.; Choi, E. S.; Elgersma, M.; Carvalho, O. M.; Giese, K. P.; Silva, A. J., Inhibitory autophosphorylation of CaMKII controls PSD association, plasticity, and learning. *Neuron* **2002,** *36* (3), 493-505.

19. Giese, K. P.; Fedorov, N. B.; Filipkowski, R. K.; Silva, A. J., Autophosphorylation at Thr286 of the alpha calcium-calmodulin kinase II in LTP and learning. *Science* **1998,** *279* (5352), 870-3.

20. Silva, A. J.; Stevens, C. F.; Tonegawa, S.; Wang, Y., Deficient hippocampal long-term potentiation in alpha-calcium-calmodulin kinase II mutant mice. *Science* **1992,** *257* (5067), 201-6.

21. Bejar, R.; Yasuda, R.; Krugers, H.; Hood, K.; Mayford, M., Transgenic calmodulin-dependent protein kinase II activation: dose-dependent effects on synaptic plasticity, learning, and memory. *J Neurosci* **2002,** *22* (13), 5719-26.

22. Yamagata, Y.; Kobayashi, S.; Umeda, T.; Inoue, A.; Sakagami, H.; Fukaya, M.; Watanabe, M.; Hatanaka, N.; Totsuka, M.; Yagi, T.; Obata, K.; Imoto, K.; Yanagawa, Y.; Manabe, T.; Okabe, S., Kinase-dead knock-in mouse reveals an essential role of kinase activity of Ca2+/calmodulin-dependent protein kinase IIalpha in dendritic spine enlargement, long-term potentiation, and learning. *J Neurosci* **2009,** *29* (23), 7607-18.

23. Kury, S.; van Woerden, G. M.; Besnard, T.; Proietti Onori, M.; Latypova, X.; Towne, M. C.; Cho, M. T.; Prescott, T. E.; Ploeg, M. A.; Sanders, S.; Stessman, H. A. F.; Pujol, A.; Distel, B.; Robak, L. A.; Bernstein, J. A.; Denomme-Pichon, A. S.; Lesca, G.; Sellars, E. A.; Berg, J.; Carre, W.; Busk, O. L.; van Bon, B. W. M.; Waugh, J. L.; Deardorff, M.; Hoganson, G. E.; Bosanko, K. B.; Johnson, D. S.; Dabir, T.; Holla, O. L.; Sarkar, A.; Tveten, K.; de Bellescize, J.; Braathen, G. J.; Terhal, P. A.; Grange, D. K.; van Haeringen, A.; Lam, C.; Mirzaa, G.; Burton, J.; Bhoj, E. J.; Douglas, J.; Santani, A. B.; Nesbitt, A. I.; Helbig, K. L.; Andrews, M. V.; Begtrup, A.; Tang, S.; van Gassen, K. L. I.; Juusola, J.; Foss, K.; Enns, G. M.; Moog, U.; Hinderhofer, K.; Paramasivam, N.; Lincoln, S.; Kusako, B. H.; Lindenbaum, P.; Charpentier, E.; Nowak, C. B.; Cherot, E.; Simonet, T.; Ruivenkamp, C. A. L.; Hahn, S.; Brownstein, C. A.; Xia, F.; Schmitt, S.; Deb, W.; Bonneau, D.; Nizon, M.; Quinquis, D.; Chelly, J.; Rudolf, G.; Sanlaville, D.; Parent, P.; Gilbert-Dussardier, B.; Toutain, A.; Sutton, V. R.; Thies, J.; Peart-Vissers, L.; Boisseau,

P.; Vincent, M.; Grabrucker, A. M.; Dubourg, C.; Undiagnosed Diseases, N.; Tan, W. H.; Verbeek, N. E.; Granzow, M.; Santen, G. W. E.; Shendure, J.; Isidor, B.; Pasquier, L.; Redon, R.; Yang, Y.; State, M. W.; Kleefstra, T.; Cogne, B.; Gem, H.; Deciphering Developmental Disorders, S.; Petrovski, S.; Retterer, K.; Eichler, E. E.; Rosenfeld, J. A.; Agrawal, P. B.; Bezieau, S.; Odent, S.; Elgersma, Y.; Mercier, S., De Novo Mutations in Protein Kinase Genes CAMK2A and CAMK2B Cause Intellectual Disability. *Am J Hum Genet* **2017,** *101* (5), 768-788.

24. Bayer, K. U.; Schulman, H., CaM Kinase: Still Inspiring at 40. *Neuron* **2019,** *103* (3), 380-394.

25. Coultrap, S. J.; Bayer, K. U., CaMKII regulation in information processing and storage. *Trends Neurosci* **2012,** *35* (10), 607-18.

26. Hell, J. W., CaMKII: claiming center stage in postsynaptic function and organization. *Neuron* **2014,** *81* (2), 249-65.

27. Hudmon, A.; Schulman, H., Structure-function of the multifunctional Ca2+/calmodulin-dependent protein kinase II. *Biochem J* **2002,** *364* (Pt 3), 593-611.

28. Kennedy, M. B., Synaptic Signaling in Learning and Memory. *Cold Spring Harb Perspect Biol* **2013,** *8* (2), a016824.

29. Kim, K.; Saneyoshi, T.; Hosokawa, T.; Okamoto, K.; Hayashi, Y., Interplay of enzymatic and structural functions of CaMKII in long-term potentiation. *J Neurochem* **2016,** *139* (6), 959-972.

30. Lisman, J.; Yasuda, R.; Raghavachari, S., Mechanisms of CaMKII action in long-term potentiation. *Nat Rev Neurosci* **2012,** *13* (3), 169-82.

31. Tobimatsu, T.; Fujisawa, H., Tissue-specific expression of four types of rat calmodulin-dependent protein kinase II mRNAs. *J Biol Chem* **1989,** *264* (30), 17907-12.

32. Erondu, N. E.; Kennedy, M. B., Regional distribution of type II Ca2+/calmodulin-dependent protein kinase in rat brain. *J Neurosci* **1985,** *5* (12), 3270-7.

33. Tombes, R. M.; Faison, M. O.; Turbeville, J. M., Organization and evolution of multifunctional Ca(2+)/CaM-dependent protein kinase genes. *Gene* **2003,** *322*, 17-31.

34. Hudmon, A.; Schulman, H., Neuronal CA2+/calmodulin-dependent protein kinase II: the role of structure and autoregulation in cellular function. *Annu Rev Biochem* **2002,** *71*, 473-510.

35. Cook, S. G.; Bourke, A. M.; O'Leary, H.; Zaegel, V.; Lasda, E.; Mize-Berge, J.; Quillinan, N.; Tucker, C. L.; Coultrap, S. J.; Herson, P. S.; Bayer, K. U., Analysis of the CaMKIIalpha and beta splice-variant distribution among brain regions reveals isoform-specific differences in holoenzyme formation. *Sci Rep* **2018,** *8* (1), 5448.

36. Srinivasan, M.; Edman, C. F.; Schulman, H., Alternative splicing introduces a nuclear localization signal that targets multifunctional CaM kinase to the nucleus. *J Cell Biol* **1994,** *126* (4), 839-52.

37. O'Leary, H.; Lasda, E.; Bayer, K. U., CaMKIIbeta association with the actin cytoskeleton is regulated by alternative splicing. *Mol Biol Cell* **2006,** *17* (11), 4656-65.

38. Brocke, L.; Chiang, L. W.; Wagner, P. D.; Schulman, H., Functional implications of the subunit composition of neuronal CaM kinase II. *J Biol Chem* **1999,** *274* (32), 22713-22.

39. Vallano, M. L., Separation of isozymic forms of type II calcium/calmodulin-dependent protein kinase using cation-exchange chromatography. *J Neurosci Methods* **1989,** *30* (1), 1-9.

40. Feng, B.; Raghavachari, S.; Lisman, J., Quantitative estimates of the cytoplasmic, PSD, and NMDAR-bound pools of CaMKII in dendritic spines. *Brain Res* **2011,** *1419*, 46-52.

41. Lin, C. R.; Kapiloff, M. S.; Durgerian, S.; Tatemoto, K.; Russo, A. F.; Hanson, P.; Schulman, H.; Rosenfeld, M. G., Molecular cloning of a brain-specific calcium/calmodulin-dependent protein kinase. *Proc Natl Acad Sci U S A* **1987,** *84* (16), 5962-6.

42. Rosenberg, O. S.; Deindl, S.; Sung, R. J.; Nairn, A. C.; Kuriyan, J., Structure of the autoinhibited kinase domain of CaMKII and SAXS analysis of the holoenzyme. *Cell* **2005,** *123* (5), 849-60.

43. Payne, M. E.; Fong, Y. L.; Ono, T.; Colbran, R. J.; Kemp, B. E.; Soderling, T. R.; Means, A. R., Calcium/calmodulin-dependent protein kinase II. Characterization of distinct calmodulin binding and inhibitory domains. *J Biol Chem* **1988,** *263* (15), 7190-5.

44. Rellos, P.; Pike, A. C.; Niesen, F. H.; Salah, E.; Lee, W. H.; von Delft, F.; Knapp, S., Structure of the CaMKIIdelta/calmodulin complex reveals the molecular mechanism of CaMKII kinase activation. *PLoS Biol* **2010,** *8* (7), e1000426.

45. Chao, L. H.; Stratton, M. M.; Lee, I. H.; Rosenberg, O. S.; Levitz, J.; Mandell, D. J.; Kortemme, T.; Groves, J. T.; Schulman, H.; Kuriyan, J., A mechanism for tunable autoinhibition in the structure of a human Ca2+/calmodulin- dependent kinase II holoenzyme. *Cell* **2011,** *146* (5), 732-45.

46. Coultrap, S. J.; Buard, I.; Kulbe, J. R.; Dell'Acqua, M. L.; Bayer, K. U., CaMKII autonomy is substrate-dependent and further stimulated by Ca2+/calmodulin. *J Biol Chem* **2010,** *285* (23), 17930-7.

47. Miller, S. G.; Kennedy, M. B., Regulation of brain type II Ca2+/calmodulin-dependent protein kinase by autophosphorylation: a Ca2+-triggered molecular switch. *Cell* **1986,** *44* (6), 861-70.

48. Yang, E.; Schulman, H., Structural examination of autoregulation of multifunctional calcium/calmodulin-dependent protein kinase II. *J Biol Chem* **1999,** *274* (37), 26199-208.

49. Meyer, T.; Hanson, P. I.; Stryer, L.; Schulman, H., Calmodulin trapping by calcium-calmodulin-dependent protein kinase. *Science* **1992,** *256* (5060), 1199-202.

50. Colbran, R. J., Inactivation of Ca2+/calmodulin-dependent protein kinase II by basal autophosphorylation. *J Biol Chem* **1993,** *268* (10), 7163-70.

51. Hanson, P. I.; Schulman, H., Inhibitory autophosphorylation of multifunctional Ca2+/calmodulin-dependent protein kinase analyzed by site-directed mutagenesis. *J Biol Chem* **1992,** *267* (24), 17216-24.

52. Shields, S. M.; Vernon, P. J.; Kelly, P. T., Autophosphorylation of calmodulin-kinase II in synaptic junctions modulates endogenous kinase activity. *J Neurochem* **1984,** *43* (6), 1599-609.

53. Bhattacharyya, M.; Stratton, M. M.; Going, C. C.; McSpadden, E. D.; Huang, Y.; Susa, A. C.; Elleman, A.; Cao, Y. M.; Pappireddi, N.; Burkhardt, P.; Gee, C. L.; Barros, T.; Schulman, H.; Williams, E. R.; Kuriyan, J., Molecular mechanism of activation-triggered subunit exchange in Ca(2+)/calmodulin-dependent protein kinase II. *Elife* **2016,** *5*.

54. Jama, A. M.; Fenton, J.; Robertson, S. D.; Torok, K., Time-dependent autoinactivation of phospho-Thr286-alphaCa2+/calmodulin-dependent protein kinase II. *J Biol Chem* **2009,** *284* (41), 28146-55.

55. Bayer, K. U.; De Koninck, P.; Leonard, A. S.; Hell, J. W.; Schulman, H., Interaction with the NMDA receptor locks CaMKII in an active conformation. *Nature* **2001,** *411* (6839), 801-5.

56. Woodgett, J. R.; Davison, M. T.; Cohen, P., The calmodulin-dependent glycogen synthase kinase from rabbit skeletal muscle. Purification, subunit structure and substrate specificity. *Eur J Biochem* **1983,** *136* (3), 481-7.

57. Kolodziej, S. J.; Hudmon, A.; Waxham, M. N.; Stoops, J. K., Three-dimensional reconstructions of calcium/calmodulin-dependent (CaM) kinase IIalpha and truncated CaM kinase IIalpha reveal a unique organization for its structural core and functional domains. *J Biol Chem* **2000,** *275* (19), 14354-9.

58. Morris, E. P.; Torok, K., Oligomeric structure of alpha-calmodulin-dependent protein kinase II. *J Mol Biol* **2001,** *308* (1), 1-8.

59. Stratton, M.; Lee, I. H.; Bhattacharyya, M.; Christensen, S. M.; Chao, L. H.; Schulman, H.; Groves, J. T.; Kuriyan, J., Activation-triggered subunit exchange between CaMKII holoenzymes facilitates the spread of kinase activity. *Elife* **2013,** *3*, e01610.

60. Myers, J. B.; Zaegel, V.; Coultrap, S. J.; Miller, A. P.; Bayer, K. U.; Reichow, S. L., The CaMKII holoenzyme structure in activation-competent conformations. *Nat Commun* **2017,** *8*, 15742.

61. Hoelz, A.; Nairn, A. C.; Kuriyan, J., Crystal structure of a tetradecameric assembly of the association domain of Ca2+/calmodulin-dependent kinase II. *Mol Cell* **2003,** *11* (5), 1241-51.

62. Rosenberg, O. S.; Deindl, S.; Comolli, L. R.; Hoelz, A.; Downing, K. H.; Nairn, A. C.; Kuriyan, J., Oligomerization states of the association domain and the holoenyzme of Ca2+/CaM kinase II. *FEBS J* **2006,** *273* (4), 682-94.

63. Kanaseki, T.; Ikeuchi, Y.; Sugiura, H.; Yamauchi, T., Structural features of Ca2+/calmodulin-dependent protein kinase II revealed by electron microscopy. *J Cell Biol* **1991,** *115* (4), 1049-60.

64. Shen, K.; Teruel, M. N.; Subramanian, K.; Meyer, T., CaMKIIbeta functions as an F-actin targeting module that localizes CaMKIIalpha/beta heterooligomers to dendritic spines. *Neuron* **1998,** *21* (3), 593-606.

65. Gaertner, T. R.; Kolodziej, S. J.; Wang, D.; Kobayashi, R.; Koomen, J. M.; Stoops, J. K.; Waxham, M. N., Comparative analyses of the three-dimensional structures and enzymatic properties of alpha, beta, gamma and delta isoforms of Ca2+-calmodulin-dependent protein kinase II. *J Biol Chem* **2004,** *279* (13), 12484-94.

66. Bayer, K. U.; De Koninck, P.; Schulman, H., Alternative splicing modulates the frequency-dependent response of CaMKII to Ca(2+) oscillations. *EMBO J* **2002,** *21* (14), 3590-7.

67. Chao, L. H.; Pellicena, P.; Deindl, S.; Barclay, L. A.; Schulman, H.; Kuriyan, J., Intersubunit capture of regulatory segments is a component of cooperative CaMKII activation. *Nat Struct Mol Biol* **2010,** *17* (3), 264-72.

68. Bradshaw, J. M.; Kubota, Y.; Meyer, T.; Schulman, H., An ultrasensitive Ca2+/calmodulin-dependent protein kinase II-protein phosphatase 1 switch facilitates specificity in postsynaptic calcium signaling. *Proc Natl Acad Sci U S A* **2003,** *100* (18), 10512-7.

69. Lou, L. L.; Schulman, H., Distinct autophosphorylation sites sequentially produce autonomy and inhibition of the multifunctional Ca2+/calmodulin-dependent protein kinase. *J Neurosci* **1989,** *9* (6), 2020-32.

70. Hoffman, L.; Stein, R. A.; Colbran, R. J.; McHaourab, H. S., Conformational changes underlying calcium/calmodulin-dependent protein kinase II activation. *EMBO J* **2011,** *30* (7), 1251-62.

71. McMullan, G.; Faruqi, A. R.; Clare, D.; Henderson, R., Comparison of optimal performance at 300keV of three direct electron detectors for use in low dose electron microscopy. *Ultramicroscopy* **2014,** *147*, 156-63.

72. Russo, C. J.; Passmore, L. A., Electron microscopy: Ultrastable gold substrates for electron cryomicroscopy. *Science* **2014,** *346* (6215), 1377-80.

73. Russo, C. J.; Henderson, R., Charge accumulation in electron cryomicroscopy. *Ultramicroscopy* **2018,** *187*, 43-49.

74. Zheng, S. Q.; Palovcak, E.; Armache, J. P.; Verba, K. A.; Cheng, Y.; Agard, D. A., MotionCor2: anisotropic correction of beam-induced motion for improved cryo-electron microscopy. *Nat Methods* **2017,** *14* (4), 331-332.

75. Orlova, E. V.; Saibil, H. R., Structural analysis of macromolecular assemblies by electron microscopy. *Chem Rev* **2011,** *111* (12), 7710-48.

76. Danev, R.; Yanagisawa, H.; Kikkawa, M., Cryo-Electron Microscopy Methodology: Current Aspects and Future Directions. *Trends Biochem Sci* **2019,** *44* (10), 837-848.

77. Cheng, Y.; Grigorieff, N.; Penczek, P. A.; Walz, T., A primer to single-particle cryo-electron microscopy. *Cell* **2015,** *161* (3), 438-49.

78. Lander, G. C.; Stagg, S. M.; Voss, N. R.; Cheng, A.; Fellmann, D.; Pulokas, J.; Yoshioka, C.; Irving, C.; Mulder, A.; Lau, P. W.; Lyumkis, D.; Potter, C. S.; Carragher, B., Appion: an integrated, database-driven pipeline to facilitate EM image processing. *J Struct Biol* **2009,** *166* (1), 95-102.

79. Zivanov, J.; Nakane, T.; Forsberg, B. O.; Kimanius, D.; Hagen, W. J.; Lindahl, E.; Scheres, S. H., New tools for automated high-resolution cryo-EM structure determination in RELION-3. *Elife* **2018,** *7*.

80. Grant, T.; Rohou, A.; Grigorieff, N., cisTEM, user-friendly software for single-particle image processing. *Elife* **2018,** *7*.

81. Tang, G.; Peng, L.; Baldwin, P. R.; Mann, D. S.; Jiang, W.; Rees, I.; Ludtke, S. J., EMAN2: an extensible image processing suite for electron microscopy. *J Struct Biol* **2007,** *157* (1), 38-46.

82. Carroni, M.; Saibil, H. R., Cryo electron microscopy to determine the structure of macromolecular complexes. *Methods* **2016,** *95*, 78-85.

83. De Carlo, S.; Harris, J. R., Negative staining and cryo-negative staining of macromolecules and viruses for TEM. *Micron* **2011,** *42* (2), 117-31.

84. Ohi, M.; Li, Y.; Cheng, Y.; Walz, T., Negative Staining and Image Classification - Powerful Tools in Modern Electron Microscopy. *Biol Proced Online* **2004,** *6*, 23-34.

85. Passmore, L. A.; Russo, C. J., Specimen Preparation for High-Resolution Cryo-EM. *Methods Enzymol* **2016,** *579*, 51-86.

86. Thompson, R. F.; Walker, M.; Siebert, C. A.; Muench, S. P.; Ranson, N. A., An introduction to sample preparation and imaging by cryo-electron microscopy for structural biology. *Methods* **2016,** *100*, 3-15.

87. Taylor, K. A.; Glaeser, R. M., Retrospective on the early development of cryoelectron microscopy of macromolecules and a prospective on opportunities for the future. *J Struct Biol* **2008,** *163* (3), 214-23.

88. Yano, Y. F.; Arakawa, E.; Voegeli, W.; Kamezawa, C.; Matsushita, T., Initial Conformation of Adsorbed Proteins at an Air-Water Interface. *J Phys Chem B* **2018,** *122* (17), 4662-4666.

89. Noble, A. J.; Wei, H.; Dandey, V. P.; Zhang, Z.; Tan, Y. Z.; Potter, C. S.; Carragher, B., Reducing effects of particle adsorption to the air-water interface in cryo-EM. *Nat Methods* **2018,** *15* (10), 793-795.

90. Noble, A. J.; Dandey, V. P.; Wei, H.; Brasch, J.; Chase, J.; Acharya, P.; Tan, Y. Z.; Zhang, Z.; Kim, L. Y.; Scapin, G.; Rapp, M.; Eng, E. T.; Rice, W. J.; Cheng, A.; Negro, C. J.; Shapiro, L.; Kwong, P. D.; Jeruzalmi, D.; des Georges, A.; Potter, C. S.; Carragher, B., Routine single particle CryoEM sample and grid characterization by tomography. *Elife* **2018,** *7*.

91. Morris, E. P.; da Fonseca, P. C. A., High-resolution cryo-EM proteasome structures in drug development. *Acta Crystallogr D Struct Biol* **2017,** *73* (Pt 6), 522-533.

92. Benjamin, C. W., Kyle; Hyun, Seok-Hee; Krynski, Kyle; Yu, Guimei; Bajaj, Ruchika; Guo, Fei; Stauffacher, Cynthia; Jiang, Wen; Thompson, David, Non-fouling NTA-PEG-based TEM Grid Coatings for Selective Capture of Histidine-tagged Protein Targets from Cell Lysates. In *Langmuir*, 2015.

93. Benjamin, C. J.; Wright, K. J.; Bolton, S. C.; Hyun, S. H.; Krynski, K.; Grover, M.; Yu, G.; Guo, F.; Kinzer-Ursem, T. L.; Jiang, W.; Thompson, D. H., Selective Capture of Histidine-tagged Proteins from Cell Lysates Using TEM grids Modified with NTA-Graphene Oxide. *Sci Rep* **2016,** *6*, 32500.

94. Kelly, D. F.; Dukovski, D.; Walz, T., Monolayer purification: a rapid method for isolating protein complexes for single-particle electron microscopy. *Proc Natl Acad Sci U S A* **2008,** *105* (12), 4703-8.

95. Fraseur, J. G.; Kinzer-Ursem, T. L., Next generation calmodulin affinity purification: Clickable calmodulin facilitates improved protein purification. *PLoS One* **2018,** *13* (6), e0197120.

96. Hudmon, A.; Aronowski, J.; Kolb, S. J.; Waxham, M. N., Inactivation and self-association of Ca2+/calmodulin-dependent protein kinase II during autophosphorylation. *J Biol Chem* **1996,** *271* (15), 8800-8.

97. Bartesaghi, A.; Merk, A.; Banerjee, S.; Matthies, D.; Wu, X.; Milne, J. L.; Subramaniam, S., 2.2 A resolution cryo-EM structure of beta-galactosidase in complex with a cell-permeant inhibitor. *Science* **2015,** *348* (6239), 1147-51.

98. Banerjee, S.; Bartesaghi, A.; Merk, A.; Rao, P.; Bulfer, S. L.; Yan, Y.; Green, N.; Mroczkowski, B.; Neitz, R. J.; Wipf, P.; Falconieri, V.; Deshaies, R. J.; Milne, J. L.; Huryn, D.; Arkin, M.; Subramaniam, S., 2.3 A resolution cryo-EM structure of human p97 and mechanism of allosteric inhibition. *Science* **2016,** *351* (6275), 871-5.

99. Russo, C. J.; Passmore, L. A., Controlling protein adsorption on graphene for cryo-EM using low-energy hydrogen plasmas. *Nat Methods* **2014,** *11* (6), 649-52.

100. Meyerson, J. R.; Rao, P.; Kumar, J.; Chittori, S.; Banerjee, S.; Pierson, J.; Mayer, M. L.; Subramaniam, S., Self-assembled monolayers improve protein distribution on holey carbon cryo-EM supports. *Sci Rep* **2014,** *4*, 7084.

101. Russo, C. J.; Passmore, L. A., Ultrastable gold substrates: Properties of a support for high-resolution electron cryomicroscopy of biological specimens. *J Struct Biol* **2016,** *193* (1), 33-44.

102. Kelly, D. F.; Abeyrathne, P. D.; Dukovski, D.; Walz, T., The Affinity Grid: A pre-fabricated EM grid for monolayer purification. *Journal of molecular biology* **2008,** *382* (2), 423-433.

103. Kelly, D. F.; Dukovski, D.; Walz, T., Strategy for the use of affinity grids to prepare non-His-tagged macromolecular complexes for single-particle electron microscopy. *J Mol Biol* **2010,** *400* (4), 675-81.

104. Kutsay, O.; Loginova, O.; Gontar, A.; Perevertailo, V.; Zanevskyy, O.; Katrusha, A.; Ivakhnenko, S.; Gorokhov, V.; Starik, S.; Tkach, V.; Novikov, N., Surface properties of amorphous carbon films. *Diamond and Related Materials* **2008,** *17* (7–10), 1689-1691.

105. Barklis, E.; McDermott, J.; Wilkens, S.; Schabtach, E.; Schmid, M. F.; Fuller, S.; Karanjia, S.; Love, Z.; Jones, R.; Rui, Y.; Zhao, X.; Thompson, D., Structural analysis of membrane-bound retrovirus capsid proteins. *The EMBO Journal* **1997,** *16* (6), 1199-1213.

106. Kubalek, E. W.; Le Grice, S. F.; Brown, P. O., Two-dimensional crystallization of histidine-tagged, HIV-1 reverse transcriptase promoted by a novel nickel-chelating lipid. *J Struct Biol* **1994,** *113* (2), 117-23.

107. Schmitt, L.; Dietrich, C.; Tampe, R., Synthesis and Characterization of Chelator-Lipids for Reversible Immobilization of Engineered Proteins at Self-Assembled Lipid Interfaces. *Journal of the American Chemical Society* **1994,** *116* (19), 8485-8491.

108. Thompson, D. H.; Zhou, M.; Grey, J.; Kim, H.-k., Design, Synthesis, and Performance of NTA-modified Lipids as Templates for Histidine-tagged Protein Crystallization. *Chemistry Letters* **2007,** *36* (8), 956-975.

109. Marcano, D. C.; Kosynkin, D. V.; Berlin, J. M.; Sinitskii, A.; Sun, Z.; Slesarev, A.; Alemany, L. B.; Lu, W.; Tour, J. M., Improved synthesis of graphene oxide. *ACS Nano* **2010,** *4* (8), 4806-14.

110. Cote, L. J.; Kim, J.; Zhang, Z.; Sun, C.; Huang, J. X., Tunable assembly of graphene oxide surfactant sheets: wrinkles, overlaps and impacts on thin film properties. *Soft Matter* **2010,** *6* (24), 6096-6101.

111. Song, J. P.; Qiao, J.; Shuang, S. M.; Guo, Y. J.; Dong, C., Synthesis of neutral red covalently functionalized graphene nanocomposite and the electrocatalytic properties toward uric acid. *J Mater Chem* **2012,** *22* (2), 602-608.

112. Suloway, C.; Pulokas, J.; Fellmann, D.; Cheng, A.; Guerra, F.; Quispe, J.; Stagg, S.; Potter, C. S.; Carragher, B., Automated molecular microscopy: the new Leginon system. *J Struct Biol* **2005,** *151* (1), 41-60.

113. Ludtke, S. J.; Baker, M. L.; Chen, D. H.; Song, J. L.; Chuang, D. T.; Chiu, W., De novo backbone trace of GroEL from single particle electron cryomicroscopy. *Structure* **2008,** *16* (3), 441-8.

114. Pettersen, E. F.; Goddard, T. D.; Huang, C. C.; Couch, G. S.; Greenblatt, D. M.; Meng, E. C.; Ferrin, T. E., UCSF Chimera--a visualization system for exploratory research and analysis. *J Comput Chem* **2004,** *25* (13), 1605-12.

115. Zhang, J.; Yu, J. G.; Jaroniec, M.; Gong, J. R., Noble Metal-Free Reduced Graphene Oxide-ZnxCd1-xS Nanocomposite with Enhanced Solar Photocatalytic H-2-Production Performance. *Nano Lett* **2012,** *12* (9), 4584-4589.

116. Wang, G. X.; Wang, B.; Park, J.; Yang, J.; Shen, X. P.; Yao, J., Synthesis of enhanced hydrophilic and hydrophobic graphene oxide nanosheets by a solvothermal method. *Carbon* **2009,** *47* (1), 68-72.

117. Paredes, J. I.; Villar-Rodil, S.; Martínez-Alonso, A.; Tascón, J. M. D., Graphene Oxide Dispersions in Organic Solvents. *Langmuir* **2008,** *24* (19), 10560-10564.

118. Gengler, R. Y.; Veligura, A.; Enotiadis, A.; Diamanti, E. K.; Gournis, D.; Jozsa, C.; van Wees, B. J.; Rudolf, P., Large-yield preparation of high-electronic-quality graphene by a Langmuir-Schaefer approach. *Small* **2010,** *6* (1), 35-9.

119. Kim, J.; Cote, L. J.; Kim, F.; Yuan, W.; Shull, K. R.; Huang, J., Graphene Oxide Sheets at Interfaces. *Journal of the American Chemical Society* **2010,** *132* (23), 8180-8186.

120. Cote, L. J.; Kim, J.; Tung, V. C.; Luo, J. Y.; Kim, F.; Huang, J. X., Graphene oxide as surfactant sheets. *Pure Appl Chem* **2011,** *83* (1), 95-110.

121. Cote, L. J.; Kim, F.; Huang, J., Langmuir-Blodgett assembly of graphite oxide single layers. *J Am Chem Soc* **2009,** *131* (3), 1043-9.

122. Kim, J.; Cote, L. J.; Huang, J., Two dimensional soft material: new faces of graphene oxide. *Acc Chem Res* **2012,** *45* (8), 1356-64.

123. Zheng, Q. B.; Shi, L. F.; Ma, P. C.; Xue, Q. Z.; Li, J.; Tang, Z. H.; Yang, J. H., Structure control of ultra-large graphene oxide sheets by the Langmuir-Blodgett method. *Rsc Adv* **2013,** *3* (14), 4680-4691.

124. Ni, Z. H.; Wang, H. M.; Kasim, J.; Fan, H. M.; Yu, T.; Wu, Y. H.; Feng, Y. P.; Shen, Z. X., Graphene thickness determination using reflection and contrast spectroscopy. *Nano Lett* **2007,** *7* (9), 2758-63.

125. Wilson, N. R.; Pandey, P. A.; Beanland, R.; Young, R. J.; Kinloch, I. A.; Gong, L.; Liu, Z.; Suenaga, K.; Rourke, J. P.; York, S. J.; Sloan, J., Graphene Oxide: Structural Analysis and Application as a Highly Transparent Support for Electron Microscopy. *Acs Nano* **2009,** *3* (9), 2547-2556.

126. Pan, S. Y.; Aksay, I. A., Factors Controlling the Size of Graphene Oxide Sheets Produced via the Graphite Oxide Route. *Acs Nano* **2011,** *5* (5), 4073-4083.

127. Ema, T.; Miyazaki, Y.; Koyama, S.; Yano, Y.; Sakai, T., A bifunctional catalyst for carbon dioxide fixation: cooperative double activation of epoxides for the synthesis of cyclic carbonates. *Chem Commun (Camb)* **2012,** *48* (37), 4489-91.

128. Ludtke, S. J.; Chen, D. H.; Song, J. L.; Chuang, D. T.; Chiu, W., Seeing GroEL at 6 A resolution by single particle electron cryomicroscopy. *Structure* **2004,** *12* (7), 1129-36.

129. Ludtke, S. J.; Jakana, J.; Song, J. L.; Chuang, D. T.; Chiu, W., A 11.5 A single particle reconstruction of GroEL using EMAN. *J Mol Biol* **2001,** *314* (2), 253-62.

130. Lisman, J.; Schulman, H.; Cline, H., The molecular basis of CaMKII function in synaptic and behavioural memory. *Nat Rev Neurosci* **2002,** *3* (3), 175-90.

131. Bennett, M. K.; Erondu, N. E.; Kennedy, M. B., Purification and characterization of a calmodulin-dependent protein kinase that is highly concentrated in brain. *J Biol Chem* **1983,** *258* (20), 12735-44.

132. Hudmon, A.; Kim, S. A.; Kolb, S. J.; Stoops, J. K.; Waxham, M. N., Light scattering and transmission electron microscopy studies reveal a mechanism for calcium/calmodulin-dependent protein kinase II self-association. *J Neurochem* **2001,** *76* (5), 1364-75.

133. Brickey, D. A.; Colbran, R. J.; Fong, Y. L.; Soderling, T. R., Expression and characterization of the alpha-subunit of Ca2+/calmodulin-dependent protein kinase II using the baculovirus expression system. *Biochem Biophys Res Commun* **1990,** *173* (2), 578-84.

134. Putkey, J. A.; Waxham, M. N., A peptide model for calmodulin trapping by calcium/calmodulin-dependent protein kinase II. *J Biol Chem* **1996,** *271* (47), 29619-23.

135. Kolb, S. J.; Hudmon, A.; Ginsberg, T. R.; Waxham, M. N., Identification of domains essential for the assembly of calcium/calmodulin-dependent protein kinase II holoenzymes. *J Biol Chem* **1998,** *273* (47), 31555-64.

136. Singla, S. I.; Hudmon, A.; Goldberg, J. M.; Smith, J. L.; Schulman, H., Molecular characterization of calmodulin trapping by calcium/calmodulin-dependent protein kinase II. *J Biol Chem* **2001,** *276* (31), 29353-60.

137. Torok, K.; Tzortzopoulos, A.; Grabarek, Z.; Best, S. L.; Thorogate, R., Dual effect of ATP in the activation mechanism of brain Ca(2+)/calmodulin-dependent protein kinase II by Ca(2+)/calmodulin. *Biochemistry* **2001,** *40* (49), 14878-90.

138. Leibly, D. J.; Nguyen, T. N.; Kao, L. T.; Hewitt, S. N.; Barrett, L. K.; Van Voorhis, W. C., Stabilizing additives added during cell lysis aid in the solubilization of recombinant proteins. *PLoS One* **2012,** *7* (12), e52482.

139. Maranga, L.; Coroadinha, A. S.; Carrondo, M. J., Insect cell culture medium supplementation with fetal bovine serum and bovine serum albumin: effects on baculovirus adsorption and infection kinetics. *Biotechnol Prog* **2002,** *18* (4), 855-61.

140. Coultrap, S. J.; Bayer, K. U., Ca2+/Calmodulin-Dependent Protein Kinase II (CaMKII). In *Protein Kinase Technologies*, Mukai, H., Ed. Humana Press: Totowa, NJ, 2012; pp 49-72.

141. Shrestha, A.; Hamilton, G.; O'Neill, E.; Knapp, S.; Elkins, J. M., Analysis of conditions affecting auto-phosphorylation of human kinases during expression in bacteria. *Protein Expr Purif* **2012,** *81* (1), 136-143.

142. Stratton, M. M.; Chao, L. H.; Schulman, H.; Kuriyan, J., Structural studies on the regulation of Ca2+/calmodulin dependent protein kinase II. *Curr Opin Struct Biol* **2013,** *23* (2), 292-301.

143. Wilde, M.; Klausberger, M.; Palmberger, D.; Ernst, W.; Grabherr, R., Tnao38, high five and Sf9--evaluation of host-virus interactions in three different insect cell lines: baculovirus production and recombinant protein expression. *Biotechnol Lett* **2014,** *36* (4), 743-9.

144. Unger, T.; Peleg, Y., Recombinant protein expression in the baculovirus-infected insect cell system. *Methods Mol Biol* **2012,** *800*, 187-99.

145. Wilkins, M. R.; Gasteiger, E.; Bairoch, A.; Sanchez, J. C.; Williams, K. L.; Appel, R. D.; Hochstrasser, D. F., Protein identification and analysis tools in the ExPASy server. *Methods Mol Biol* **1999,** *112*, 531-52.

146. Hutchings, J.; Stancheva, V.; Miller, E. A.; Zanetti, G., Subtomogram averaging of COPII assemblies reveals how coat organization dictates membrane shape. *Nat Commun* **2018,** *9* (1), 4154.

147. Schur, F. K.; Obr, M.; Hagen, W. J.; Wan, W.; Jakobi, A. J.; Kirkpatrick, J. M.; Sachse, C.; Krausslich, H. G.; Briggs, J. A., An atomic model of HIV-1 capsid-SP1 reveals structures regulating assembly and maturation. *Science* **2016,** *353* (6298), 506-8.

148. Chreifi, G.; Chen, S.; Metskas, L. A.; Kaplan, M.; Jensen, G. J., Rapid tilt-series acquisition for electron cryotomography. *J Struct Biol* **2019,** *205* (2), 163-169.

149. Noble, A. J.; Stagg, S. M., Automated batch fiducial-less tilt-series alignment in Appion using Protomo. *J Struct Biol* **2015,** *192* (2), 270-8.

150. Zhang, P., Advances in cryo-electron tomography and subtomogram averaging and classification. *Curr Opin Struct Biol* **2019,** *58*, 249-258.

151. Schur, F. K., Toward high-resolution in situ structural biology with cryo-electron tomography and subtomogram averaging. *Curr Opin Struct Biol* **2019,** *58*, 1-9.

152. Wan, W.; Briggs, J. A., Cryo-Electron Tomography and Subtomogram Averaging. *Methods Enzymol* **2016,** *579*, 329-67.

153. Briggs, J. A., Structural biology in situ--the potential of subtomogram averaging. *Curr Opin Struct Biol* **2013,** *23* (2), 261-7.

154. Hoffman, L.; Farley, M. M.; Waxham, M. N., Calcium-calmodulin-dependent protein kinase II isoforms differentially impact the dynamics and structure of the actin cytoskeleton. *Biochemistry* **2013,** *52* (7), 1198-207.

155. Wang, Q.; Chen, M.; Schafer, N. P.; Bueno, C.; Song, S. S.; Hudmon, A.; Wolynes, P. G.; Waxham, M. N.; Cheung, M. S., Assemblies of calcium/calmodulin-dependent kinase II with actin and their dynamic regulation by calmodulin in dendritic spines. *Proc Natl Acad Sci U S A* **2019,** *116* (38), 18937-18942.

156. Mastronarde, D. N., Automated electron microscope tomography using robust prediction of specimen movements. *J Struct Biol* **2005,** *152* (1), 36-51.

157. Hagen, W. J. H.; Wan, W.; Briggs, J. A. G., Implementation of a cryo-electron tomography tilt-scheme optimized for high resolution subtomogram averaging. *J Struct Biol* **2017,** *197* (2), 191-198.

158. Rohou, A.; Grigorieff, N., CTFFIND4: Fast and accurate defocus estimation from electron micrographs. *J Struct Biol* **2015,** *192* (2), 216-21.

159. Kremer, J. R.; Mastronarde, D. N.; McIntosh, J. R., Computer visualization of three-dimensional image data using IMOD. *J Struct Biol* **1996,** *116* (1), 71-6.

160. Nicastro, D.; Schwartz, C.; Pierson, J.; Gaudette, R.; Porter, M. E.; McIntosh, J. R., The molecular architecture of axonemes revealed by cryoelectron tomography. *Science* **2006,** *313* (5789), 944-8.